LIGHT SHEET MICROSCOPY INCORPORATING ADAPTIVE OPTICS

by

KEELAN M. LAWRENCE

(Under Direction of Peter A. Kner)

ABSTRACT

When imaging deep into biological samples in Light Sheet Microscopy, refractive index variations within the sample, as well as differences between the sample, immersion medium, and sample holder distort the optical wavefront causing a loss of resolution and a decrease of the signal to noise ratio of the image. By implementing Adaptive Optics in a light sheet system, optical aberrations can be corrected and resolution can be increased despite the wavefront distortions cause by the organism. Adaptive Optics systems operate by sensing the wavefront of the incident light and then correcting the distortions in the wavefront with a modulation element. In this paper, we cover the design and implementation of an Adaptive Optics system composed of a deformable mirror and Shack-Hartmann Wavefront Sensor for the measurement and correction of wavefront aberrations caused by zebrafish (*D. rerio*) larvae during live imaging with Light Sheet Microscopy.

Index Words: Light Sheet Microscopy, Adaptive Optics, and *D. rerio*

LIGHT SHEET MICROSCOPY INCORPORATING ADAPTIVE OPTICS

by

KEELAN M. LAWRENCE

BS, University of Georgia, 2014

A Thesis Submitted to the Graduate Faculty of The University of Georgia in Partial Fulfilment of the Requirements of the Degree

MASTER OF SCIENCE

ATHENS, GEORGIA

2018

LIGHT SHEET MICROSCOPY INCORPORATING ADAPTIVE OPTICS

by

KEELAN M. LAWRENCE

Major Professor: Peter Kner

Committee: Mark Haidekker

James Lauderdale

Electronic Version Approved:

Suzanne Barbour

Dean of the Graduate School

The University of Georgia

May 2018

TABLE OF CONTENTS

CHAPTER 1:

INTRODUCTION

Purpose of study

Light Sheet Microscopy is a key imaging modality for observing live biological samples. Compared to a conventional epi-fluorescence microscope, light sheet microscopes combat photo-damage by illuminating only a thin slice of the sample at a time. This limiting of light exposure also provides natural optical sectioning capability and reduces the amount of background light outside of the plane of interest resulting in high contrast images similar to confocal microscopy. However, confocal microscopy is a point-scanning technique. Light sheet microscopy image acquisition rates are hundreds of times faster than confocal microscopy acquisition rates. Figure 1.1 illustrates the principle behind the light sheet microscope. A thin sheet of light illuminates the sample orthogonal to the detection axis. The plane of interest within the sample is placed in the focal plane of the detection objective. The specimens used for this study are 5 to 7 day old zebrafish larvae. The larvae are around 3~4 mm in total body length and the zebrafish brain has a volume of around 350 μm^3.

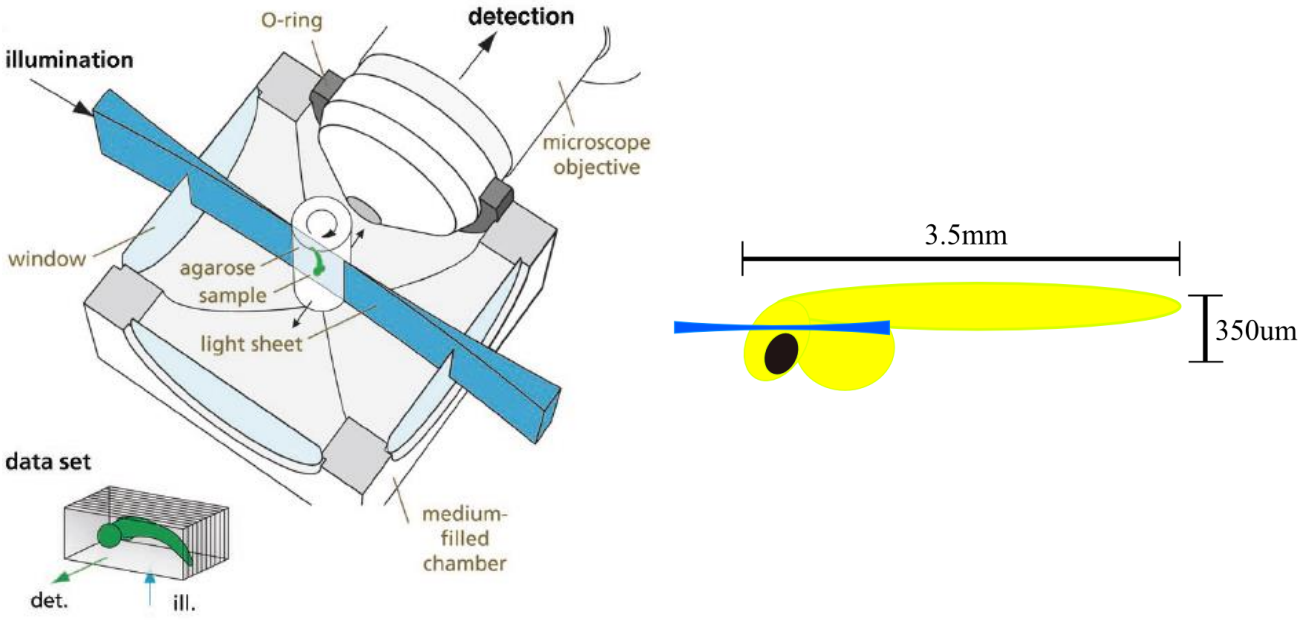

Figure 1.1: (a) Diagram illustrating the principle behind Light Sheet Microscopy [1]. (b) Illustration showing the scale between the zebrafish body length (3.5mm), head size (350um) and sheet width (7um).

Optical aberrations caused by the biological sample when imaging deep in tissue limit the effectiveness of a conventional light sheet microscope. When imaging biological samples, light waves traveling from the area of interest become aberrated due to the variations of the refractive index within the sample. As light enters a medium with an index of refraction different from the previous, the light will bend due to Snell's law and experience a change in speed. This leads to variations in the local tip and tilt of the wavefront as well as differences in the optical path length traveled by different rays of the light wave. Figure 1.2 illustrates the wavefront distortions due to changes in the refractive index of the propagation medium with in a confocal system.

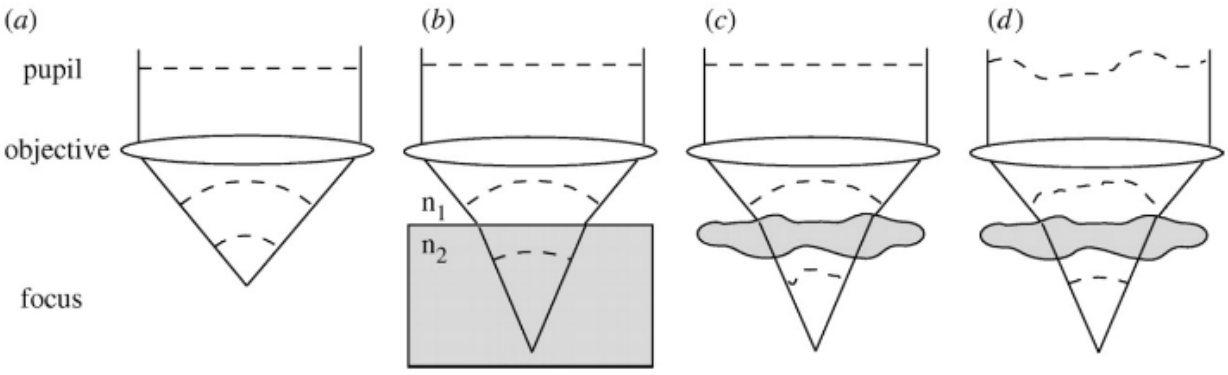

Figure 1.2: illustrating how the refractive index effects wavefront shape in four different scenarios. Each situation has a propagating wavefront from a pupil that is focused by a microscope objective to the focal plane. (a) illustrates the ideal microscope system. A plane wavefront is converted to a spherical wavefront which converges at the focus. (b) shows the effect of a refractive index mismatch which induces spherical aberration. (c) shows the effect of a complex shaped object which a variant index of refraction, similar to a biological sample. A plane wavefront becomes distorted and aberrated after passing through the object. (d) shows an example of a modulated wavefront in the pupil plane that forms a focus similar to that of (b) [11].

These optical aberrations change the size and shape of the microscopes point-spread-function (PSF). The PSF convolved with the object of interest forms the resulting image. An ideal diffraction limited microscope has a PSF the shape of an Airy disk. Wavefront aberrations distort the PSF into a larger less dense intensity distribution causing lower resolution in the image when convolved with the object. The addition of Adaptive Optics (AO) into a light sheet system can correct optical aberrations to obtain high-resolution images of biological processes within deep tissue.

AO systems were first used in ground-based telescopes in the 1970s to correct for aberrations caused by atmospheric turbulence [10]. The optical setup for an astronomical AO system is shown in figure 1.3. The system functions by sensing the wavefront of the collected light, then modulating the phase of the wavefront with a correction element. The wavefront is usually measured with a Shack-Hartmann Wavefront Sensor (SHWFS) and corrected with a deformable mirror (DM).

The success of AO for correcting aberrations in the field of astronomy has encouraged research in applications for microscopy. AO systems have been successfully designed and implemented in wide-field [3, 4], confocal [5], multi-photon [6, 7], and light sheet microscopy [8]. Some of these AO systems use modal methods to determine the optimum mirror shape instead of a wavefront sensor. Modal methods determine the optimal wavefront correction based on various metrics used to deduce image quality. The systems using a SHWFS, in general, do not use the biological scene to measure the wavefront but image structures that resemble point sources or image microbeads injected into the sample.

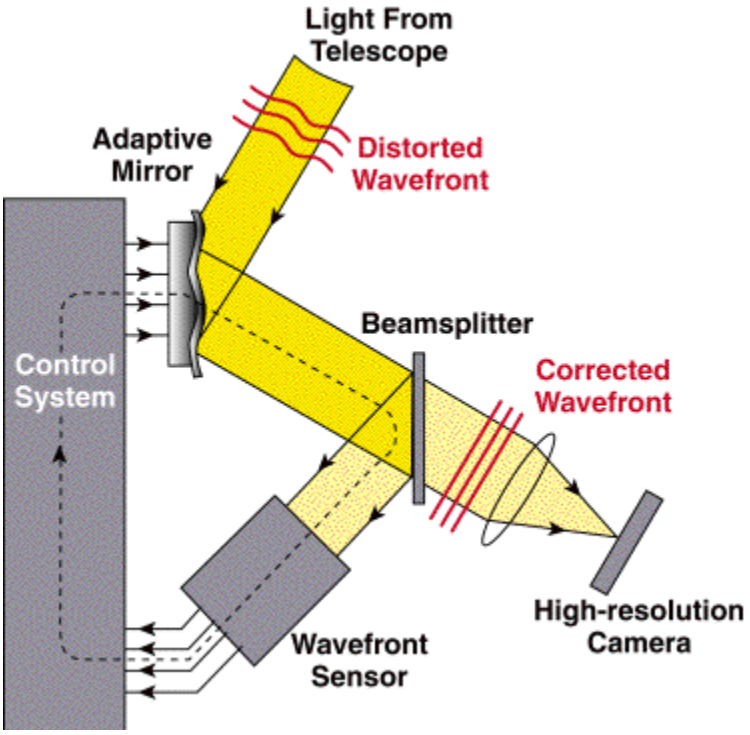

Figure 1.3: Diagram illustrating the principle behind Adaptive Optics [2].

Typically, wavefront sensors require a reference image or “guide star” that closely resembles a point source emitting light. Guide stars are naturally observed in astronomy when imaging an image such as a distant star. However, a typical SHWFS will be unable to sense the

wavefront when looking at images such as the sun. The sun has distant features and relying on typical SHWFS center of mass calculation will be unreliable. Applying Cross Correlation instead of conventional centroid methods to measure local gradients will allow the use of a SHWFS to measure the wavefront for general scenes instead of just objects resembling point sources [9].

In this manuscript, we propose using a SHWFS to measure the wavefront when looking at general scenes within samples. Applying Cross Correlation in replacement of centroid algorithms, we can determine local wavefront gradients without the use of a guide-star.

This study discusses the design and implementation of an AO system within a light sheet microscope, applying a cross-correlation approach for determining local image shifts using a SHWFS. The measurement and correction of aberrations caused when imaging *D. rerio* (zebrafish) will be explored. We will apply the AO-LSM to imaging zebrafish neural activity with the light sheet microscope.

Significance

Zebrafish are a model organism commonly studied to further understanding of biological processes. Zebrafish are transparent while in their embryonic state making them ideal for imaging with light sheet microscopy. These model organisms can be easily bred and maintained, and provide insight into many processes important for all vertebrates. The fish observed for the study have been trans-genetically modified to have seizures and to encode a green fluorescent calcium sensor. Imaging the calcium waves within zebrafish could increase the understanding of seizures in both zebrafish and humans alike.

The increase of resolution capabilities by adding Scene Based Wavefront Sensing and AO to Light-Sheet Microscopy will allow biological processes within zebrafish to be viewed with enhanced detail. Obtaining images of live neural activity will lead to an increased

understanding of seizure dynamics. Demonstration of successful wavefront measurement and correction applying a SHWFS for the use of observing general scenes with a microscope will lead to more imaging modalities applying a SHWFS in cases were guide stars are not applicable or available.

Organization of Thesis

The thesis begins with background information on the history of Light Sheet Microscopy, sources of aberration in microscopy, Adaptive Optics, and *D. rerio in* Chapter 2. Chapter 3 provides background on the Shack-Hartmann Wavefront Sensor component of the Adaptive Optics system and how to reconstruct the wavefront from the sensor's signal. Chapter 4 presents all experimental setups for this study. Details on the systems, their parts, and construction are discussed. Chapter 5 shows the results of the study, conclusions, and future studies. After the chapters is an appendix discussing software used to control instruments as well as drawings for all machined parts.

References

1.Huisken J, Swoger J, Del Bene F, Wittbrodt J, Stelzer EH. 2004. Optical sectioning deep inside live embryos by selective plane illumination microscopy

2.Max, C., University of California at Santa Cruz, Astronomy 289C.

3.Kner, P., Sedat, J. W., Agard, D. A., Kam, Z. 2009. High-resolution wide-field microscopy with adaptive optics for spherical aberration correction and motionless focusing. Journal of Microscopy.

4.Azucena, O. et al. 2010. Wavefront aberrations measurements and corrections through thick tissue using fluorescent microsphere reference beacons. Optics Express. Vol. 18. p. 17522-17532.

5.Booth, M. J., Neil, M. A. A., Juskaitis, R., and T. Wilson. 2002. Adaptive aberration correction in a confocal microscope. *PNAS.* Vol. 99, p.5788-5792.

6.Sherman, L., Ye, J. Y. , Albert, O., Norris, T.B. 2002. Adaptive correction of depth-induced aberrations in multiphoton scanning microscopy using a deformable mirror. *J. Microscopy.* Vol. 206, p.65-71

7.Neil, M. A. et al. 2000. Adaptive aberration correction in a two-photon microscope. *Journal of Microscopy.* Vol. 200, p.105-108.

8. Cyril Bourgenot, C. D. S., Jonathan M. Taylor, John M. Girkin, and Dordon D. Love (2012). "3D adaptive optics in a light sheet microscope." Optics Express **20**(12): 10.

9. Poyneer, L. A. (2003). "Scene-based Shack-Hartann wave-front sensing: analysis and simulation." Applied Optics 42(29): 9.

10. Hardy, J. W. 1998. Adaptive Optics for Astronomical Telescopes. New York, N. Y.: Oxford University Press

11. M. J. Booth, "Adaptive optics in microscopy," *Philos Transact Math Phys Eng Sci*, vol 365, pp. 2829-43, Dec 15 2007

CHAPTER 2:

BACKGROUND

The purpose of this chapter is to provide necessary background on light sheet microscopy and Shack-Hartmann wavefront sensors. We discuss fluorescence and how it is used in microscopy and the development of light sheet microscopy. Next is a discussion of the physics responsible for a trade-off between beam width and maximum field of view while imaging with a LSM. We then discuss mathematical properties of optical wavefronts and how aberrated wavefronts form distorted lower quality images. This topic leads into the technologies incorporated for correcting the optical wavefront to enhance the features of the systems captured scene. Finally, we discuss the biological organism imaged in this study, *D Rerio*.

Fluorescence Microscopy

Fluorescence is the re-emission of a photon from a molecule that has absorbed a photon at a higher energy [25]. Fluorescent molecules have been developed that have specific excitation and emission wavelengths and are chemically engineered to be attached to antibodies such that optical imaging can be applied to capture the fluorescent light to form an image. The fluorophore attaches to the antibody outlining the structure. The labeled antibodies have a high affinity for proteins in which they conjugate. Exciting the fluorophores with a specific wavelength will excite the molecule and the image is formed by detecting this light. Fluorescent tagging can also be accomplished genetically where the genetic sequence for a particular fluorescent protein is fused to the sequence for a protein of interest. Fluorescent tagging was an important discovery in microscopy, allowing specific proteins of interest to be labeled [26, 27]. In fluorescence

microscopy, excitation light excites the fluorophores in the sample. The fluorophores absorb the light and enter an excited state. The flourophores fluoresce at a wavelength that is longer than the wavelength of the excitation light. This spectrum shift is due to energy loss from vibrational modes of the molecule. This energy loss is called the Stokes Shift and can be seen in Figure 2.1 that illustrates the intensity spectrum of the excitation and emission profiles (b). Separating the fluorescence signal from the excitation light allows the detector to only capture the light emitted by the fluorophores. Figure 2.1 (a) illustrates the principle behind a fluorescence microscope. A single microscope objective is used to both illuminate the sample and capture light emitted by the sample. A dichroic reflects the excitation light and transmits the sample's emitted light. The tube lens forms the final image on the CCD detector.

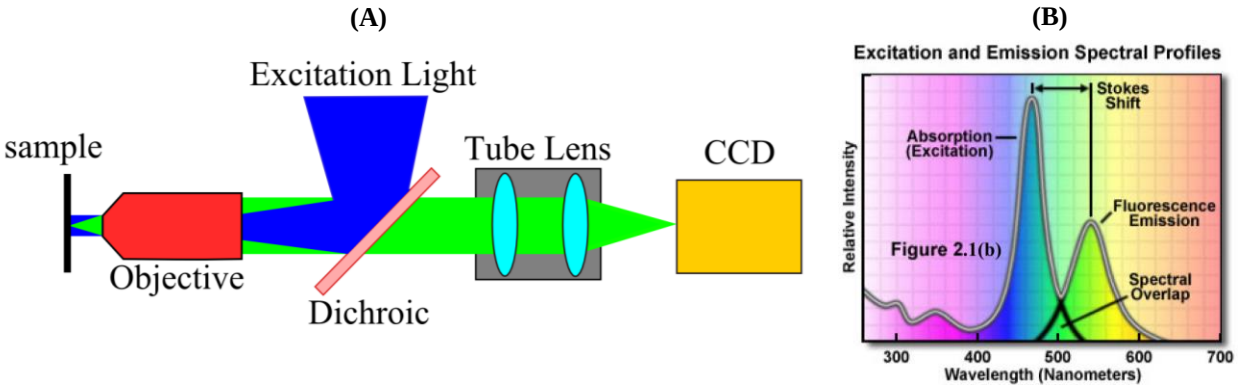

Figure 2.1 (a) Principle of a fluorescence microscope. (b) shows the emission spectrum of the absorption and emission light from fluorescence [26].

Light Sheet Microscopy

Light Sheet Microscopy is a fluorescence microscopy technique designed to reduce background light, improve optical sectioning, and decrease photo bleaching compared to standard fluorescence microscopes while maintaining fast image acquisition. The method works by decoupling the excitation and emission optical paths. A common method to accomplish the decoupling is by placing illumination and detection objectives in a perpendicular arrangement

such that their focal planes intersect. Figure 2.2 shows the two objective configuration for a light sheet microscope. This configuration allows the sample to be illuminated from the side by a sheet of light only a few microns thick. Siedentopf and Zsigmondy first proposed light sheet microscopy in 1903 [12] and applied the microscope to image nanometer sized gold particles. Voie, Burns, and Spelman applied a cylindrical lens to create a static light sheet to image the inner ear cochlea of a guinea pig [13]. Later, Huisken et al performed a renaissance of the illumination technique in 2004 for live developmental biology applications. The LSM successfully imaged *D. melanogaster* in vivo to capture events of embryogenesis [14]. Keller established a digitally scanned light-sheet microscope to analyze the zebrafish gastrulation [15]. This method creates a light sheet by scanning a laser beam while exposing the pixels of the imaging element sequentially with the position of the beam. Techniques using non-diffracting light beams have been recently developed to maintain narrow light sheets over a larger field of view. Betzig imaged filopodia in a HeLa cell using a lattice light sheet microscope [16]. This technique applies Bessel beams over standard Gaussian beams to increase the range over which the light sheet maintains its width. Dholakia clearly resolved fine details of individual sarcomeres in a muscle block of a zebrafish larva using Airy beam illumination [17].

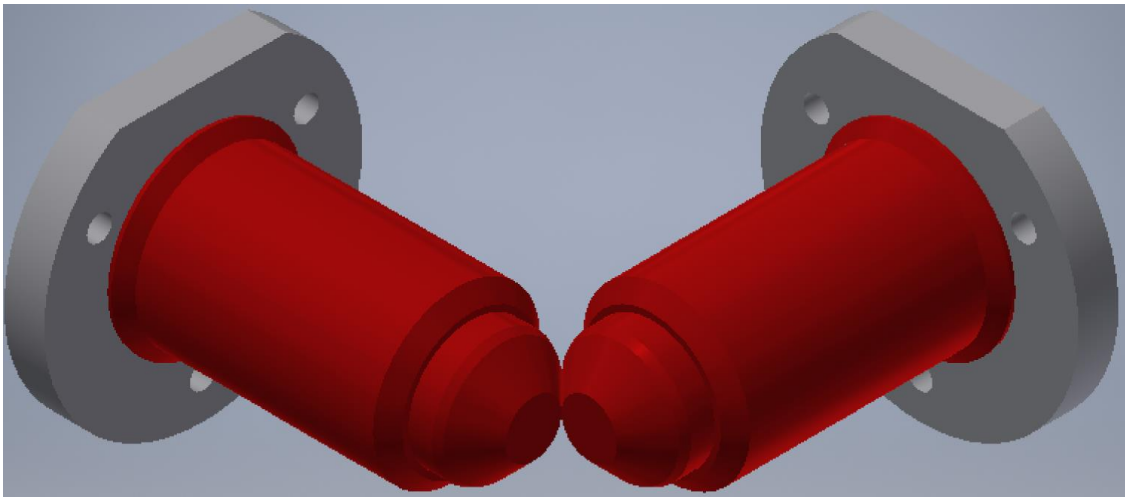

Figure 2.2: Two objective configuration for a light sheet microscope. One objective is used for sample illumination and the other to capture the image.

Rayleigh Range and Beam Waist

In light sheet microscopy, there is a tradeoff between sheet width and the range over which the sheet maintains its beam waist. This translates to a tradeoff between axial resolution and maximum field of view. This tradeoff is due to the law of diffraction. Light spreads out as it propagates through space. This is because the tails of the Gaussian beam where the amount of intensity has dropped to off past $1/e^2$ of its on-axis value increases while propagating. The diameter of the beam increases linearly as the off axis distance increases. The distribution intensity remains Gaussian at every point on the wave, only the radius of the Gaussian beam and the radius of curvature of the wavefront change. The diffraction rate increases as the beam waist decreases. The Rayleigh range, illustrated in Figure 2.3 (b), is the distance over which the beam radius increases by $\sqrt{2}$ and determines the range over which a Gaussian light beam maintains a narrow enough waist [29]. It is important when designing a light sheet microscope to determine what is an acceptable axial resolution and field of view and then choose a beam waist accordingly. Figure 2.3 (a) shows the relationship between beam waist and Rayleigh range.

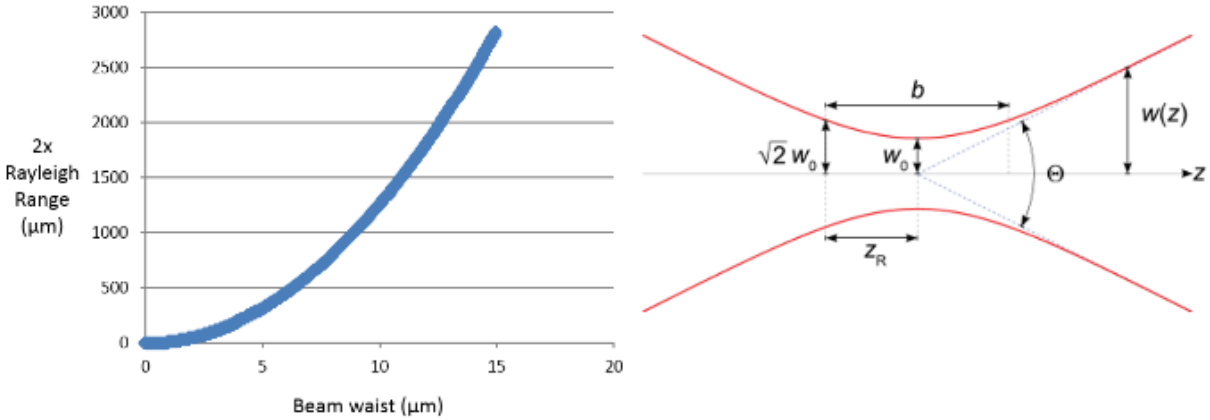

Figure 2.3: (a) is a graphical representation showing the value in microns of twice the Rayleigh range at a given beam waist. (b) is an illustration showing the relationship between the beam waist, Wo, and the Rayleigh range, Zr.

Methods have been developed to shape non- diffracting light beams. Bessel beams were applied in Betzig's structured illumination lattice light sheet microscope. True Bessel beams are completely non-diffracting. However, a true Bessel beam cannot be created experimentally. Bessel beam approximations are generated in practice by focusing a Gaussian beam with an axicon lens to generate a Bessel-Gauss hybrid beam. Another method to form a Bessel-Gauss beam is to illuminate a thin annulus shaped aperture or to use axisymmetric diffraction gratings. Bessel beams have the strength of maintaining a narrow waist but have very strong side lobes outside the central illumination beam. These side lobes excite fluorescence outside the detection focal plane. Another form of non-diffracting beams are Airy beams. Airy beams were successfully fabricated in 2007 by modulating a Gaussian beam with a spatial light modulator [18]. Dholakia used Airy beams to create a light sheet for sample illumination. Airy beams naturally curve as the beam propagates, which negatively effects the axial resolution of the microscope.

Microscope Objectives

Microscope objectives are optical elements that have a very high magnification with a very short focal length. The numerical aperture (NA) of a microscope objective typically ranges from 0.1 to 1.25 with focal lengths of about 40 mm to 2 mm. Certain objectives are designed for use in immersion mediums other than air such as oil and water. These mediums have an index of refraction greater than 1, which allows for an NA greater than 1.0. Many objectives are designed such that the high index light medium is placed between the objective and a coverslip. Objectives can also be fully immersed in a medium along with the sample, such as the objectives applied in this study. These objectives are referred to as dipping objectives. Microscope objectives play a large roll in light sheet microscopy for both sample illumination and image formation. Objectives must be chosen to have the proper magnification, NA, and working distance in the LSM to achieve the necessary performance required to efficiently resolve the sample. The working distance of microscope objectives detoured the breakthrough of light sheet microscopy until the early 2000's because objectives did not have long enough working distances to be placed in the perpendicular configuration as shown in Figure 2.2. Objectives are commonly applied in light sheet experiments to either create a light sheet or capture an image. The Huisken/Stelzer LSM used a cylindrical lens to form the light sheet while a single objective formed the image on the CCD camera. This LSM imaged the embryogenesis of *Drosophila melanogaster* in vivo. The objective used for this breakthrough system was a 40X magnification water dipping lens with an NA of 0.8. The OpenSpim platform applies high working distance and NA objectives for both illumination and detection in order to place both objectives in a perpendicular arrangement. The illumination objective (UMPLFLN 10XW) is a 10x objective with a working distance of 3.5 mm and NA of 0.3. The detection objective (UMPLFLN 20XW)

is a 20x objective with a working distance of 3.5 mm and NA of 0.5. The OpenSpim platform's microscope was designed to image Drosophila and zebra fish. Betzig's Lattice Light Sheet also used long WD objectives with high NA. The system used a custom manufactured excitation objective (Special Optics, 0.65 NA, 3.74 mm WD) and a Nikon detection objective (Nikon, CFI Apo LWD 25XW, 1.1 NA, 2 mm WD). The Lattice Light Sheet imaged embryogenesis in *Caenorhabditis elegans* and *Drosophila melanogaster*.

Optical Aberrations

Optical aberrations are distortions in light waves emitted from a source. Aberrations reduce the image quality and distort the captured scene. Refractive index mismatches in the sample are one of the greatest contributors to aberrations while imaging in microscopy. Different tissues within a biological specimen can vary in refractive index. This variation changes the optical path length causing the light rays of the wave to diverge from the focus. Mounting media and methods to hold the sample such as coverslips and FEP tubes also aberrate fluorescent light. Imperfection in optics and alignment are another cause of optical aberrations in a microscope system. Imaging deep into a biological specimen induces spherical aberration. Figure 2.3 shows a ray diagram illustrating spherical aberration caused by a lens. The index of refraction mismatch between the sample and the immersion medium is the cause of spherical aberration when imaging deep. Light rays traveling further from the principle axis will bend further due to the mismatch and an increase in depth causes more light rays to travel even further from the principle axis as the light propagates through the sample.

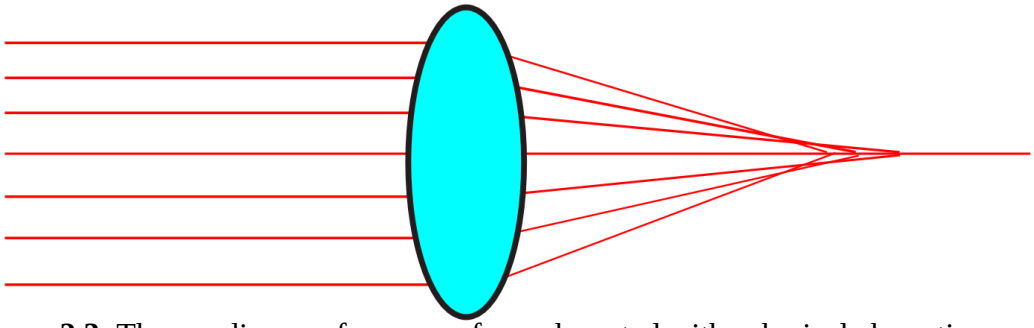

Figure 2.3: The ray diagram for a waveform aberrated with spherical aberration. Notice how the rays converge at different points along the principle axis. Light rays further from the principle axis intersect further from the ideal focal position.

Light rays further from the principle axis focus closer to the lens than the paraxial focal plane of the lens. The light rays are a geometric interpretation of the optical wavefront, in which all rays are perpendicular to the wavefront at that point in space. A Wavefront is a set of points on a light wave that all have the same phase. Ideal diffraction limited images have a flat wavefront that is focused by a lens to form a spherical wavefront that focuses to form an image with a high resolution. However, imaging systems are not completely aberration free and imaging deep within biological tissue causes large distortions to the wavefront due to the index of refraction inhomogeneity within the sample. These distortions in the optical wavefront lead to degraded image quality and resolution because of the correlation between the wavefront and the point spread function. An ideal flat wavefront has a point spread function the shape of an airy disk and provides the best resolution for diffraction limited imaging systems. Distortions from a flat wavefront also degrade the PSF resulting in lower image quality. Figure 2.4 shows simulations of three different wavefront shapes (flat, astigmatism, spherical aberration) and their resulting PSFs.

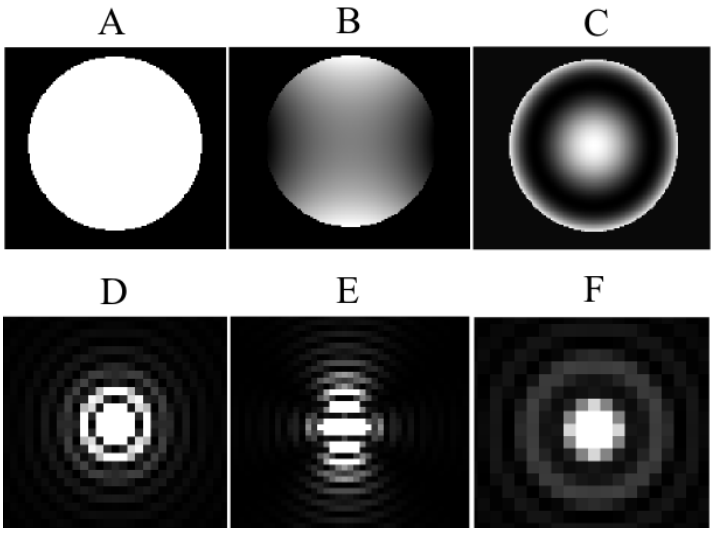

Figure 2.3: The top row (A-C) shows the phase values of wavefront within a back-pupil plane. The bottom row (D-E) shows the PSF for the corresponding pupil function above. (A&D) simulates a flat wavefront and its Airy disk PSF. (B&E) shows the effect of an astigmatic wavefront on the PSF and (C&F) shows spherical aberration.

Wavefronts and Zernike Polynomials

Frits Zernike invented a set of complete orthogonal mathematical functions defined on a circle. These functions are often used in optics to explain the shapes and modes of optical wavefronts. The lower order Zernike modes correspond to common optical aberrations. A wavefront can be expanded into a sum of weighted Zernike polynomials. There are an infinite number of them and the lower order terms are the most dominant, similar to a Taylor series. The first 10 Zernike polynomials are shown in Figure 2.5 (a) as well as a description of the aberration shape that mode corresponds to. These polynomials correspond to modes 0 through 9 using the Noll ordering [47]. Visual representations of these Zernike polynomials are shown in Figure 2.5 (b). These functions are useful for AO because the DM can be shaped to correct for given aberrations. An out of focus image can be brought back into focus by applying a set amplitude to Zernike number 4. The sample tube in LSM introduces astigmatism to the system that can be corrected, and spherical aberration due to deep tissue imaging can be corrected by applying Zernike mode 11 to the DM.

(a) **(b)**

Noll Index	Zernike	Classical name
1	1	Piston
2	$2\rho\cos()$	Tip
3	$2\sin()$	tilt
4	$\sqrt{3}(2\rho^2 - 1)$	Defocus
5	$\sqrt{6}(\rho^2)\sin(2)$	Oblique astigmatism
6	$\sqrt{6}(\rho^2)\cos(2)$	Vertical astigmatism
7	$\sqrt{8}(3\rho^3 - 2\rho)\sin()$	Vertical coma
8	$\sqrt{8}(3\rho^3 - 2\rho)\cos()$	Horizontal coma
9	$\sqrt{8}(\rho^3)\sin(3)$	Vertical trefoil
10	$\sqrt{8}(\rho^3)\cos(3)$	Oblique trefoil

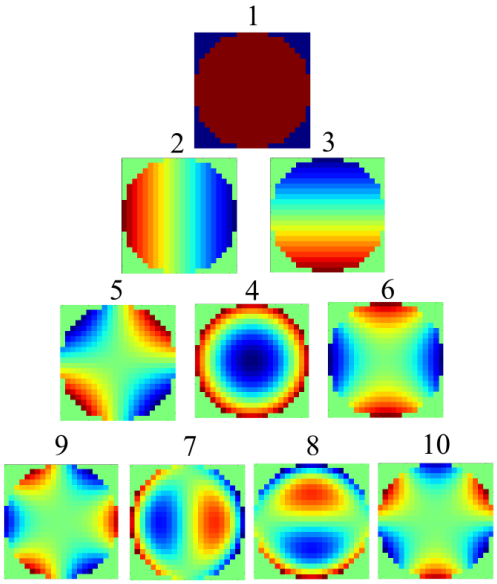

Figure 2.5: (a) is a table of the first 10 Zernike modes, the equation that represents it, and classical name describing the type of aberration. (b) is a visual representation of each mode.

saw important applications in astronomy before being adapted for microscopy. Light travels through the earth's atmosphere to reach the telescope when imaging distant celestial bodies, and atmospheric turbulence causes a refractive index mismatch, which leads to wavefront distortions as the light propagates. Adaptive optics refers to any system for correcting wavefronts to increase image quality by altering the elements of the system. Horace Babock proposed a method to enhance the performance of telescopes. He suggested applying a deformable optical element in combination with a wavefront sensor to correct wavefront distortions [19]. Advancements in micro-mechanical systems and computation have led to inventions, which make the idea of AO a reality. Figure 1.3 shows the experimental set up for an AO system. Figure 2.6 shows a non-corrected and corrected image of the planet Neptune.

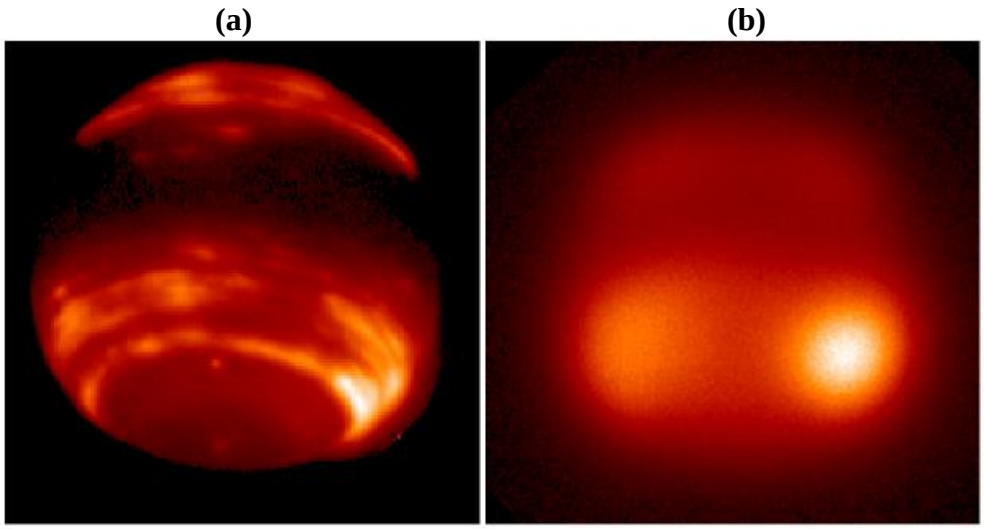

Figure 2.6: Images of Neptune capturing inferred light. Image (a) shows the image applying an adaptive optics correction. (b) show the image without correction [20].

Deformable Mirror

Deformable Mirrors are optical elements that can be locally deformed and have a wide variety of applications [21]. Different types of deformable mirrors include stacked array [30], bimorph [30], voice-coil [31], Micro Electro-Mechanical System (MEMS) [32, 33, 34], and optically addressed [35, 36] DMs. These types of deformable mirrors can be grouped into segmented and continuous surface deformable mirrors. Segmented deformable mirrors have individual reflective surfaces that can be raised or lowered individually. Continuous surface deformable mirrors comprise of a bendable surface membrane connected to an array of actuators. Modern deformable mirrors manufactured by companies such as Imagine Optic and Boston Micromachines are capable of correcting the aberrations caused during deep tissue imaging. The number of actuators defines the quality and the quantity of Zernike shapes the mirror can produce. As the number of actuators increases, so does versatility in deformation. Actuator stroke is the maximum possible actuator displacement and limits the maximum amplitude of the corrected wavefront.

Wavefront Measurement

Measuring the wavefront is a key component in an adaptive optics system to properly shape the deformable mirror for image correction. Methods for measuring the wavefront are generally defined in the category of Zonal or Modal wavefront sensing. Zonal sensing directly measure the wavefront by separating the pupil into an array of contiguous sub-apertures. The local gradient of each sub-aperture is independently measured then combined to reconstruct the entire wavefront. Types of Zonal sensors are the Shearing Interferometer [37], Pyramid [38], Foucault knife-edge [39], and Shack-Hartmann Wavefront Sensing [40]. Modal sensing estimates the wavefront based upon an image metric. This method of wavefront sensing has been successful in two photon and confocal microscopes because the imaged scene does not resemble a guide star. Modal wavefront calculation has the upsides of not requiring a sensor, however the calculation of the wavefront can require the detector to capture several images. Therefore, these methods can reduce the speed at which the detector captures corrected images. The sample will be susceptible to an increase phototoxicity due to the increase in the number of images taken.

Shack-Hartmann Wavefront Sensor

A very common Zonal wavefront sensor commonly applied in microscopy is the Shack-Hartmann Wavefront Sensor (SHWFS) [41, 42]. This type of sensor uses the combination of a micro-lenslet array and photodetector for measurement. Light interacts with the lenslet array as it propagates and each lens forms its own image or "sub-image" on the photodetector. Each sub-image will be shifted vertically and laterally depending on the local tip and tilt of the wavefront focused by the individual lenslet. An illustration of the physics is shown Figure 2.7. Routinely point sources are imaged with a SHWFS generating an array of dots on the detector. Local shifts can be determined for each spot using a centroid algorithm on each intensity distribution. The

phase of the wavefront can then be reconstructed from the gradient array using the Fourier transform [23] or Vector Matrix Multiplication (VMM) [46].

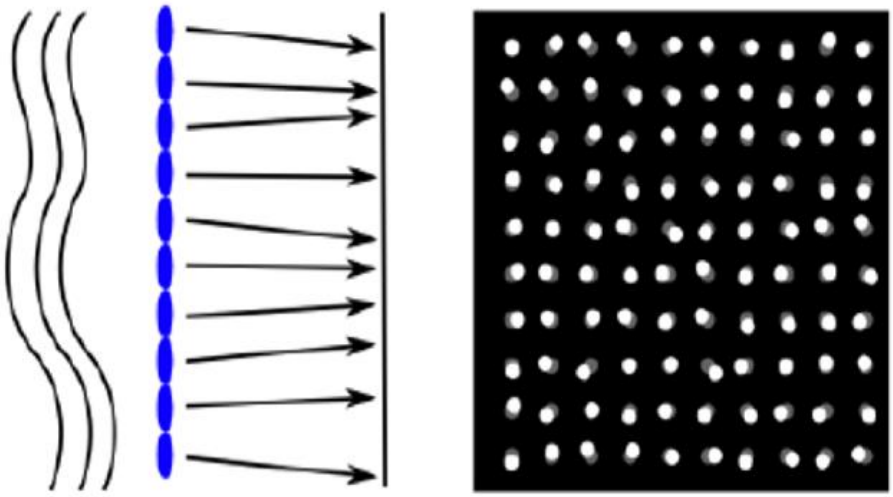

Figure 2.7: Illustrates the principle behind a Shack-Hartmann wavefront sensor. (a) shows how an aberrated waveform is locally focused by an individual lenslet based on the local shape of the light wave. (b) shows an example of a Shack-Hartmann image.

Influence Function

Actuator voltages of a continuous surface deformable mirror can be correlated to the mirror shape by developing a matrix called influence function, H, as shown in Equation (2.1). H is an (mxn) matrix where m is the total number of lenslets reconstructing the wavefront and n is the number of actuators. This influence function is determined by measuring an array of wavefronts with a set voltage applied to each actuator independently and the wavefront calculated for each prominence.

$$(H)*(A) = W \qquad (2.1)$$

Mirror actuator values, A, a 1xn matrix can be determined when correcting from a given wavefront, W, by solving for the inverse of the influence function matrix. W is the wavefront reshaped into a (1xm) matrix. The inverse of H is determined through singular value

decomposition. Multiplication of the inverse influence function with the wavefront result in an nx1 command vector to control the voltage of each actuator.

D. Rerio

D. rerio (zebrafish) are commonly applied in studies for biology. The genome has been fully sequenced for this particular model organism and has well-understood and easily observable developmental behavior. *D. rerio* have been used to make transgenic models of types of cancer, cardiovascular disease, infectious disease, and drug discoveries. The embryo of a zebrafish is transparent for several days post fertilization. Figure 2.8 shows zebrafish embryo images under a microscope at various early developmental stages. The zebra fish is about 4mm long and has a brain size of around 350 μm at an age of 5-7 days. The zebrafish is commonly imaged using a LSM and is observed in this study to understand seizure dynamics within zebrafish embryos. Dr. Jim Lauderdale at the University of Georgia provides the zebrafish for this study to advance his current work on the neuroscience of seizures [42, 43, 44].

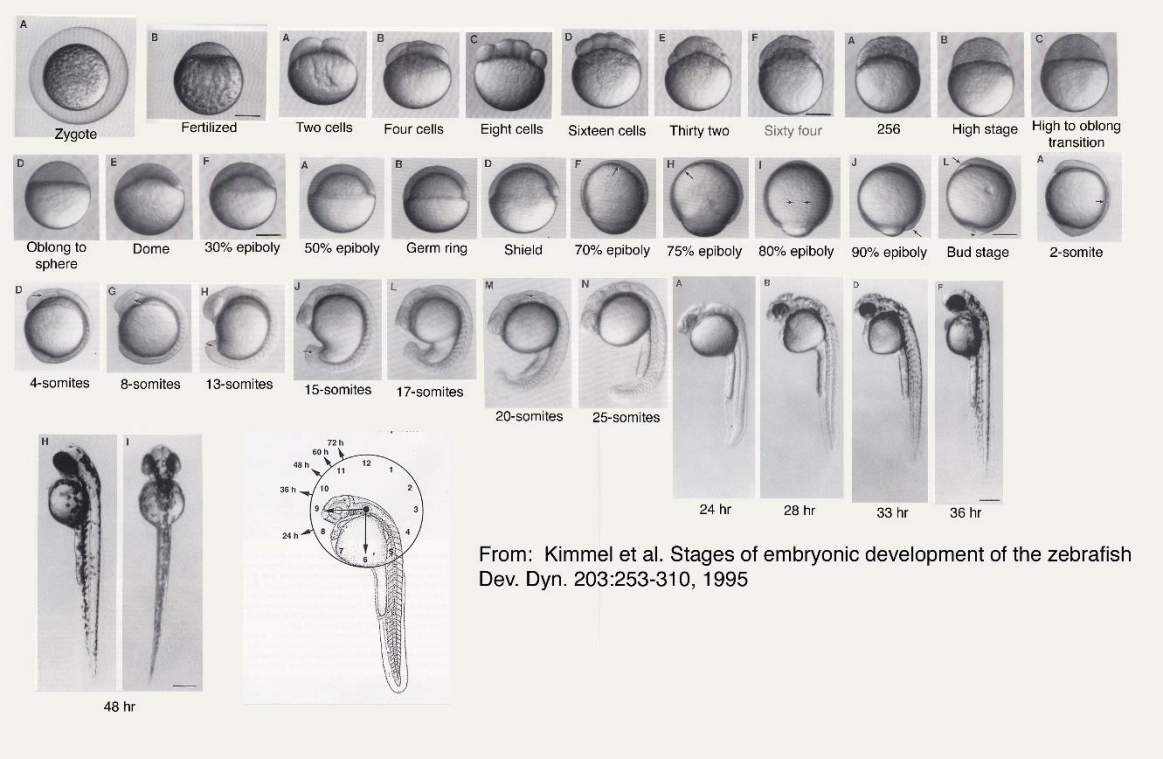

Figure 2.8: Diagram of the development of a zebra fish from the zygote state to 36 hours post fertilization [24].

References

12) Siedentopf H, Zsigmondy R. 1903. Über Sichtbarmachung und Groessenbestimmung ultramikroskopischer Teilchen, mit besonderer Anwendung auf Goldrubinglaesern. Annalen der Physik. 10:1-39 “English”

13) Voie, A. H., Burns, D. H., & Spelman, F. A. (1993), Orthogonal-plane fluorescence optical sectioning: three-dimensional imaging of macroscopic biological specimens, *Journal of Microscopy*

14) Huisken, J., Swoger, J., Del Bene, F., Wittbrodt, J. & Stelzer, E.H.K. Optical sectioning deep inside live embryos by selective plane illumination microscopy. *Science* **305**, 1007–1009 (2004).

15) Keller, P.J., Schmidt, A., Wittbrodt, J. & Stelzer, E.H.K. Reconstruction of zebrafish early embryonic development by scanned light sheet microscopy. *Science* **322**, 1065–1069 (2008).

16) L. Gao, L. Shao, B. C. Chen, E. Betzig, 3D live fluorescence imaging of cellular dynamics using Bessel beam plane illumination microscopy. Nat. Protoc. **9**, 1083–1101 (2014). doi:10.1038/nprot.2014.087 pmid:24722406

17) Vettenburg , T , Dalgarno , H I C , Nylk , J , Coll-Lladó , C , Ferrier , D E K , Cizmar , T , Gunn-Moore , F J & Dholakia , K 2014 , ' Light-sheet microscopy using an Airy beam ' Nature Methods , vol 11 , no. 5 , pp. 541-544 . DOI: 10.1038/nmeth.2922

18) Siviloglou, G.A., Broky, J., Dogariu, A. & Christodoulides, D.N. Phys. Rev. Lett. 99, 213901 (2007).

19) Hardy, J. W. 1998. Adaptive Optics for Astronomical Telescopes. New York, N. Y.: Oxford University Press

20) Max, C., University of California at Santa Cruz, Astronomy 289C

21) Enrique J. Fernández, Laurent Vabre, Boris Hermann, Angelika Unterhuber, Boris Považay, and Wolfgang Drexler, "Adaptive optics with a magnetic deformable mirror: applications in the human eye," Opt. Express **14**, 8900-8917 (2006)

22) *Platt, Ben C.; Shack, Ronald (October 2001). "History and Principles of Shack-Hartmann Wavefront Sensing". Journal of Refractive Surgery.* ***17*** *(5): S573–7. PMID 11583233*

23) Poyneer, L. A., Gavel, D. T., and J. M. Brase. 2002. Fast wave-front reconstruction in large adaptive optics systems with use of the Fourier transform. *J. Opt. Soc. Am*. Vol. 19, p.2100-2111

24) Kimmet et al. Stages of embryonic development of the zebrafish Dev. Dyn. 203:253-310, 1995

25) *Lakowicz, Joseph R. Principles Of Fluorescence Spectroscopy. New York :Kluwer Academic/Plenum, 1999. Print.*

26) Shimomura, O., F.H. Johnson, and Y. Saiga, *Extraction, Purification and Properties of Aequorin, a Bioluminescent Protein from the Luminous Hydromedusan, Aequorea*. Journal of Cellular and Comparative Physiology, 1962. **59**(3): p. 223-239.

27) Prasher, D.C., et al., *Primary structure of the Aequorea victoria green-fluorescent protein.* Gene, 1992. **111**(2): p. 229-233.

28) https://micro.magnet.fsu.edu/primer/lightandcolor/fluoroexcitation.html

29) *Siegman, A. E. (1986). Lasers. University Science Books. pp. 664–669. ISBN 0-935702-11-3.*

30) Sauvage, J.-F., et al., "SAXO, the eXtreme Adaptive Optics System of SPHERE: overview and calibration procedure", Proc. SPIE 7736, 77360F (2010).

31) Biasi, R., Gallieni, D., et al., "Contactless thin adaptive mirror technology: past, present and future", Proc. SPIE 7736, 77362B (2010).

32) Cornelissen, S., A., et al., "MEMS Deformable Mirrors for Astronomical Adaptive Optics", Proc. SPIE 7736, 77362D (2010).

33) Helmbrecht, M., A., et al., "MEMS DM development at Iris AO, Inc", Proc. SPIE 7931, 793108 (2011).

34) Hamelinck, R., et al., "Electromagnetic DM technology meets future AO demands", in the 1st AO4ELT Conference - Adaptative Optics for Extremely Large Telescopesproceedings, 2010, edited by Y. Clénet, J.-M. Conan, T. Fusco and G. Rousset, published by EDP Sciences (ao4elt.edpsciences.org)

35) Davies, D., W., Shimizu, J., A., "Optical processor for controlling a deformable mirror", US Patent #5,166,508 (Nov. 24, 1992)

36) Schiller, C., M., et al., "Charge-transfer-plate deformable membrane mirrors for adaptive optics applications", Proc. SPIE 1543, 120 (1992)

37) W. H. Southwell, "Wave-front estimation from wave-front slope measurements," *Journal of the Optical Society of America,* vol. 70, pp. 998-1006, 1980.

38) C. Vérinaud, "On the nature of the measurements provided by a pyramid wave-front sensor," *Optics Communications,* vol. 233, pp. 27-38, 3/15/ 2004.

39) H. W. Babcock, "THE POSSIBILITY OF COMPENSATING ASTRONOMICAL SEEING," *Publications of the Astronomical Society of the Pacific,* vol. 65, pp. 229-236, 1953.

40) B. C. Platt and R. Shack, "History and principles of Shack-Hartmann wavefront sensing," *J Refract Surg*, vol. 17, pp. S573-7, Sep-Oct 2001.

41) J. L. Beverage, R. V. Shack, and M. R. Descour, "Measurement of the three-dimensional microscope point spread function using a Shack-Hartmann wavefront sensor," *J Microsc*, vol. 205, pp. 61-75, Jan 2002.

42) O. Azucena, J. Kubby, J. Crest, J. Cao, W. Sullivan, P. Kner, *et al.*, "Implementation of a Shack-Hartmann wavefront sensor for the measurement of embryo-induced aberrations using fluorescent microscopy," in *MEMS Adaptive Optics III*, San Jose, CA, USA, 2009, pp. 6-9.

43) Johnston, L., Ball, R.E., Acuff, S., Gaudet, J., Sornborger, A., and Lauderdale, J.D. (2013) Electrophysiological recording in the brain of intact adult zebrafish. Journal of visualized experiments : JoVE. (81):e51065

44) Tao, L., Lauderdale, J.D., and Sornborger, A.T. (2011) Mapping Functional Connectivity between Neuronal Ensembles with Larval Zebrafish Transgenic for a Ratiometric Calcium Indicator. Frontiers in neural circuits. 5:2

45) Fan, X., Majumder, A., Reagin, S.S., Porter, E.L., Sornborger, A.T., Keith, C.H., and Lauderdale, J.D. (2007) New statistical methods enhance imaging of cameleon fluorescence resonance energy transfer in cultured zebrafish spinal neurons. Journal of Biomedical Optics. 12(3):034017

46) Jan Herrmann, "Least-squares wave front errors of minimum norm," J. Opt. Soc. Am. **70**, 28-35 (1980)

47) *Noll, R. J. (1976). "Zernike polynomials and atmospheric turbulence" (PDF). J. Opt. Soc. Am.* ***66*** *(3): 207. Bibcode:1976JOSA...66..207N. doi:10.1364/JOSA.66.000207*

CHAPTER 3:

SHACK-HARTMANN WAVEFRONT SENSING THEORY

In this chapter, we discuss the Shack-Hartman Wavefront Sensor (SHWFS) theory applied for this study. We begin the chapter introducing the concept of the Shack-Hartmann wavefront sensor and how the sensor is able to measure the optical wavefront. We then discuss in detail how gradients are measured and calculated from an array of shifted scenes captured by the camera. Next we discuss the reconstruction of a wavefront from a given set of Shack-Hartmann gradients using the Fast Fourier Transform. We then discuss how to eliminate artifacts in the wavefront caused by the reconstruction. Finally, we demonstrate the effectiveness of scene-based Shack-Hartmann wavefront sensing through simulation.

Shack-Hartmann Introduction:

The purpose of a SHWFS is to be able to measure the optical wavefront within an imaging system such that the distortions of the light wave can be corrected using AO. The sensor consists of two major components, lenslet array and photodetector. The lenslet array samples the light over the entire aperture. Light within a local lenslet will form its own image on the photodetector that is locally shifted based on the sampled wavefront shape. Figure 2.7 (a) from Chapter 2 shows how the wavefront is sampled by the lenslet array. Figure 2.7 (b) illustrates an example SHWFS image generated by the photodetector. The goal of the sensor is to reconstruct the optical wavefront from the detector's produced signal, an image of individually spaced scenes produced by the lenslet array. The idea is that local displacement values for each image have a direct relationship to the local phase of the wavefront within that sub aperture. The local

position of each scene can be determined through many mathematical techniques that we will discuss in this chapter. Once a set of gradients is determined, a wavefront can be reconstructed by use of the Fourier-Transform. The DM shape is set to the opposite profile of the measured wavefront to compensate the aberrations.

Determining Local Shifts:

This section discusses methods to sense the wavefront gradients used to reconstruct the wave's phase. Shack-Hartmann wavefront sensors are generally employed to image guide-stars as shown in figure 2.7 (b) which illustrates a Shack-Hartmann Wavefront Sensor imaging a point like object. The reasoning is because the objects location can be accurately determined using a center of mass calculation as shown in equations (3.1) and (3.2) for both x and y coordinates respectively. m_i is the intensity measurement for the pixel, $x_i$is the horizontal position of the pixel, and $y_i$is the vertical position of the pixel. This method is very accurate due to the symmetry of the intensity distribution while imaging guide-stars.

$$\bar{x} = \frac{\sum_{i=1}^{n} m_i x_i}{\sum_{i=1}^{n} m_i} \qquad (3.1)$$

$$\bar{y} = \frac{\sum_{i=1}^{n} m_i y_i}{\sum_{i=1}^{n} m_i} \qquad (3.2)$$

There are other methods to determining local shifts for the SHWFS. One method to improve on the center of mass technique is to first apply a global threshold at the noise level of the system [53]. Another technique applied for measuring gradients is by implementing a Gaussian weighed centroid algorithm, where local shifts are characterized by its full-width-at-half-maximum (FWHM). A separate technique examines the similarity between Shack-Hartmann sensing and carrier frequency interferometry to determine the wavefront [56,57,58]

However, if a SHWFS is to be used on a general scene to determine local gradients, then another algorithm besides a center of mass calculation needs to be implemented. Applying a

cross correlation over centroid methods was proposed by Poyneer [52]. Cross-correlation is a mathematical operation that measures the area overlap of two signals as a function of lag between the signals. Equation 3.3 defines the discrete method for calculating a cross-correlation between two signals, f and g. The Cross-Correlation between two similar images will produce a well-defined peak whose position determines local shifts.

$$(f * g)[n] \stackrel{\text{def}}{=} \sum_{m=-\infty}^{m=\infty} f^*[m]\, g[m+n] \qquad (3.3)$$

Figure 3.1 is a simulation to demonstrate how the cross-correlation can be used to determine shifts in intensity distributions by observing the location of the cross-correlation's maximum value. Figure 3.1 (a) illustrates an auto-correlation of two pixelated images. Figure 3.1 (b) shows the cross-correlation between two images where the intensity distributions are shifted spatially. The result of an auto-correlation will always have its maximum area overlap at the center of the cross-correlation. If two images differ only in a rigid shift of one of the images then the magnitude and direction of the shift is related the location of the maximum value of the two images' cross-correlation. This property is illustrated in Figure 3.1 (b). Images 1 and 2 only differ by a shift in intensity. Image 2 is shifted 3 pixels higher in the x and y direction. The location of the maximum value of the two images' cross-correlation is shifted with the same magnitude and direction.

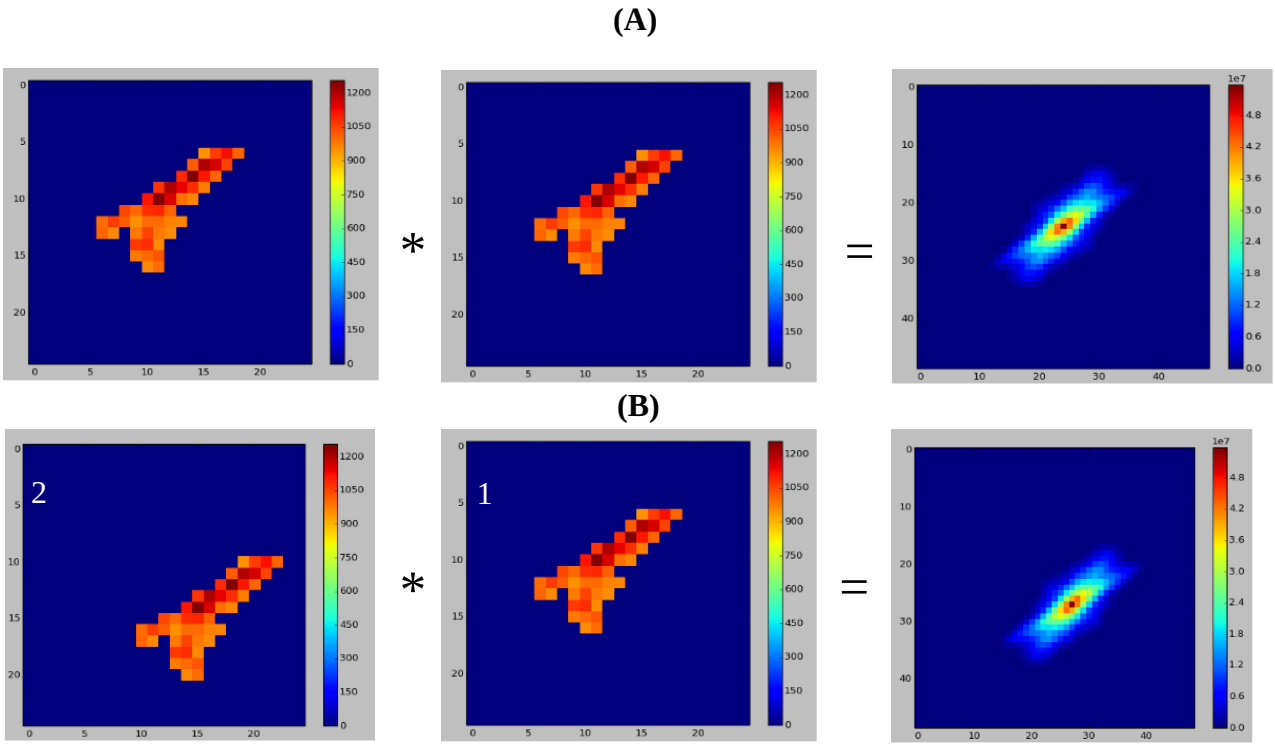

Figure 3.1: Demonstration of how applying the cross correlation can determine the shift between images 1 and 2. (a) illustrates an autocorrelation. The result has its maximum value in the result's center. (b) illustrates a cross correlation where the images differ by a rigid pixel shift in the x and y direction.

Relying solely on the maximum value location of the cross-correlation can only detect shifts with a resolution of a pixel, which will not be accurate enough for our SHWFS system. Performing a parabolic fit over a local neighborhood centered on the location of the maximum cross-correlation value is a useful method for estimating sub-pixel shifts [52]. Equation (3.4) and (3.5) give the shift estimates $\hat{x}_o$ and $\hat{y}_o$ respectively for a given discrete correlation C[m,n]. Fitting a parabola to a 3x3 neighborhood centered at the signal's peak value location $[\Delta_x,\Delta_y]$ gives the final shift estimate in pixels.

$$\hat{x}_o = \Delta_x + \frac{0.5(C[\Delta_x-1,\Delta_y]-C[\Delta_x+1,\Delta_y]}{C[\Delta_x-1,\Delta_y]+C[\Delta_x+1,\Delta_y]-2C[\Delta_x,\Delta_y]} \quad 3.4$$

$$\hat{y}_o = \Delta_y + \frac{0.5(C[\Delta_x,\Delta_y-1]-C[\Delta_x,\Delta_y+1]}{C[\Delta_x,\Delta_y-1]+C[\Delta_x,\Delta_y+1]-2C[\Delta_x,\Delta_y]} \quad 3.5$$

The discussed method determines sub-image shifts between a reference base-image and an aberrated offset-image. This two-image comparison method compares the (i,j) lenslet in the base image with the (i,j) lenslet of the offset image . Local shifts in each corresponding lenslet can be determined by cross-correlating the (i,j) Shack-Hartmann sub-image of the base image with the (i,j) Shack-Hartmann sub-image of the offset image. The local shift for that local aperture is determined using the methods above. When using a single image to determine the wavefront, another method needs to be used due to the lack of a reference image. Instead, each sub-image is correlated with a reference lenslet, usually the center, when using a single image to determine the wavefront. The resulting x and y gradients are reduced by the median value of each set. The reason to perform the median reduction is due to the bias the reference sub-image has on calculating the gradients. The local position of the reference sub-image's intensity distribution will skew the gradients in the direction such that the gradient for the reference sub-image is zero. This is because the reference sub-image will always undergo an autocorrelation regardless of the scene's shift or local wavefront slope that forms the reference sub-image. This method is successful for determining gradients using a single image at the cost of sensing Zernike modes corresponding to tip and tilt.

The gradient values determined by applying cross-correlation and parabolic fitting can be converted from a shift in pixels to a change in phase. The relationship between a pixel shift (g), wavefront gradient, θ, and wavefront phase, Φ, with a pupil diameter, p, for a lenslet with focal length, f, is illustrated in Figure 3.2. Equation 3.6 relates the wavefront phase to the pixel shift,

lenslet focal length, and pixel width (L). Equation 3.7 is the relationship between wavefront phase to the wavefront gradient and pitch of the lenslet array (P).

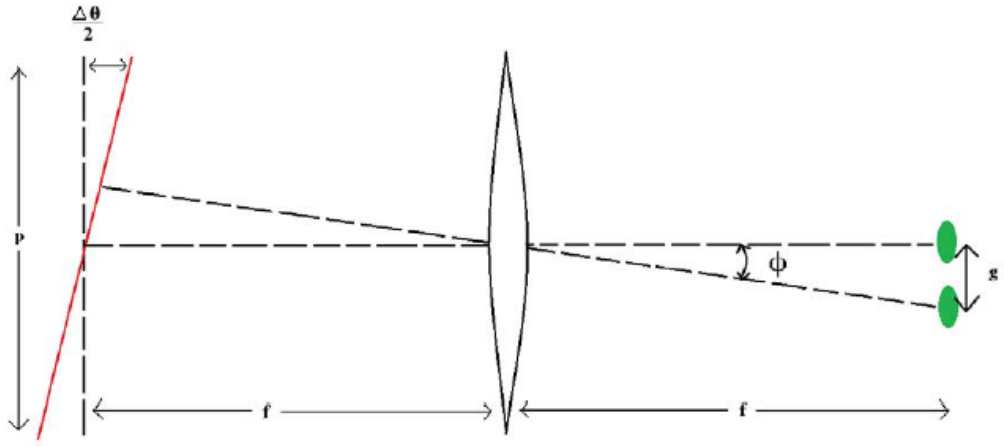

Figure 3.2: Illustration showing the relationship between a pixel shift (g) and wavefront gradient (θ)

$$\Phi = \left(\frac{gL}{f}\right) \qquad 3.6$$

$$\Delta\theta = P\Phi \qquad 3.7$$

Reconstruction

The end goal is to reconstruct the phase measurement of the wavefront from the gradients measured by the SHWFS, which are proportional to local slopes in the wavefront. This section discusses methods of reconstructing a wavefront from a set of x and y gradients. The reconstructed wavefront is represented as an array of equidistant nodes. The sub-aperture geometry of the sensor affects the solution to the reconstructed phase. One proposed geometry is due to Hudgins. For this geometry, wavefront phase values are centered between each pair of points. Another configuration is the Fried Geometry. The Fried geometry is modeled as the average of the two nearest first differences. Both geometries result in wavefront reconstructions with a low residual mean square error and are illustrated in Figure 3.3 [48]

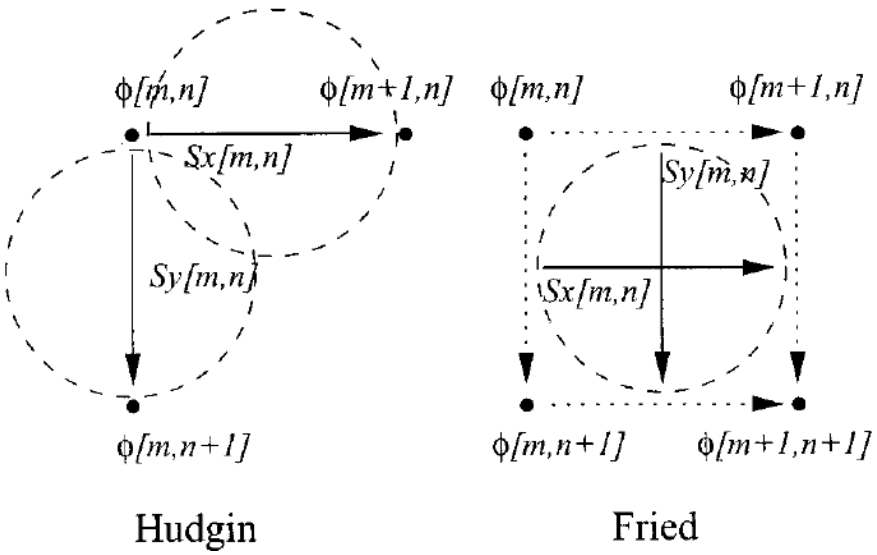

Figure 3.3: Illustration of the Hudgin geometry. The dashed circles represent Shack-Hartmann wavefront sensor locations [49].

Equation 3.8 and 3.9 show the modeled gradients using first differences between adjacent phase points. $s_x[m,n]$ and $s_y[m,n]$ are the x and y gradients for a set of phase values ϕ[m,n].

$$s_x[m,n] = \phi[m+1,n] - \phi[m,n] \qquad (3.8)$$

$$s_y[m,n] = \phi[m,n+1] - \phi[m,n] \qquad (3.9)$$

There are many methods developed for reconstructing the wavefront from gradients measured by the SHWFS. It is possible to represent the relationship between the wavefront nodes and gradient array as a system of linear equations as shown in Equation 3.10. (ŝ) is a vector of gradient measurements, (H) is a matrix based on the geometry of the sensor, (w) is a vector of wavefront nodes, and (n) is the noise of the system, Multiplying both sides of the equation by the transpose of A and then inverting the result is one method to solve the equation [14].

$$\hat{s} = Hw + n \qquad (3.10)$$

However, reconstruction time applying vector-matrix-multiplication for n number of actuators scales as $O(n^2)$. Applying the Fast Fourier Transform (FFT) for wavefront

reconstruction scales as *O(nlogn)* for power-of-2-sized grids [49]. Processing time when applied to AO systems with higher number of correctable elements is faster. Equations 3.8 and 3.9 can be solved with the shift property of the Fourier Transform for determining the wavefront. Equations 3.11 and 3.12 result from taking the Discrete Fourier Transform of Equation 3.8 and 3.9 respectively.

$$S_x[k,l] = \Phi[k,l]\left[\exp\left(\frac{j2\pi k}{N}\right) - 1\right] \qquad (3.11)$$

$$S_y[k,l] = \Phi[k,l]\left[\exp\left(\frac{j2\pi l}{N}\right) - 1\right] \qquad (3.12)$$

Multiplying Equations 3.11 and 3.12 by the complex conjugate of the exponential term and combining the results allows for us to solve for $\widehat{\Phi}[k,l]$ as shown in equation 3.13.

$$\widehat{\Phi}[k,l] = \begin{cases} 0, & k,l = 0 \\ \left\{\left[\exp\left(-\frac{j2\pi k}{N}\right) - 1\right] S_x[k,l] + \left[\exp\left(-\frac{j2\pi l}{N}\right) - 1\right] S_y[k,l]\right\} & \\ \quad x\left[4\left(\sin^2\frac{\pi k}{N} + \sin^2\frac{\pi l}{N}\right)\right]^{-1}, & \text{else} \end{cases} \qquad (3.13)$$

Equation 3.13 gives the formula for wavefront reconstruction using Hudgins geometry. We will now derive the reconstruction equation while using the Fried geometry starting with the inverse spatial filter shown in equations 3.14 and 3.15.

$$s_x[m,n] = \frac{1}{2}(\phi[m+1,n] - \phi[m,n] + \phi[m+1,n+1] - \phi[m,n+1]) \qquad (3.14)$$

$$s_y[m,n] = \frac{1}{2}(\phi[m,n+1] - \phi[m,n] + \phi[m+1,n+1] - \phi[m+1,n]) \qquad (3.15)$$

Once again these equations can be rewritten as the using the Fourier theory and an equation for the inverse spatial filter to reconstruct the wavefront using the same method as the Hudgin's geometry. Equation 3.16 shows the equation for the reconstructed phase when using the Fried geometry.

$$\widehat{\Phi}[k,l] = \begin{cases} 0, k, l = 0, k, l = N/2 \\ \left\{ \begin{array}{l} \left[\exp\left(-\frac{j2\pi k}{N}\right) - 1\right]\left[\exp\left(-\frac{j2\pi l}{N}\right) + 1\right] S_x[k,l] \\ + \left[\exp\left(-\frac{j2\pi l}{N}\right) - 1\right]\left[\exp\left(-\frac{j2\pi l}{N}\right) + 1\right] S_y[k,l] \end{array} \right\} \\ x \left[8\left(\sin^2\frac{\pi k}{N}\cos^2\frac{\pi l}{N} + \sin^2\frac{\pi l}{N}\cos^2\frac{\pi k}{N}\right)\right]^{-1}, \text{else} \end{cases} \quad (3.16)$$

These reconstruction methods were derived for a rectangular grid of gradient measurements. However, Shack-Hartmann systems in microscopy typically sense the wavefront over a circular aperture. Zero padding the unused gradient positions will result in an increase in RMS error. One method of obtaining a consistent set of gradients is the extension method [49]. This method was designed to be consistent with assumptions made when reconstructing with the FFT. The assumptions are that the reconstructed phase is spatially periodic and that any closed path of gradients must sum to zero [50, 51]. The method extends the inside gradients at the edge of aperture and is illustrated in Figure 3.2. The x gradients are extended up and down out of the aperture while the y gradients are extended to the left and right. This method is consistent with the spatial periodicity assumption because the extended gradients from opposite sides connect to form seam gradients. Setting the seams to have gradient values in which the sum of each row and column total to zero ensures spatial periodicity. The loop-continuity condition is also met and can be observed in Figure 3.4 by summing gradient values for any closed loop and confirming that they sum to zero.

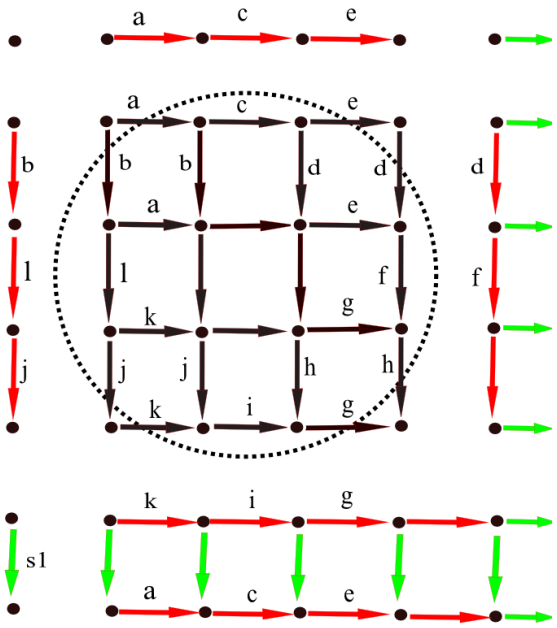

Figure 3.4: Illustration showing the Extension method. Gradient values closest to the edge of the aperture are repeated to spread outside the aperture.

Errors arise during wavefront sensing from noise in gradient measurements. Variations from point to point result in a waffle component in the reconstructed wavefront. Waffle noise can be thought of as a repeated pattern of alternating high and low values over the entire aperture and the pattern has the same frequency as the phase positions. The extension method results in an increase in error as noise becomes more relevant because loop continuity will no longer be preserved at the seam gradients. Processing each phase value independently can result in waffle errors that vary across the aperture. Figure 3.5 is an illustration of waffle error, which resembles a checkerboard pattern of high and low values. This waffle component could be removed in the frequency domain by removing the frequency component associated with the waffle. However, removing high-frequency components can greatly deteriorate sharp features and edges in the image. Instead we employ a method that removes global waffle in the spatial domain by generating a waffle pattern across the aperture. The coefficient for global waffle can be determined through Equation 3.17. $\hat{\phi}$ is the original wavefront. v is the waffle-mode of interest

with a value of 1 or -1 depending on position. Equation 3.18 shows the wavefront estimate with waffle mode removed.

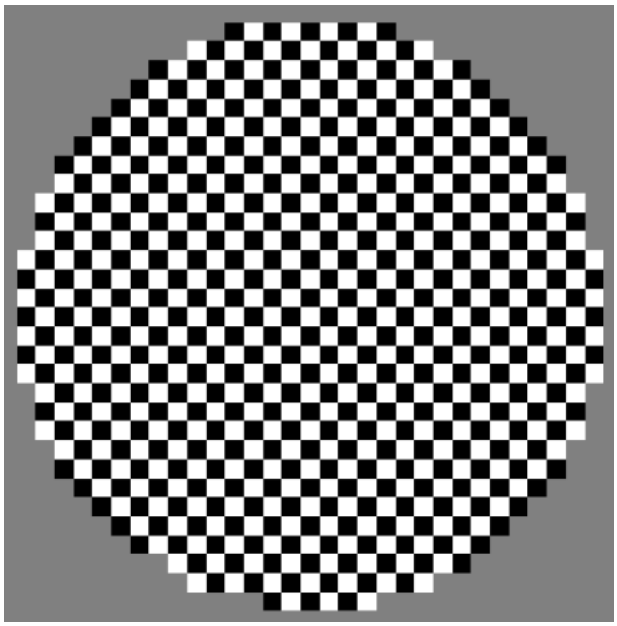

Figure 3.5: Illustration of the shape waffle errors take. Noise values alternate between high and low values across the sensor.

$$c_v = \frac{\sum_{m=0}^{N-1}\sum_{n=0}^{N-1}\hat{\phi}[m,n]v[m,n]}{\sum_{m=0}^{N-1}\sum_{n=0}^{N-1}v[m,n]v[m,n]} \qquad (3.17)$$

$$\phi_{-v}[m,n] = \hat{\phi}[m,n] - c_v v[m,n] \qquad (3.18)$$

We demonstrate the effectiveness of Poyneer's waffle removal estimate through simulation. Figure 3.6 (a) illustrates a parabolic wavefront with no noise. Figure 3.6 (b) is the same wavefront, but with a waffle component added to the phase. The waffle has a strength ranging from -0.005 to 0.005. Figure 3.6 (c) shows the filtered wavefront with waffle removed using equations 3.17 and 3.18. Figure (d) is the difference image between (c) and (b) and shows the waffle removed from the wavefront.

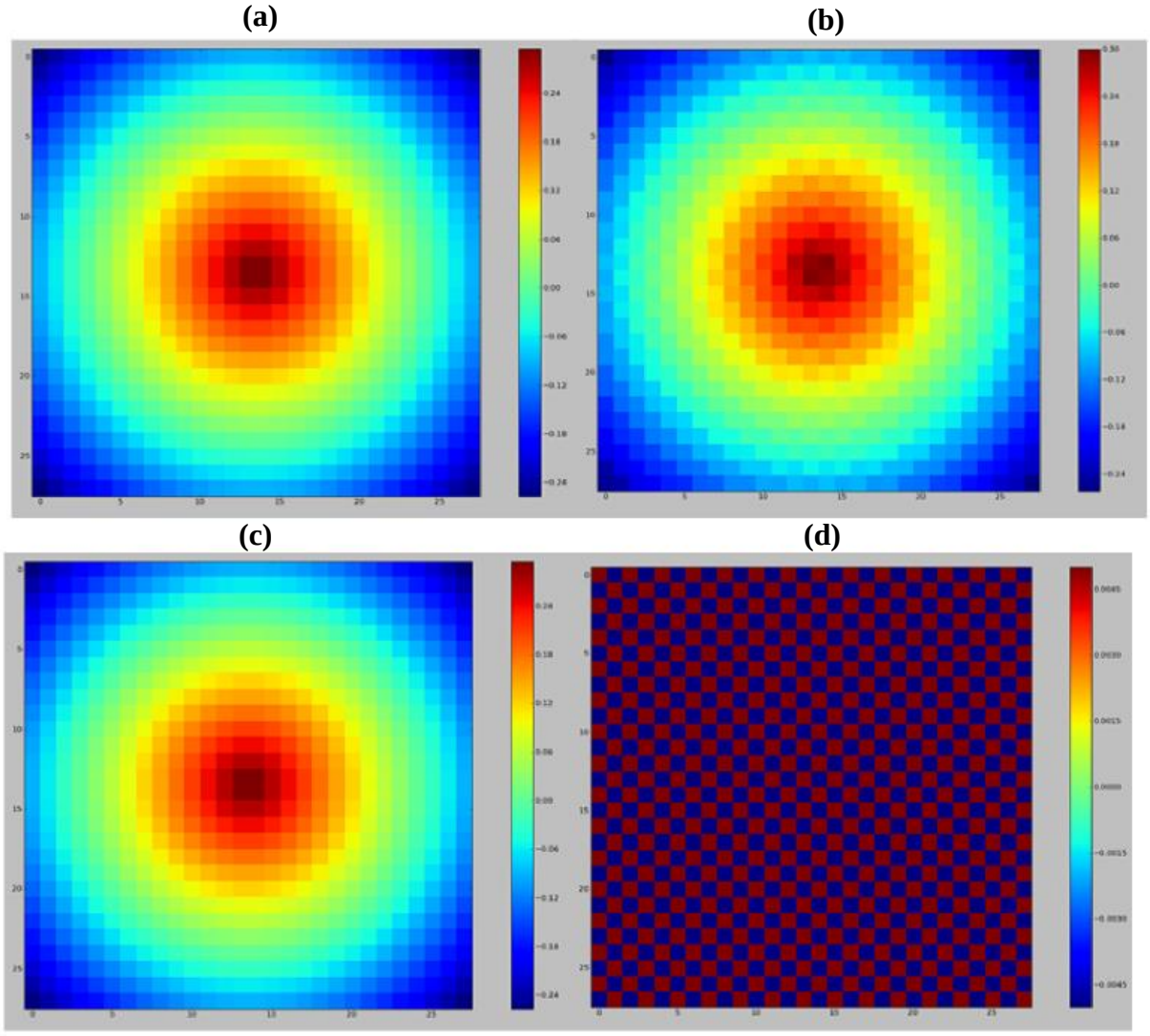

Figure 3.6: Simulations demonstrating Global waffle removal. (a) Parabolic wavefront with no noise. (b) shows the simulated wavefront with global waffle with a strength of -.005 to 0.005 phase units. (c) is the wavefront after the waffle is removed using equations 3.17 and 3.18. (d) is a difference image between the (c) and (b) which is equal to the waffle pattern added.

Wavefront Sensing Simulation

This section is dedicated to applying everything discussed in this chapter to reconstruct the wavefront from 2 simulated Shack-Hartmann images. Figure 3.7 (a) shows a simulated Shack-Hartmann image of a general scene applied to generate each subimage of a SHWFS

signal. The Shack-Hartmann image shown in Figure 3.7 (b) has subpixel lenslet shifts corresponding to an astigmatic wavefront which was compared to a flat wavefront image. Figure 3.7 (c) shows the reconstructed wavefront in pixels applying the cross correlation for gradient measurement and methods for reconstruction mentioned in the earlier sections of this chapter.

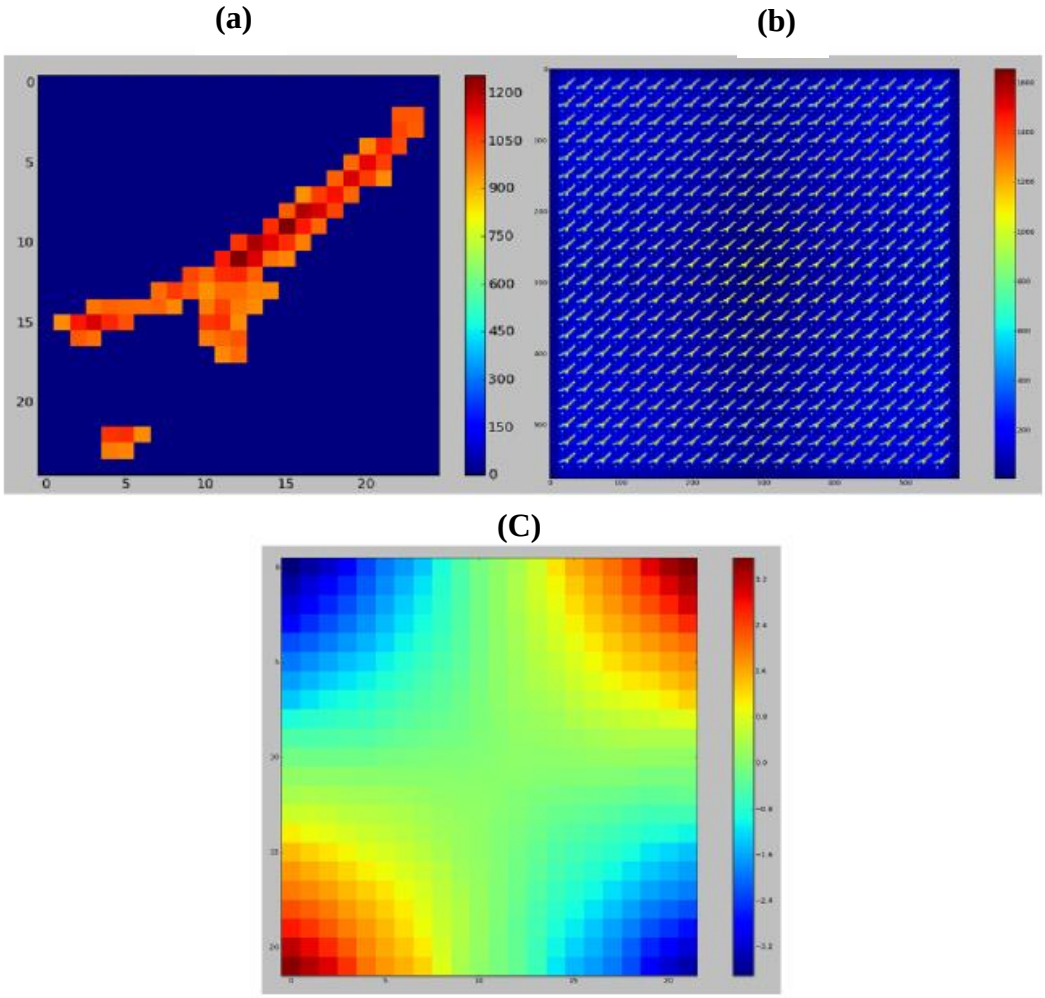

Figure 3.7: (a) shows the image used as a subimage to generate an array of shifted images formed from a lenslet array. (b) is the simulated SHWFS image. (c) is the reconstructed wavefront in pixels of image (b) and illustrates the astigmatic wavefront that would generate the SH signal shown in (b).

References

48) R. H. Hudgin, “Wave-front reconstruction for compensated imaging,” J. Opt. Soc. Am. 67, 275-378 (1977)

49) Poyneer, L. A., Gavel, D. T., and J. M. Brase. 2002. Fast wave-front reconstruction in large adaptive optics systems with use of the Fourier transform. *J. Opt. Soc. Am*. Vol. 19, p.2100-2111

50)K. Freischlad and C. L. Koliopoulos, “Wavefront reconstruction from noisy slope of difference data using the discrete Fourier transform,” in *Adaptive Optics*, J. E. Ludman, ed., Proc. SPIE **551**, 74-80 (1985)

51) K. Freischlad and C. L. Koliopoulos, “Wavefront integration from difference data,” in *Interferometry: Techniques and Analysis*, G. M. Brown, O. Y. Kwon, M. Kujawinska, and G. T. Reid, eds., Proc. SPIE **1755**, 212-218 (1992)

52) Poyneer, L. A. (2003). "Scene-based Shack-Hartann wave-front sensing: analysis and simulation." Applied Optics 42(29): 9.

53) J. Arines and J. Ares, “Minimum variance centroid thresholding,” Opt. Lett. 27, 497 (2002).

54) M. Nicolle, T. Fusco, G. Rousset, and V. Michau, “Improvement of Shack-Hartmann wave-front sensor measurement for extreme adaptive optics,” Opt. Lett. 29, 2743 (2004).

55) T. Fusco, M. Nicolle, G. Rousset, V. Michau, J.-L. Beuzit, and D. Mouillet, “Optimisation of a ShackHartmann-based wave-front sensor for XAO system,” SPIE 5490, 1155 (2004).

56) Y. Carmon and E. N. Ribak, “Phase retrieval by demodulation of a Hartmann–Shack sensor,” Opt. Commun. 215, 285 (2003)

57) S. Velghe, J. Primot, N. Guérineau, M. Cohen, and B. Wattellier,, “Wave-front reconstruction from multidirectional phase derivatives generated by multilateral shearing interferometers,” Opt. Lett. 30, 245 (2005)

58) M. Kujawinska, in Interferogram Analysis, edited by David W Robinson and Graeme T Reid (Institute of Physics Publishing, Bristol and Philadelphia, 1993).

59) D. L. Fried, "Least-square fitting a wave-front distortion estimate to an array of phase-difference measurements, " J. Opt. Soc. Am. **67**, 370-375 (1977)

CHAPTER 4:

OPTICAL DESIGNS AND EXPERIMENTAL SET-UPS

In this chapter, we discuss the designs of experimental set ups that led to the creation of the LSM incorporating AO. For each set-up, we will discuss the details of each component and reasoning behind its selection. We begin illustrating the optical design and experimental setup of a Shack-Hartmann wavefront sensor. Second, we review the DM used in this study. Third, we discuss a closed-loop adaptive optics evaluation set up designed to test algorithms and physical performance of the deformable mirror in combination with a SHWFS for wavefront sensing and correction. Fourth, we discuss the optical and mechanical design of a LSM based off an open source design. Finally, we reveal the optical and mechanical design for the experimental set-up that combines closed-loop AO with the LSM.

Shack Hartmann Wavefront Sensor Design and Setup:

Figure 4.1 illustrates the setup of a Shack-Hartmann wavefront sensor. The pupil plane is imaged onto the lenslet array. The focal plane of the lens-let array is reimaged onto a photo detector using a matched pair. The matched pair is necessary due to the focal length of the lenslet array being less than 10 mm while the CCD chip of the camera is deeper than that distance inside the camera body.

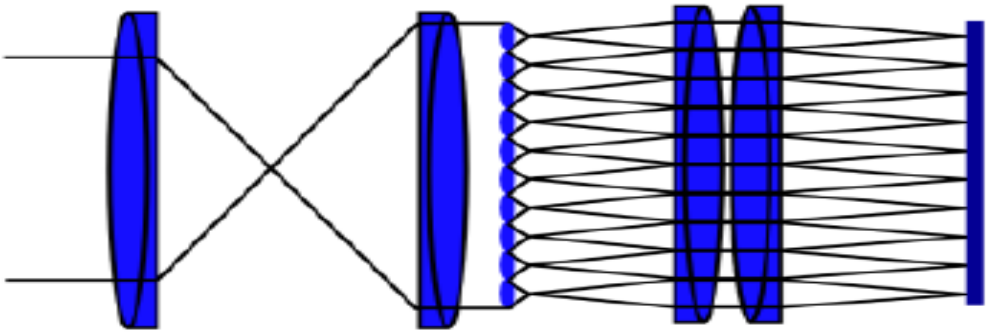

Figure 4.1: Illustration behind the experimental setup of a Shack-Hartmann wavefront sensor. Propagating light is relayed onto a lens-let array.

Closed Loop Adaptive Optics Test Bed:

A Closed Loop Adaptive Optics system designed to demonstrate the effectiveness of our methods is shown in Figure 4.3. The purpose of this set up is to evaluate the physical performance of the wavefront sensor and deformable mirror, as well as ensure proper execution of algorithms discussed in the background. The SHWFS applied in this setup uses a 150 μm pitch lenslet array (Thorlabs MLA150-7AR) mounted in a rotation mount (Thorlabs RSP1x15/M), one-to-one matched pair (Thorlabs MAP105050-A), and a pike CCD camera (Pike F-032 B) in the configuration discussed in the previous section. Light from a 543nm helium neon laser is expanded by 20mm focal length lens followed by a 300mm to fully illuminate the deformable mirror. A 4f relay system consisting of a 400mm followed by 300mm focal length lenses image the DM onto the lenslet array of the SHWFS. The magnification due to this 4f lens pair reduces the active actuator pupil to a diameter of 3.6 mm. There are two reasons for choosing this magnification. One is that a pupil of 3.6 mm illuminates 22 lenslets in the linear direction and maintains the Hudgins geometry discussed in Chapter 2. Second, the range of lenslets that can be illuminated is limited by the physical size of the pike CCD chip inside the camera. Each DM actuator is sampled by 2 lenslets. The actuators located at the corner of the

deformable mirror are conjugate to the corner lenslets illuminated by the active actuator pupil. Each lenslet has a focal length of 6.7mm, a NA of 0.0108, and corresponds to 20.25 CCD pixels per lenslet and a resolution of around 25 μm.

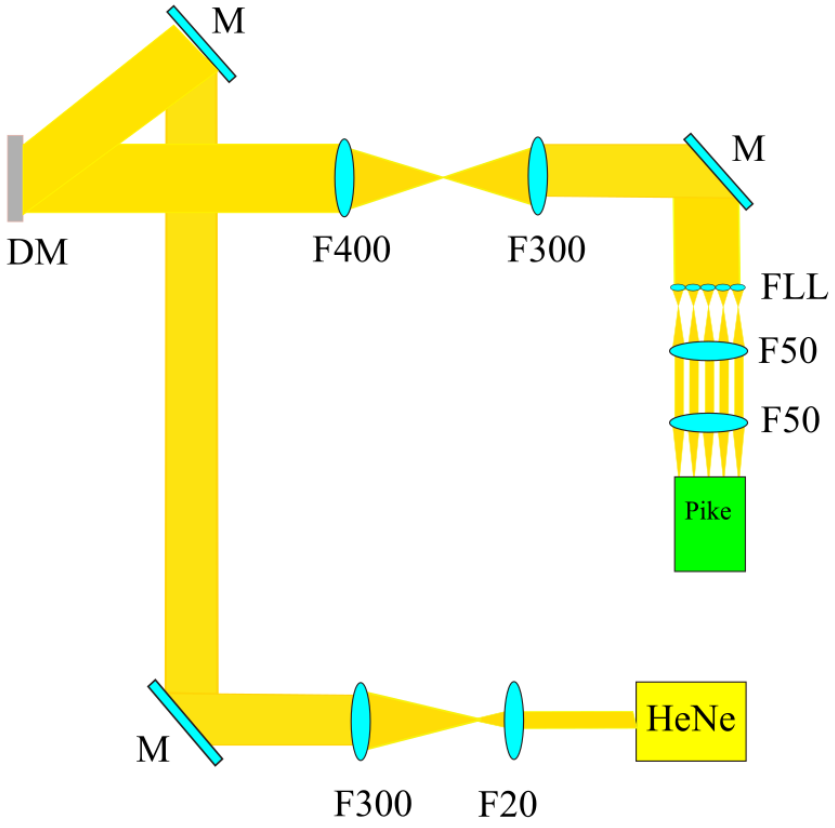

Figure 4.3: Design of Closed Loop Adaptive Optics implemented to test Shack-Hartmann wavefront sensing using cross correlation. Light from a helium neon laser is expanded by a 20mm and 300mm lens pair. Two bouncing mirrors (BM) relay the light to illuminate the Deformable Mirror (DM). The DM is relayed onto the lenslet array (FLL) using a 400mm and 300mm lens. A 1 to 1 matched pair focuses the light on the Pike CCD camera

Light Sheet Microscope Optical Design:

Figure 4.4 shows the optical design of the LSM. This design is based off the open source platform OpenSPIM [60]. Two beams from 488 and 561 lasers are combined using a dichroic for two-color imaging. A telescope consisting of a 25mm lens followed by a 50mm lens expands the beam before the light reflects off the scanning galvo mirror forming a light sheet in the Y-Z

plane of the illumination path. A telescope consisting of a 50mm lens followed by a 30mm lens demagnifies the scanned beam. The light is then focused by 10X water-dipping objective used for sample illumination. The light sheet passes through the biological specimen along the focal plane of the 20X objective that captures the sheet profile in the X-Y plane along the detection path. The detection objective has a magnification of 20x, NA equal to 0.5, and a working distance of 3.5 mm. A 180mm focal length tube lens forms the image on the CMOS camera. This design is modified in the Closed-Loop Light Sheet Optical Design section to include Scene Wavefront Sensing with AO by introducing additional elements between the tube lens and camera.

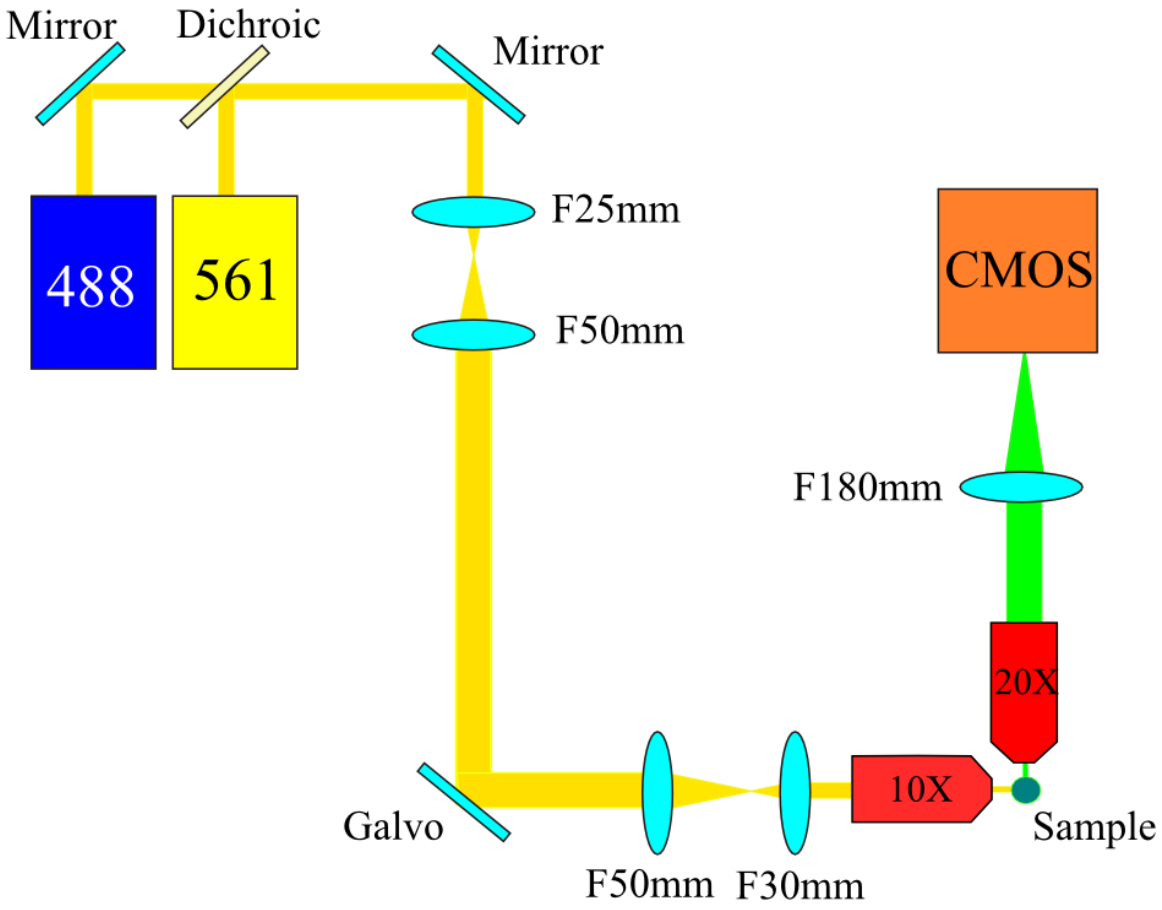

Figure 4.4: Illustrates the optical components in the Light Sheet Microscope Design.

The illumination axis is shown in Figure 4.5. The relationship between the initial beam waists h_1, h_2, h_3, h_4, and h_f that occur at different locations along the principle axis are shown. The lens configuration was chosen in such a way to maintain a narrow final beam waist over a large field of view to cover the entire region of the zebrafish brain. The Rayleigh range must e greater than ~200 μm. The beam diameter leaving the laser is 1.0 mm, therefore the beam height, h_1, is 0.5 mm. A 25 mm and 50 mm 4-f telescope expands the beam by a factor of 2 making h_2 and h_3 equal to 1.0 mm. Another telescope consisting of a 50 mm and 30 mm lens reduces the beam waist before the illumination objective, h_4 to 0.6 mm. Equation (4.1) defines the size of the pupil, D, if the entire objective were illuminated. Equation (4.2) defines the illuminated pupil, d. These diameters were calculated to be 10.8 mm and 1.2 mm. Equation (4.3) defines the relationship of the effective numerical aperture, NA_{eff}, in terms of the objectives numerical aperture, NA, and the variables, D and d. Equation (4.4) relates the beam waist before the illumination objective, h_4, to the final beam waist after the objective, h_f. The wavelength of the illumination light, λ , is 488 nm. The emersion medium, n, is water with an index of 1.33. The final beam waist is calculated to be 6.2 μm. The Rayleigh range of the light sheet is determined using equation (4.5). Twice the Rayleigh range is equal to 495 μm.

$$D = NA(2f) = 0.3(18)(2)\ \text{mm} = 10.8\ \text{mm} \quad (4.1)$$

$$d = 2h_4 = 1.2\ \text{mm} \quad (4.2)$$

$$NA_{eff} = \frac{NA(d)}{D} = \frac{0.3(1.2)}{10.8}\ \text{mm} = 0.033 \quad (4.3)$$

$$h_f = \frac{\lambda n}{\pi NA_{eff}} = \frac{1.33(0.488)}{0.033\pi} = 6.2\ \mu\text{m} \quad (4.4)$$

$$2 \times \text{Rayleigh Range} = \frac{2\pi h_f^{\,2}}{\lambda} = \frac{2\pi 6.2^2}{0.488} = 495\ \mu\text{m} \quad (4.5)$$

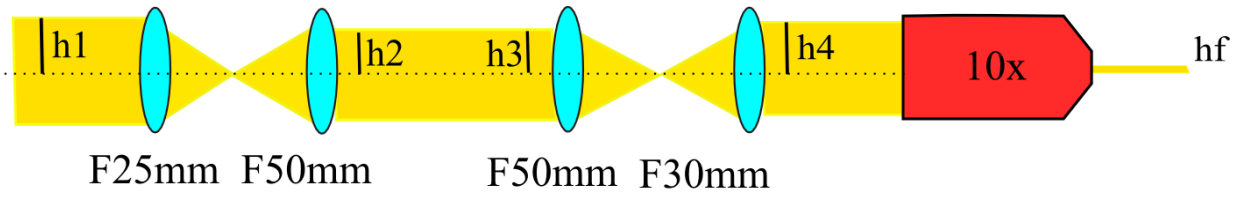

Figure 4.5: Illustration of the illumination axis within the Light Sheet Microscope.

Light Sheet Microscope Mechanical Design:

This section discusses the mechanical design of the Light Sheet Microscope based on the optical design discussed in the previous section. Figure 4.6 shows the mechanical design of the LSM designed in Autodesk inventor inspired by the OpenSPIM mechanical design. The microscope is placed on an optical table (TMC CleanTop Ametek). An OBIS 488 and OBIS 561 (Coherent) are used for sample illumination. Both lasers are mounted on machined aluminum laser mounts to raise the beam height to 50 mm above the optical table. The two beams are combined using two half-inch silver mirrors (Thorlabs BB05-E03) and a half-inch longpass dichroic mirror (Thorlabs DMLP505T). These mirrors are held in half-inch mirror mounts (Thorlabs Polaris – K05) inserted into machined aluminum posts to raise the center of the mirror to the 50 mm beam height when placed on a sliding rail carrier (Thorlabs RC1) on top of a dovetail optical rail (Thorlabs RLA1200). The first relay telescope after the bouncing mirror consists of half-inch lenses (AC127-025-A-ML and AC127-050-A-ML) mounted in half-inch lens mounts (Thorlabs LMR05). The center of the two lenses are raised to the 50 mm beam height with machined posts. These two lenses are also mounted on rail carriers (Thorlabs RC1) on top of a 12 inch dovetail (Thorlabs RLA1200). A scanning galvo mirror (Thorlabs GVSM002) is raised by a machined aluminum mount designed to slide on a dovetail optical rail (Thorlabs RLA1200). The galvo mount is designed such that the y-axis mirror is at a 50 mm beam height. The telescope after the galvo mirror is placed on the same optical rail with each

lens on a rail carrier (Thorlabs RC1). Machined posts raise the half-inch lenses (AC127-050-A-ML and AC127-030-A-ML) to a beam height of 60 mm due to a 10 mm raise in height after the scanning galvo. The lenses of the telescope are mounted in half-inch lens mounts (Thorlabs LMR05). Both microscope objectives (UMPLFLM 10XW and UMPLFLM 20XW) are mounted in a machined aluminum sample chamber holder and acrylic sample chamber with aluminum mounting objective rings. The sample chamber holder is designed in such a way to be mounted directly onto an optical dovetail such that the microscope objectives are at the 60 mm beam height. A 4axis motor (x, y, z, and rotation, USB-4D-Stage, Picard Industries) holds the sample. The stage is mounted on a 10mm high mount to account for the 10mm height change due to the galvo. The tube lens (Olympus U-TLU) is mounted in a machined aluminum mount that directly mounts on a dovetail to raise the tube lens to the 60 mm beam height. The CMOS camera (Hamamatsu ORCA-Flash 4.0) is raised to the 60 mm beam height on a machined camera mount. Figure 4.7 shows a table of all machined parts for the LSM.

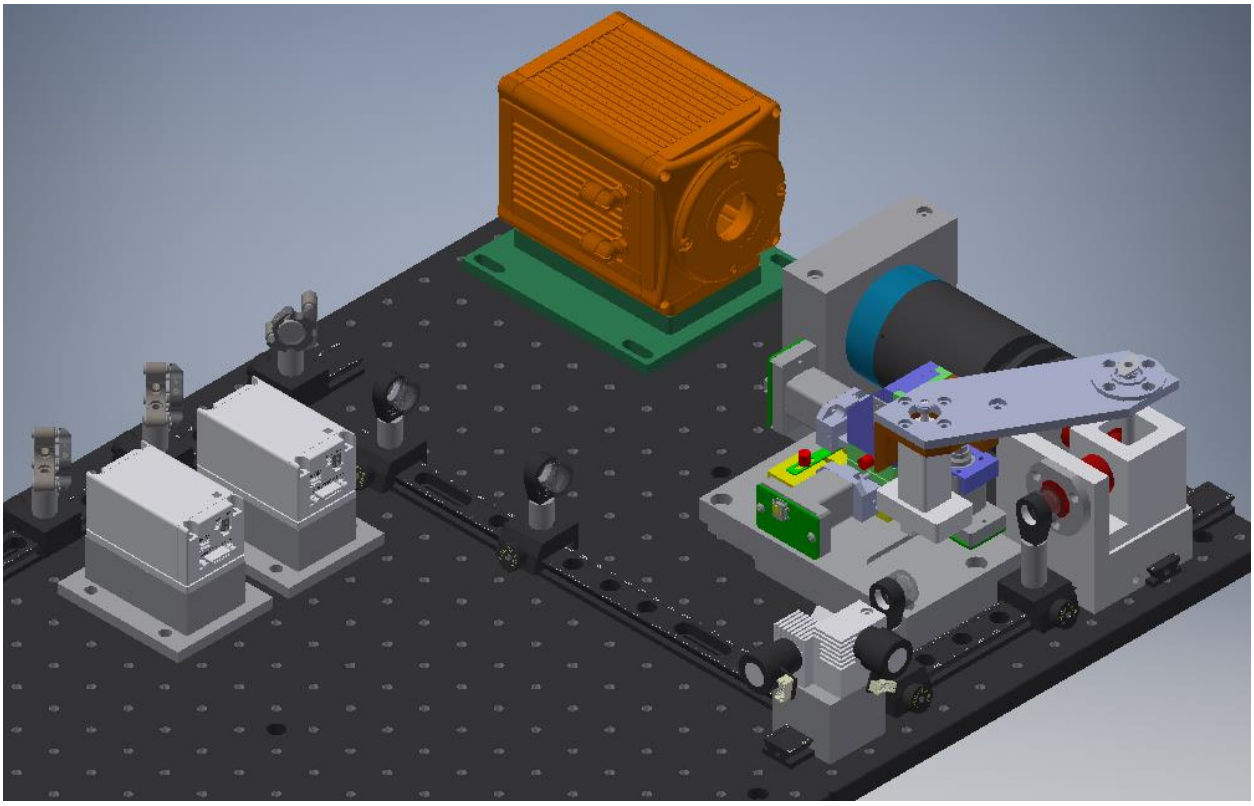

Figure 4.6: Illustrates the mechanical design for our experimental set up of the Light Sheet Microscope. This design is based off the OpenSPIM design created in AutoDesk Inventor 2016.

Name	Material	Quantity	Description
Sample Chamber	Acrylic	1	Water filled chamber used to hold the sample
Sample Chamber holder	Aluminum	1	Mounts the sample chamber and objectives
Objective Mounting Rings	Aluminum	2	Thread rings to mount the objectives to the sample chamber holder
Tube Lens Mount	Aluminum	1	Mounts the tube lens in place on an optical rail at a 60 mm beam height
50 mm LMR05 lens post	Aluminum	2	Posts for raising half-inch lenses to a 50 mm beam height
USB-4d-Stage mount	Aluminum	1	Mounts the stage onto the optical table and raises the motor 10 mm
60 mm LMR05 lens post	Aluminum	2	Posts for raising half-inch lenses to a 60 mm beam height
50 mm K-05 mirror post	Aluminum	2	Posts for raising half-inch mirors to a 60 mm beam height
50 mm laser mount	Aluminum	2	Mount to raise the laser to provide a 50 mm beam height above the optical table
Orca Flash Mount	Aluminum	1	Mount to raise the camera to a 60 mm beam height above the optical table
Galvo Mount	Aluminum	1	Mount the scanning galvo mirror on an optical rail at a 50 mm beam height with the x axis mirror.

Figure 4.7: Table showing the name of all machined parts for the LSM the material each part made, quantity of each part made, and description for each part.

Closed-Loop Light Sheet Optical Design

The LSM design had to be modified in order to incorporate a back pupil plane wavefront correction with a DM. The back pupil plane of the detection objective must be reimaged onto the deformable mirror with the deformable mirror reimaged onto the lenslet array to form a scene array on the sensor camera. Figure (4.8) shows the principle optical configuration with unknown focal lengths. The pupil size at the back pupil plane is determined by equation (4.6).

$$\emptyset_{BPP} = 2(f_{obj})(NA) \qquad (4.6)$$

$$\emptyset_{DM} = \frac{f_2}{f_{tl}}(\emptyset_{BPP}) \qquad (4.7)$$

The numerical aperture (NA) of the detection objective is equal to 0.5, and the objective has a focal length (Fobj) of 9mm. Therefore the pupil size at the microscope objective is calculated to be 9mm. We use the tubes lens and another achromatic doublet no relay the objective pupil onto the DM for wavefront correction. We want the objective's pupil to be demagnified such that the pupil size at the DM is equal to the DM's physical diameter of 5.0mm. The focal length of the achromatic doublet is determined to be 100mm from equation (4.7). We want to illuminate 22 x 22 lenslets with the 4.4mm x 4.4mm active DM area. $\emptyset_{LL}$is determined to be 6.6mm through equation (4.8).

$$\#\text{ of lenslets} = \frac{\emptyset_{LL}}{\text{Pitch}} \qquad (4.8)$$

Next we want to determine the ratio of f_4 /f_3 as shown in equation (4.9) to properly magnify the beam after the deformable mirror. A ratio of three-halves will satisfy the proper magnification. Therefore, f_3 is chosen to be 200 mm and f_4 to be a 300 mm focal length lens.

$$\emptyset_{LL} = \frac{f_4}{f_3}(\emptyset_{DM}) \qquad (4.9)$$

The lens that forms the image on the ORCA-FLASH has to satisfy the sampling condition of the detector given by equation (4.10).

$$\frac{\lambda}{4 \cdot NA} \cdot M_{obj} \cdot \frac{f_5}{f_2} = d_{pixel} \qquad (4.10)$$

λ is the wavelength of the detected light. M_{obj} is the magnification of the detection objective. d_{pixel} is the pixel size of the CMOS camera. f_5 is determined to be 200 mm.

The magnification due to this 4f lens pair reduces the active actuator pupil to a diameter of 3.6 mm. There are two reasons for choosing this magnification. One is that a pupil of 3.6 mm

illuminates 22 lenslets in the linear direction and maintains the Hudgin geometry discussed in Chapter 2. Second, the range of lenslets that can be illuminated is limited by the physical size of the HQ2 chip inside the camera. Each DM actuator is sampled by 2 lenslets. The actuators located at the corner of the deformable mirror are conjugate to the corner lenslets illuminated by the active actuator pupil. The lenslet array has a pitch of 300 μm. Each lenslet has a focal length of 4.7mm, a NA of 0.0319, and corresponds to 31 CCD pixels per lenslet with a field of view of 500 μm. The resolution of this SH system is given by $\frac{\lambda}{2 \cdot NA}$, which is equal to 7.83 μm. With all focal lengths determined, we can place the additional optics into a configuration that supplements into our LSM as shown in Figure (4.9).

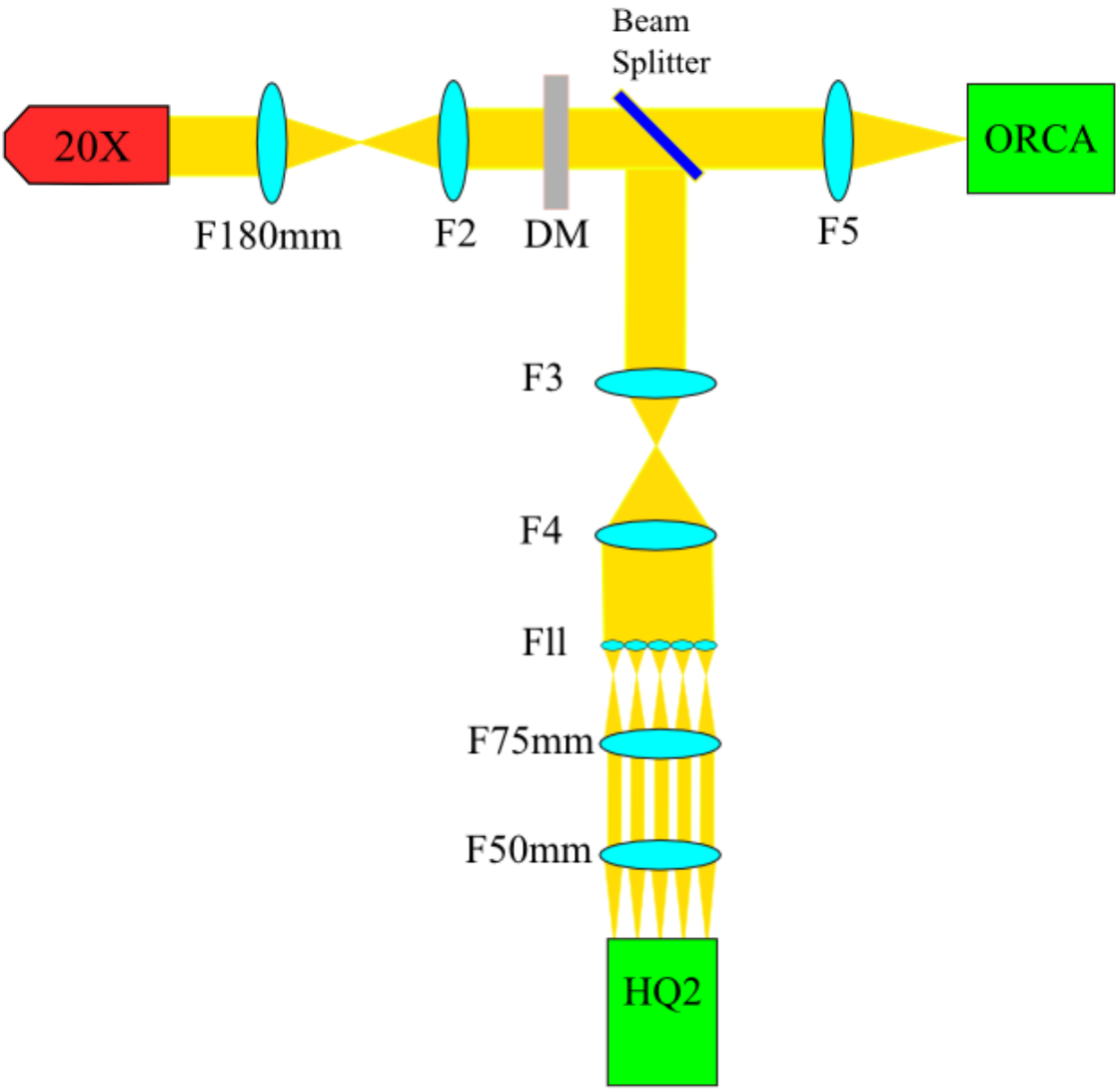

Figure (4.8): Illustrates the optical layout of elements needed to implement wavefront sensing and adaptive optics into the light sheet microscope. The back pupil plane of the detection microscope objective is reimaged onto the DM using the tube lens, F180 and F2 before being split in two directions by a beam splitter. F3 and F4 reimage the DM onto the lenslet array for wavefront sensing. The matched pair made of a 75mm and 50mm lens image the focal plane of the lenslet array onto the HQ2 camera generating an array of scenes. F5 forms an image of the ORCA flash.

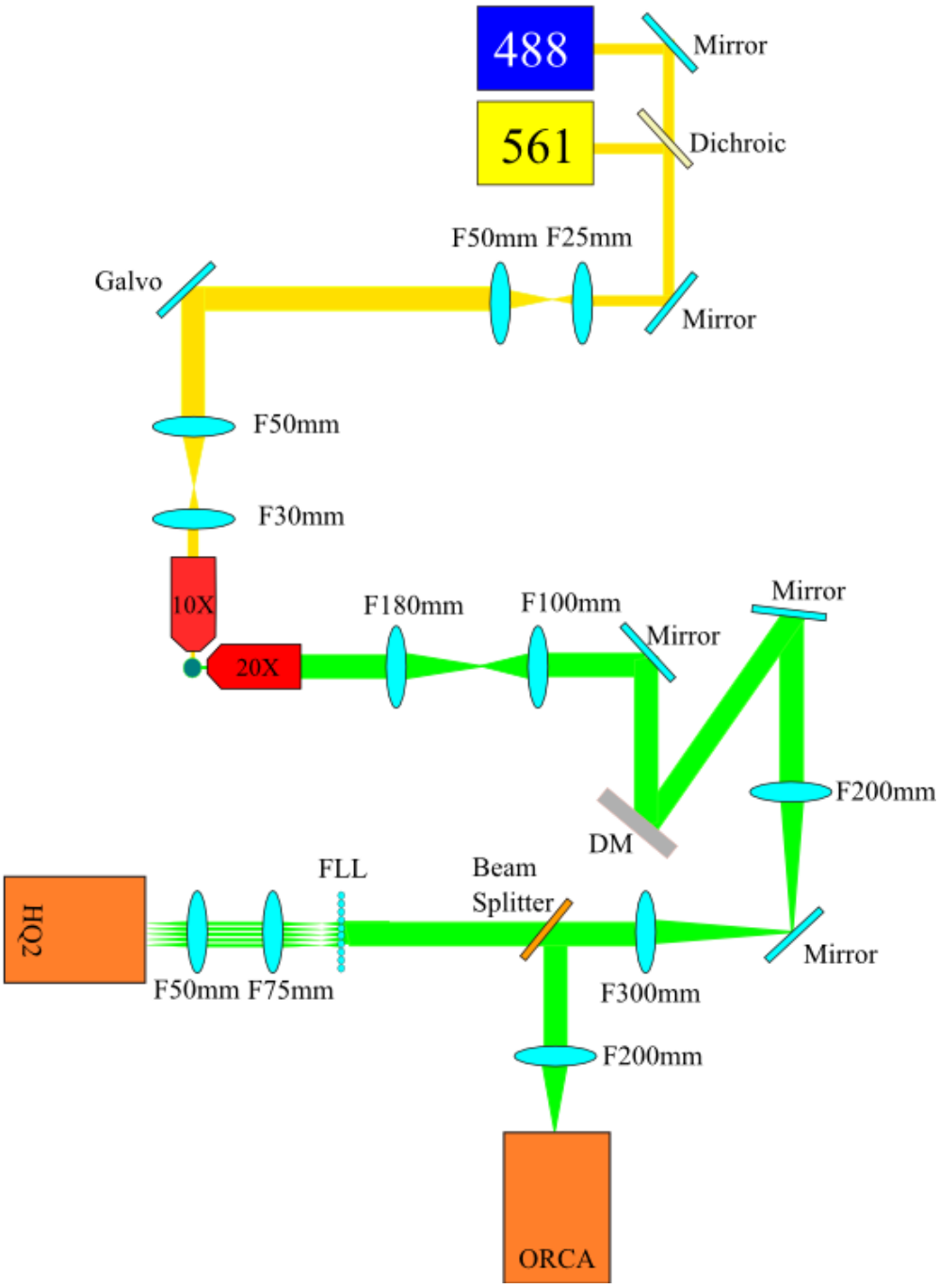

Figure 4.9: Illustration of the final optical design combining Adaptive Optics using a Shack-Hartmann wavefront sensor into the Light Sheet Microscope. This design takes into account the calculated focal lengths of the lenses and the fact that the DM must be placed in the optical system at an angle to reflect the light. Figure 4.8 illustrates the DM is a modulation element that light passes through.

Closed Loop Light Sheet Mechanical Design:

The purpose of this mechanical design is to physically implement AO into our LSM as discussed in the previous optical design section. Everything up through the tube lens of the original light sheet set up is the same for this one. Only the CMOS camera changes position. The camera is replaced with a 1-inch silver mirror (Thorlabs BB1-E02) mounted into a 1-inch mirror mount (Thorlabs Polaris-K1). All one inch mirror mounts are raised to the 60 mm beam height using machined mirror posts to mount directly on optical rails. A 1-inch 100mm focal length lens (Thorlabs AC254-100-A-ML) is mounted within a 1-inch lens holder (Thorlabs LMR1) to relay the back pupil plane of the 20X microscope objective onto the deformable mirror. Lens posts were machined in order to raise all 1-inch lens holders to a 60 mm beam height when mounted onto rail carriers placed on optical dovetails. The bouncing mirror, 100 mm lens, and deformable mirror are all placed on a 12 inch optical rail (Thorlabs RLA1200). The next configuration is also placed on a 12 inch optical rail. Light from the deformable mirror bounces off another 1-inch silver mirror mounted on an aluminum machined mount. The light is focused by a 200mm lens (OptoSigma SLSH-25-200P) in a lens mount (OptoSigma LHF-30AS) attached to a machined post to raise to 200 mm lens to the 60 mm beam height while placed on a rail carrier. A 2-inch silver mirror (ThorlabsBB2-E02) mounted in a 2-inch mirror mount (Thorlabs Polaris-K2) placed on an optical pedestal (Newport 9944-M) to redirect the beam perpendicularly to a 300 mm lens (OptoSigma SLSH-25-300P) placed in a 30 mm lens mount raised to a 60 mm beam height from a machined post. A 50/50 beam splitter (Thorlabs BSW10) mounted in a 1-inch mirror mount is placed on machined aluminum mount identical the 1-inch mirrors. A 2-inch diameter 200 mm lens (Thorlabs AC508-200-A-ML) and 300mm lens (Thorlabs AC508-300-A-ML) mounted in a 2-inch lens holder (Thorlabs LMR2). These two lenses are raised to the 60

mm beam height using an optical pedestal (Newport 9944-M). The Shack-Hartmann wavefront sensor applied in this setup consists of a lenslet array (Edmund Optics 86-745), a relay lens pair (Thorlabs MAP105075-A), and a photo-detector (Photometrics HQ2). Each lenslet has a focal length of 4.7 mm, a NA of 0.0108, and corresponds to 31 CCD pixels per lenslet. The rotation mount (Thorlabs RSP1x15/M) holding the lenslet array is raised to the 60 mm beam height with a machined mount. The 1-to-1.5 matched pair is mounted in a Thorlabs 1 inch lens post raised to 60 mm with a machined aluminum post. Both the ORCA Flash and HQ2 cameras are raised to the 60 mm beam height with machined camera mounts. Figure 4.10 shows all additional machined parts added to the light in order to implement this design. Figure 4.11 is a CAD rendering of the final mechanical design.

Name	Material	Quantity	Description
60mm LMR1 lens post	Aluminum	2	Raises Thorlabs 1-inch lens to a 60 mm beam height
60mm Optosigma	Aluminum	2	Raises Optosigma 1-inch lens to a 60 mm beam height
60mm 1 inch mirror posts	Aluminum	4	Raises thorlabs 1 inch mounts to a 60 mm beam height
Lenslet Array Mount	Aluminum	1	Raises the Thorlabs rotation mount to a 60 mm beam height
HQ2 Camera Mount	Aluminum	1	Raises the HQ2 photometrics camera to a 60 beam height

Figure 4.10: Table showing the name of all additional machined parts for implementing Adaptive Optics into the light sheet microscope. The table shows the material each part made, quantity of each part made, and description for each part.

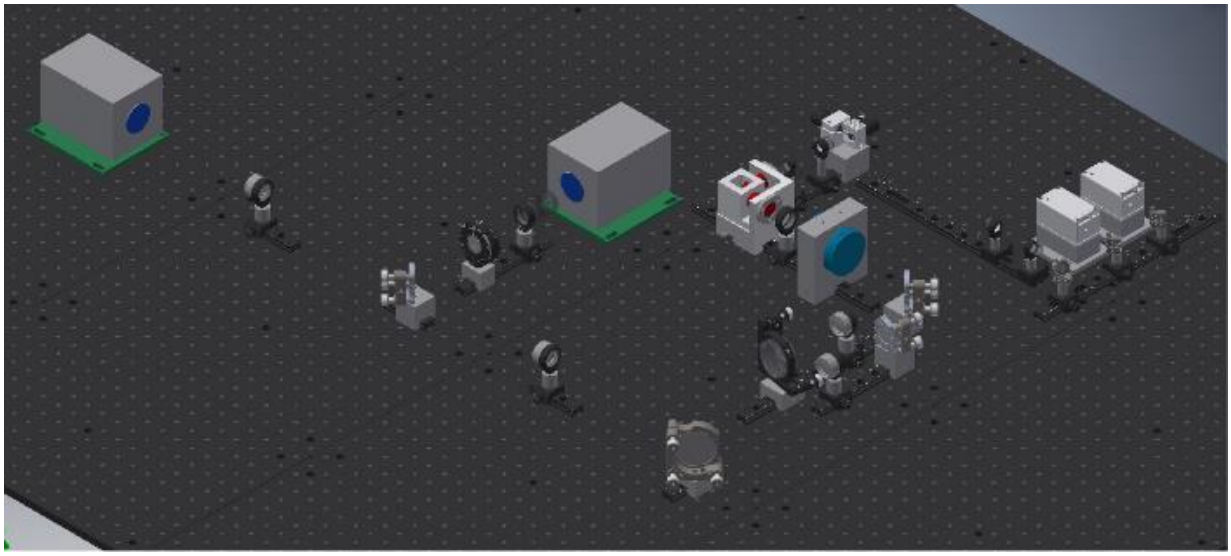

Figure (4.11): Mechanical Design for the Closed-Loop Light Sheet Microscope.

References

60) Pitrone P. G., Schindelin J., Stuyvenberg L., Preibisch S., Weber M.; Eliceiri K. W., Huisken J., Tomancak P. (2013) **OpenSPIM: an open access light sheet microscopy platform**

CHAPTER 5:

RESULTS

This chapter is a discussion of results obtained using the experimental setups discussed in Chapter 4. We will begin with the Closed Loop Evaluation set up, followed by the Light Sheet Microscope, and end with results using the Closed Loop Light Sheet microscope. This section will demonstrate the effectiveness of imaging with a LSM and quality of the corrections achieved with AO.

Closed Loop Evaluation:

The results discussed in this section correspond to the experimental set up discussed in the chapter 4 in the Closed-Loop Evaluation Set-Up section. This setup was designed to test the implementation of wavefront sensing applying cross-correlation in a closed loop AO environment. We built an influence function for commanding the DM as discussed in Chapter 2. by taking 141 Shack-Hartmann images. One image is the base-image where no actuators are pushed. This reference image will be compared to the remaining 140 to determine phase change due to each actuator element. This image is taken with all actuator values set to zero volts and is shown in Figure 5.1.

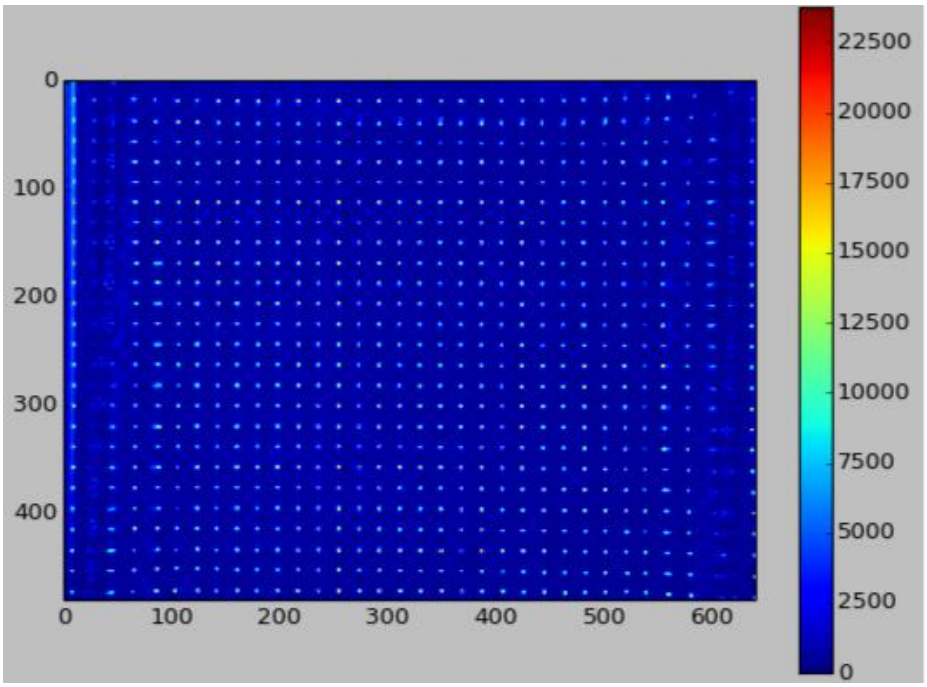

Figure (5.1): Image taken using a SHWFS with all actuators set to zero V. This base-image is used as the reference image that aberrated images are compared to determine the phase difference between them. The scale bar represents the intensity of at the given pixel.

The next 140 images each correspond to a deformable mirror local deformation with an actuator push of 0.2 V. The wavefront was calculated for each deformation by applying the wavefront sensing method discussed in chapter 3 using a base-image and offset-image to generate an array of 140 wavefronts, one for each poke. Figure 5.2 (a) shows a close up on a difference image between the base-image and an offset-image with a 0.2 V poke on 64^{th} actuator of the DM. The difference image illustrates the change in scene location generated by lenslets due to an optical path length increase of the light focused by lenslets local to the deformed area of the DM. The measured phase difference between the base-image and the offset-image sensed due to the deformation is shown in figure 5.2 (b).

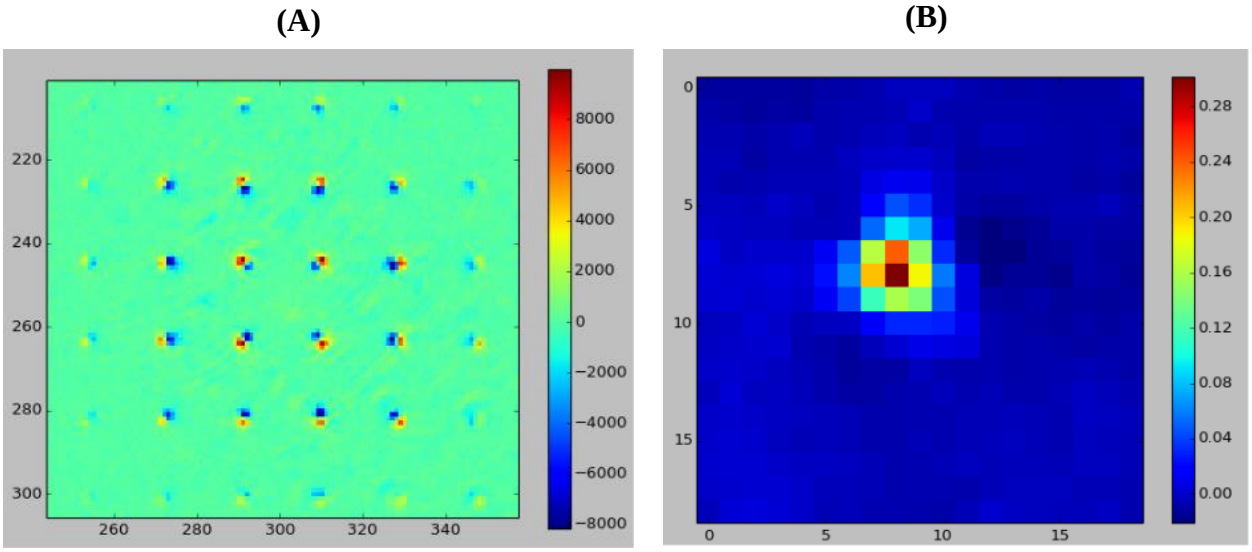

Figure (5.2): (A) is a difference image between a base-image and offset-image. The image has been magnified to see the difference in the deformation. The scale represents differences in intensity between the base image and the offset image. The offset image is taken with a 0.2 V poke on the 64th actuator. (B) shows the reconstructed wavefront phase in μm due to the change in the wavefront due to the poke.

An influence function and inverse influence function were generated as discussed in Chapter 2 using these 140 wavefront measurements. We shaped the deformable mirror to various forms corresponding to individual Zernike modes and sensed the phase difference of the resulting Shack-Hartmann scene array to a base-image with the mirror set flat. The actuator values to shape for a given wavefront is determined by matrix multiplying the wavefront with the inverse influence function. Figure 5.3 shows the phase difference between the base-image and an image taken with the mirror shaped to Zernike modes 2-13.

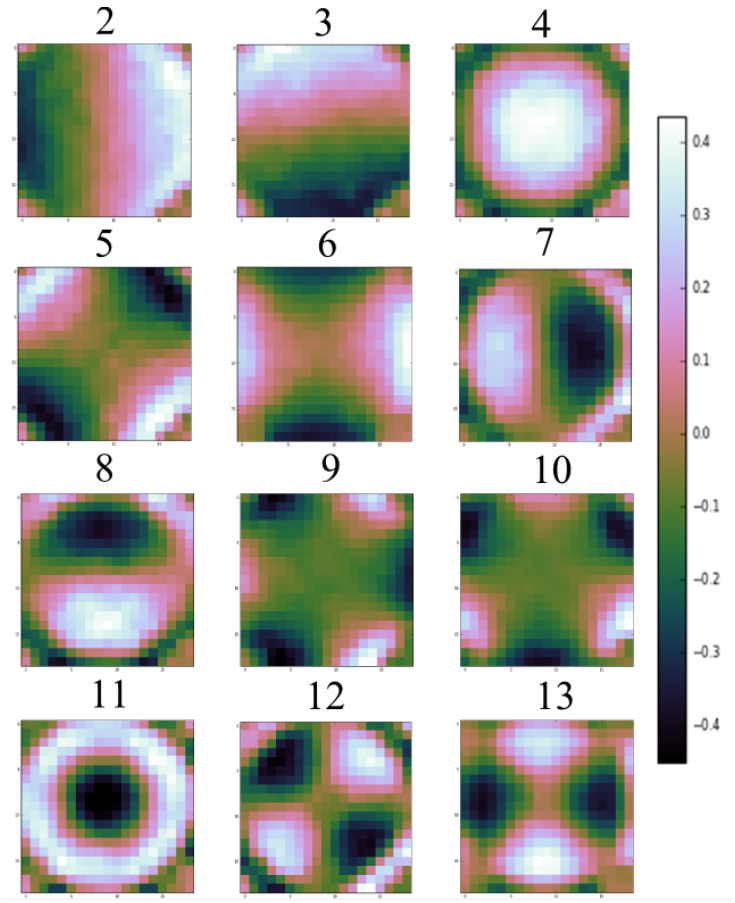

Figure (5.3): Wavefront reconstructions when setting the mirror to a shape for correcting individual Zernike modes. Modes 2-13 are shown. Units are in μm.

The final test for this evaluation setup was to perform an AO correction on an aberrated wavefront. Once again, a base image was taken with the mirror set flat before aberrations were induced by placing a 3000 mm focal length lens in front of the lenslet array. The wavefront phase difference caused by the aberration was calculated using the SHWFS. The aberrated wavefront was corrected by updating actuator values due to the sensed wavefront. Figure 5.4 (a) shows the aberrated optical wavefront due to the 3000 mm lens. Figure 5.5 (b) shows the measured wavefront after correction. The RMS error for the sensed wavefront was reduced from 0.0967 μm to 0.0171 μm after correction.

(A) **(B)**

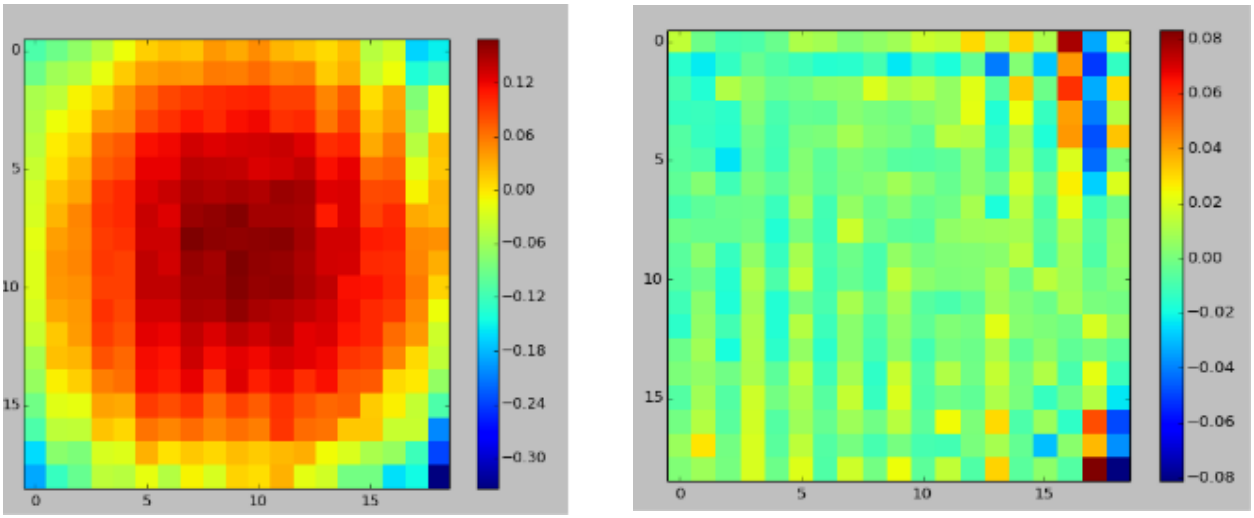

Figure (5.4): (a) shows an aberrated wavefront sensed by the SHWFS due to a 3000 mm focal length lens placed in the optical path in front of the lenslet array. (b) shows the corrected wavefront after performing an AO correction. Units are in μm

Light Sheet Microscope Results:

This section will reveal the results imaging applying the light Sheet microscope. Figure 5.5 (a) shows an image of the Gaussian beam captured by the ORCA Flash. Sweeping this beam creates our light sheet as seen in figure 5.5 (b)

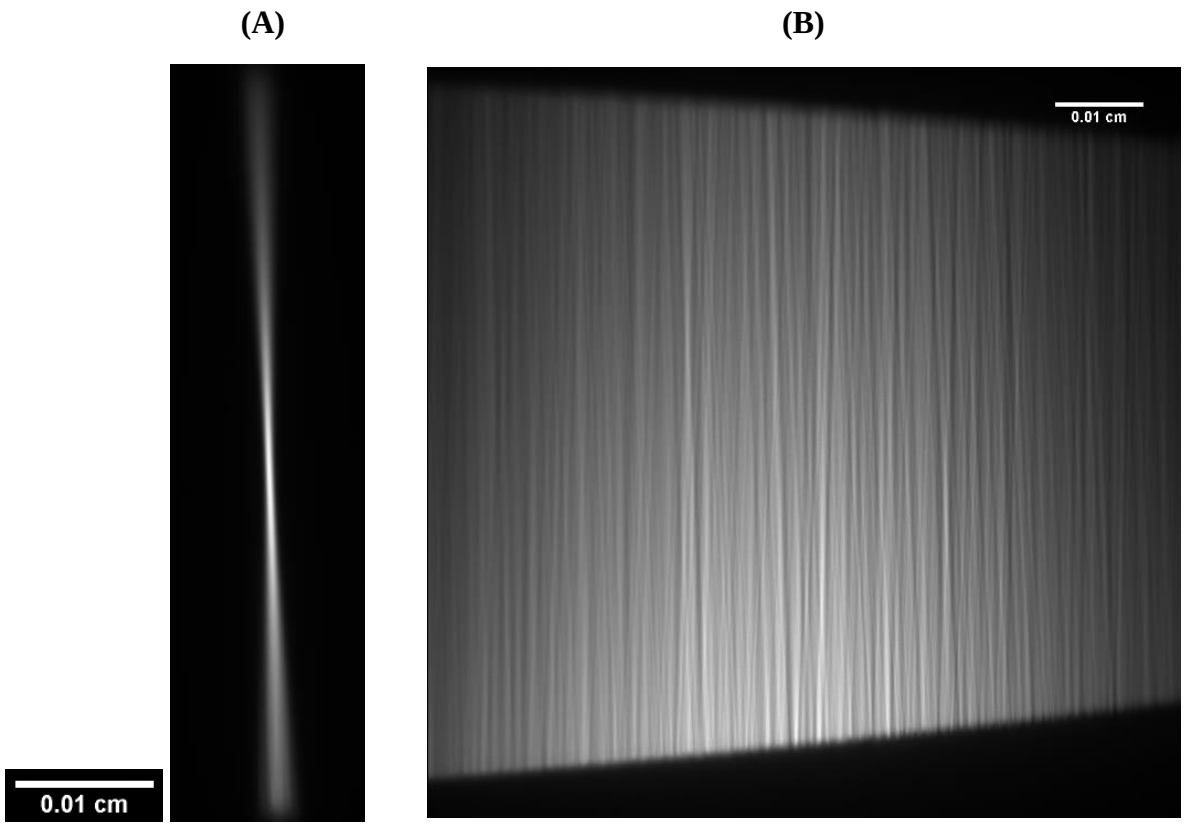

Figure (5.4): (a) Shows the beam profile of the LSM. (b) shows the generated Digital Scanned Light Sheet.

Figure 5.6 shows images of seizure dynamics within a zebrafish embryo. The sample is a GCaMP5G; *gad1b*:RFP+/- zebrafish imaged at 50Hz with a field of view of 330 microns. *Gamma*-Aminobutyric acid(GABA) is an inhibitory transmitter. Glutamate decarboxylase(GAD) is an enzyme catalyze to the decarboxylation of glutamate to GABA and CO2. GAD is encoded by gad1a, gad1b and gad2. The sample is genetically mutated such that part of the gad1b gene will result in an improperly functioning protein.

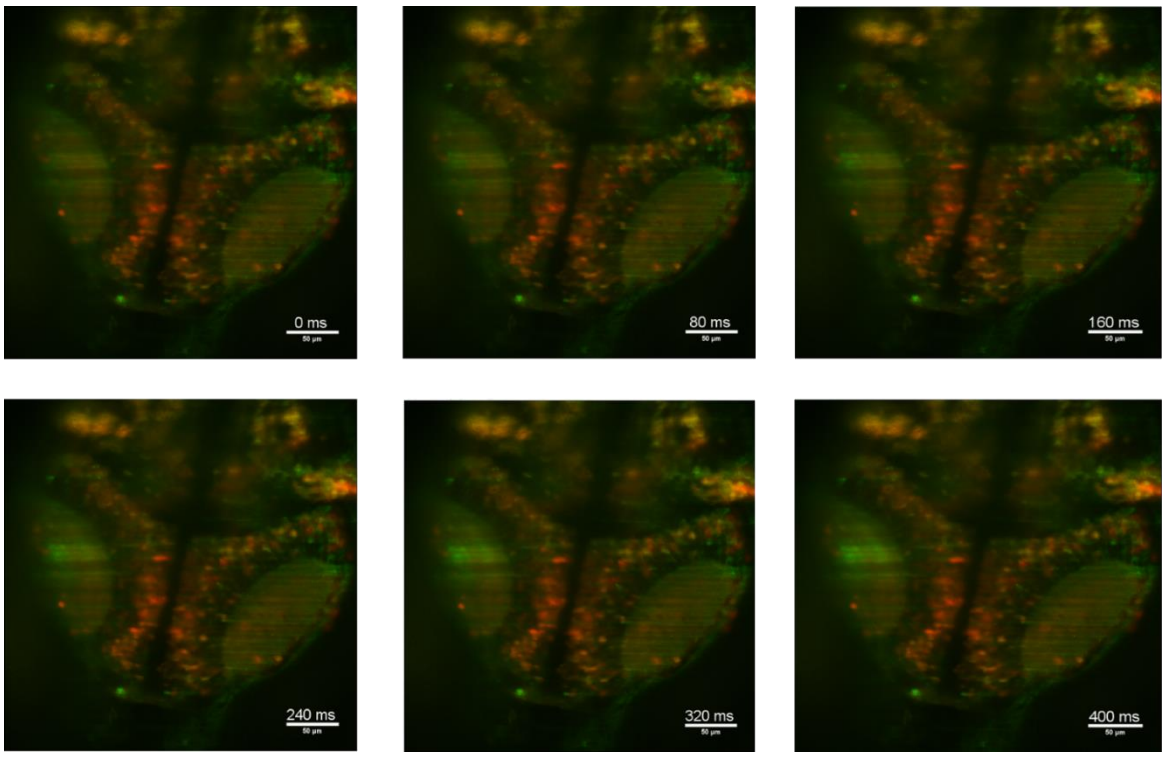

Figure (5.5): Images of calcium waves within a zebrafish embryo, 5dpf GCaMP5G;*gad1b*:RFP. zebrafish embryo treated with PTZ. The green channel labels GCaMP5g calcium indicator. The red channel is a red fluorescent protein labeling *gad1b.*

Light Sheet Microscope with Adaptive Optics:

This section shows the data once Scene-Based Adaptive Optics was added into the system. Once the mechanical system was assembled the first experiment was to build an influence function while looking at a zebrafish. Figure 5.6 (a) shows the Shack-Hartmann image with the DM voltages set flat. Figure 5.6 (b) shows a close up on an individual lenslet. This lenslet shows the left and right optical tectum of the imaged zebrafish. 141 images were taken to with a 0.25 V poke applied to the DM actuator when each was individually modulated. The two-image wavefront reconstruction method was used to generate to phase relationship due to each actuator deformation. Figure 5.7 (a) shows the wavefront change after the 100^{th} actuator is modulated. Figure 5.7 (b) is a plot of the maximum phase amplitude change causes by during

each modulation. The actuators with very low actuator values are due to the position of the actuators in relation to the pupil. These actuators are on the edge and slightly outside the pupil, so when these actuators “poke” there are no/fewer lenslet images conjugate to the actuator.

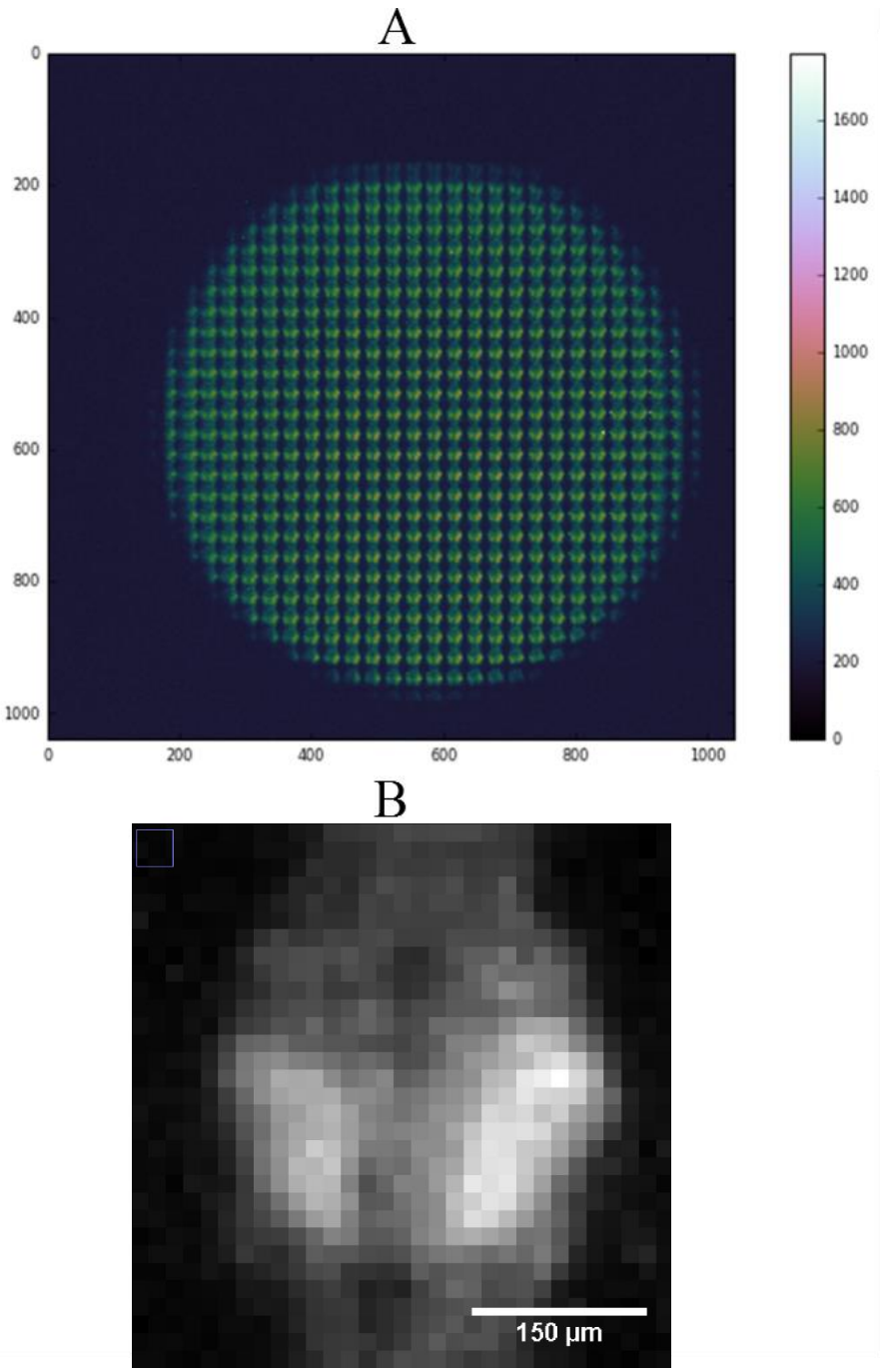

Figure 5.6: (a) is the Shack-Hartmann image of 6 day old wildtype zebrafish. Each lenslet forms its own image of the zebrafish’s brain on the HQ2. (b) shows a cut out of the central lenslet.

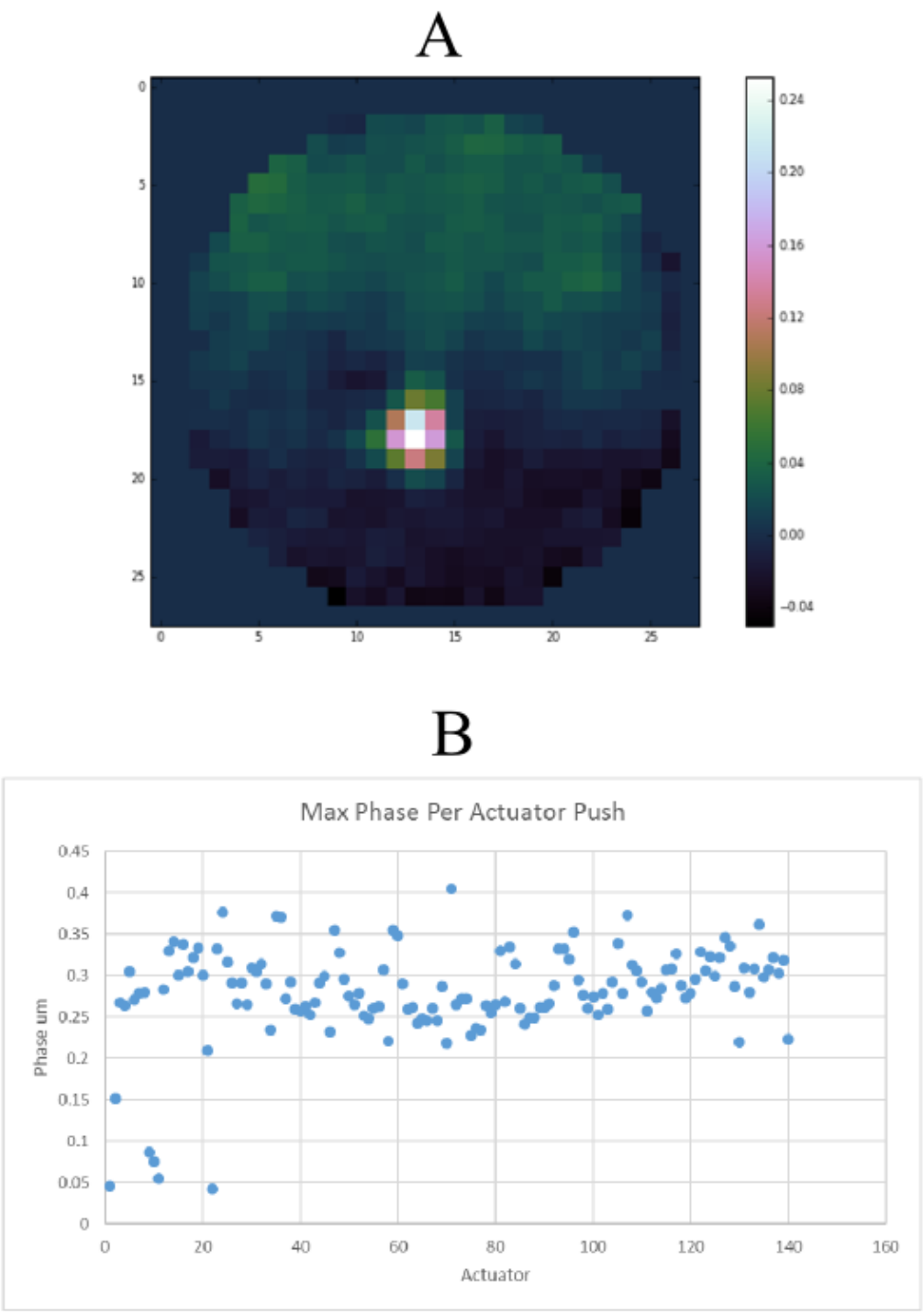

Figure 5.7: (a) shows the phase change in the wavefront introduced by a 0.2V poke on the 100th actuator of the DM. (b) shows a plot of the maximum phase amplitude change causes by during each modulation. Units are in microns

The inverse matrix for the AO system was determined through SVD after the influence function was generated. Zernike Modes 3 through 120 were generated on the DM and sensed using the two-image Scene-Based Shack-Hartmann method. Modes 3 through 20 shown in Figure 5.8 (a). The RMS values for each mode are plotted in (b).

(a)

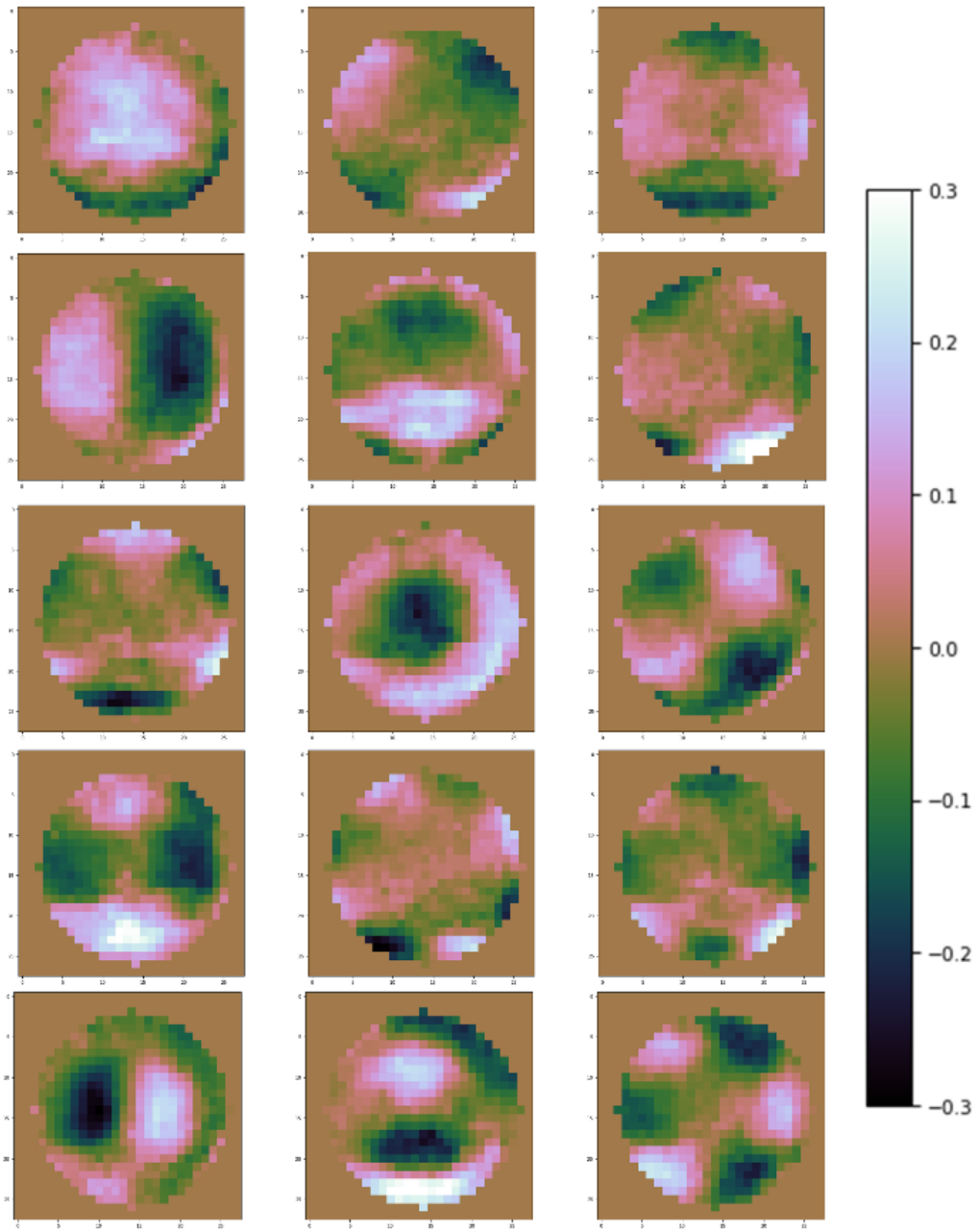

(b)

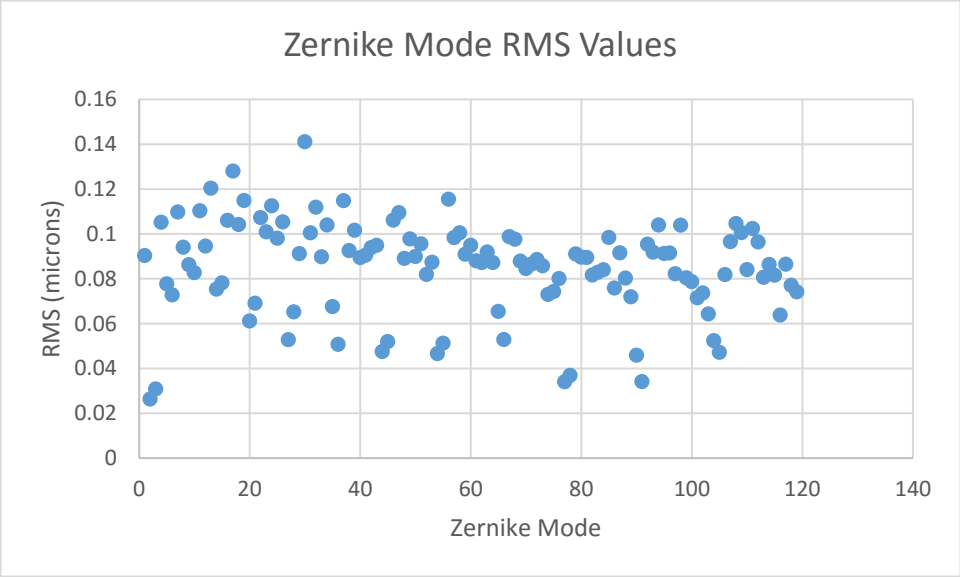

Figure 5.8: (a) shows the modes 3 through 20 sensed by the Wavefront Sensor in the Light Sheet applying cross-correlation. (b) is a plot of the RMS values for each sensed mode in μm.

The increased of spherical aberration corresponding to increase of imaging depth is sensed using the Scene-Based Shack-Hartmann. The one-image reconstruction method is applied in this situation because the scene is dynamic and changes as the sample is scanned. A base image is taken with the image plane at the edge of the zebrafish and its wavefront reconstructed. 3 μm steps were taken deeper into the sample, and each time an image was taken then its wavefront calculated. The difference between the initial wavefront at the start of the fish and each proceeding wavefront is calculated. The line profiles through the wavefront differences shown in Figure 5.9 (a). Wavefronts reconstructed at 3, 6, 9, and 12 μm depths are shown in Figure 5.9 (b).

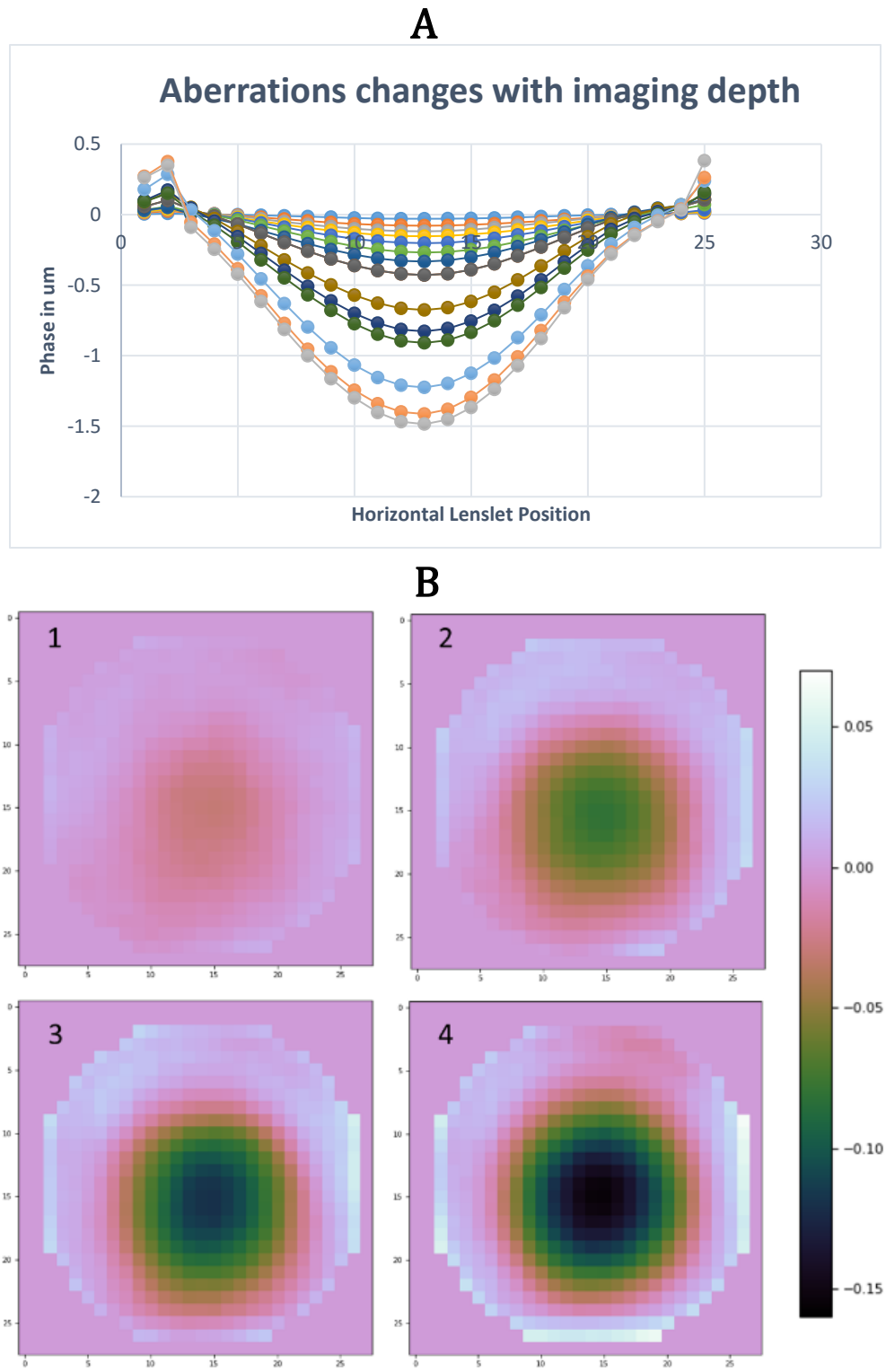

Figure 5.9: (a) shows the line profile across the calculated wavefront while scanning through the zebrafish. The amount of spherical aberration increases as imaging depth increases. Each step size through the fish is 3 µm. (b) shows the first 4 wavefront differences at steps 1,2,3 and 4. Phase units are in µm.

Conclusions and Future work:

We successfully demonstrated a technique for wavefront modulation and aberration correction in a light sheet microscope by applying adaptive optics. Direct measurement of the wavefront while looking at general scenes was accomplished by using cross-correlation to determine wavefront gradients. We demonstrate the effectiveness of cross-correlation by building an influence function, shaping the deformable mirror to multiple Zernike modes, and sensing spherical aberration within *D. rerio.*

Future work for this project is to perform an Adaptive Optics to correct for the wavefront aberrations caused from imaging deep into *D. rerio* and distrotions due to imperfections in the system.

APPENDIX

Machined Parts

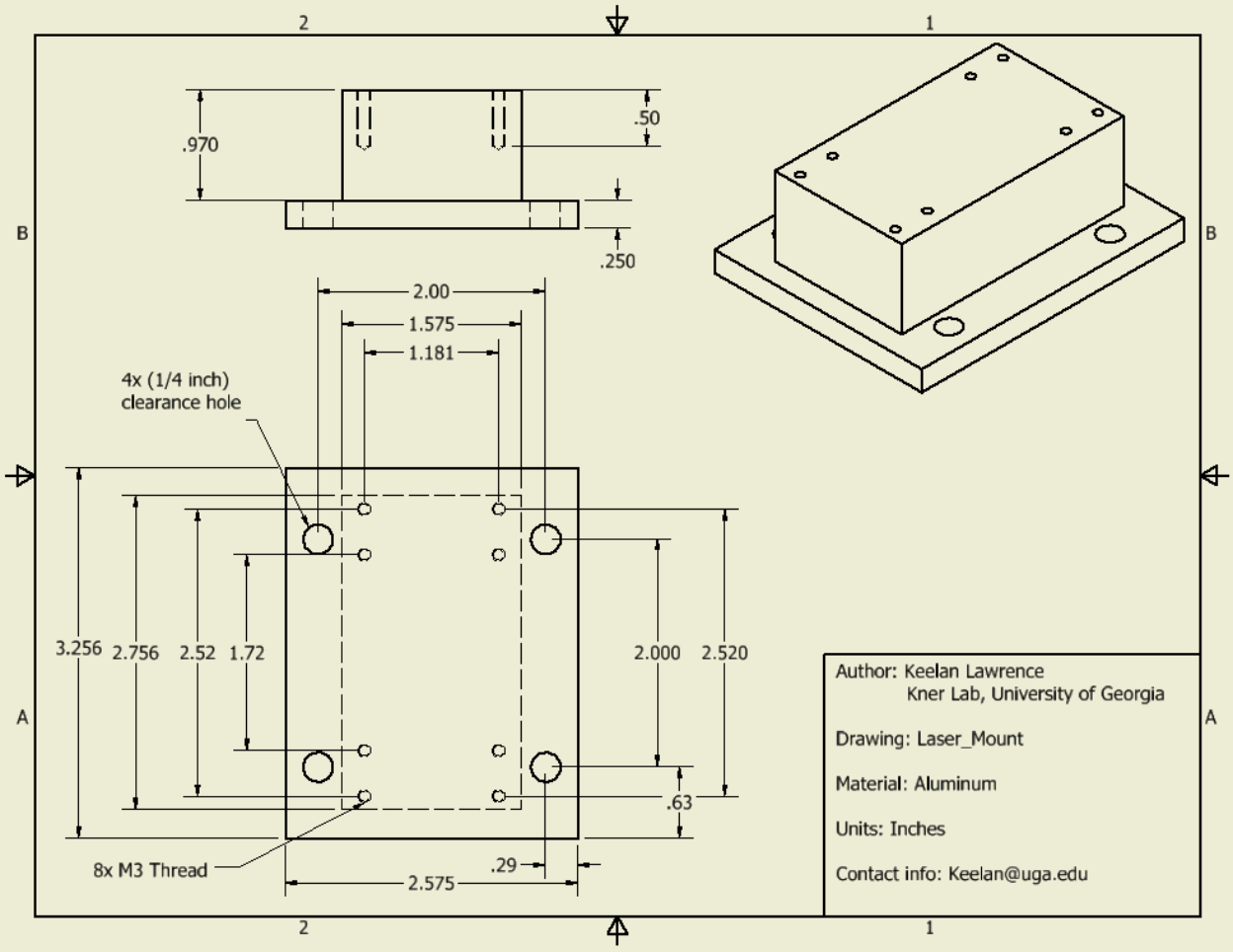

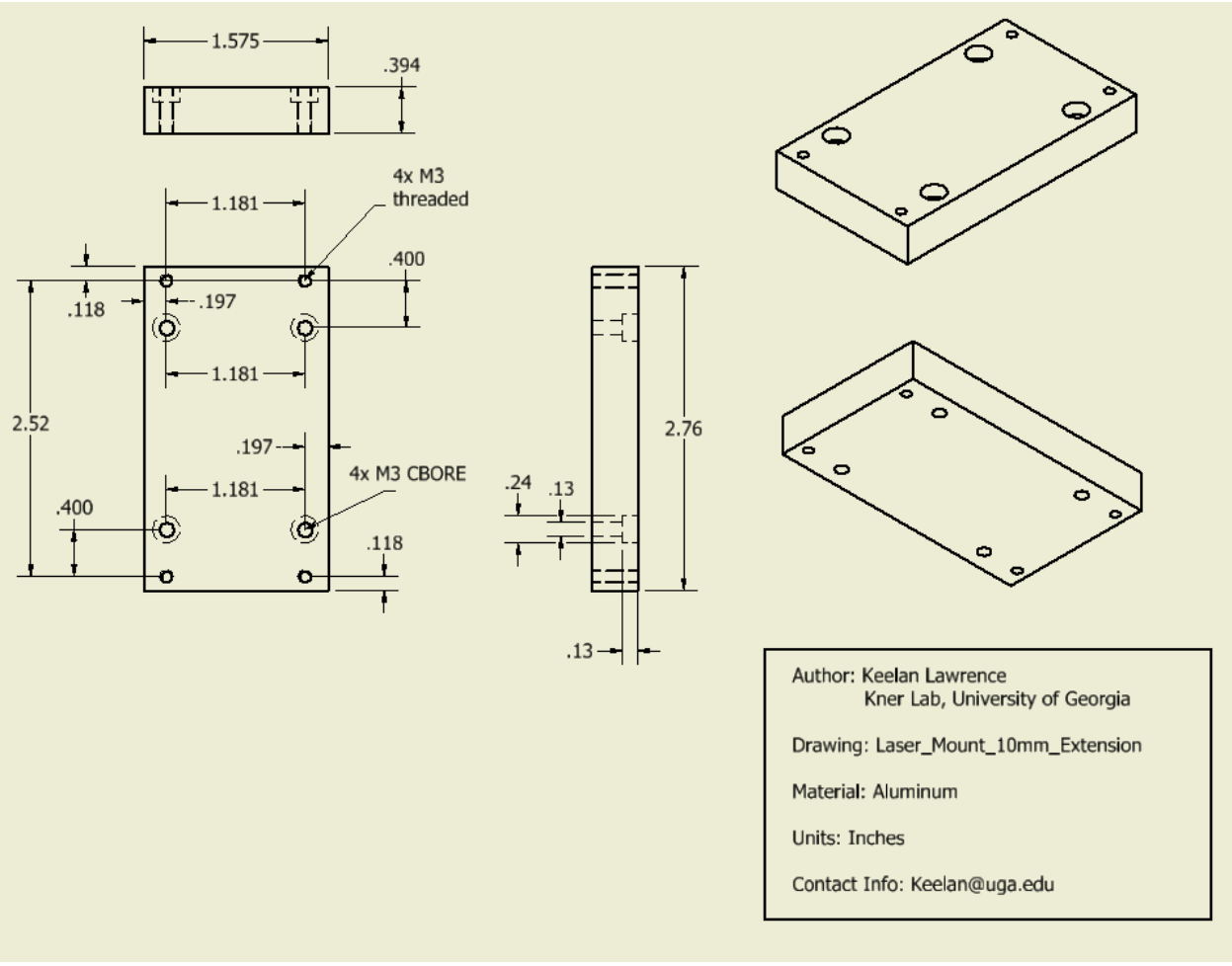
1.575
.394
4x M3
threaded
1.181
.400
.118
.197
1.181
2.52
.197
4x M3 CBORE
1.181
.400
.118
.24
.13
2.76
.13
Author: Keelan Lawrence
Kner Lab, University of Georgia
Drawing: Laser_Mount_10mm_Extension
Material: Aluminum
Units: Inches
Contact Info: Keelan@uga.edu

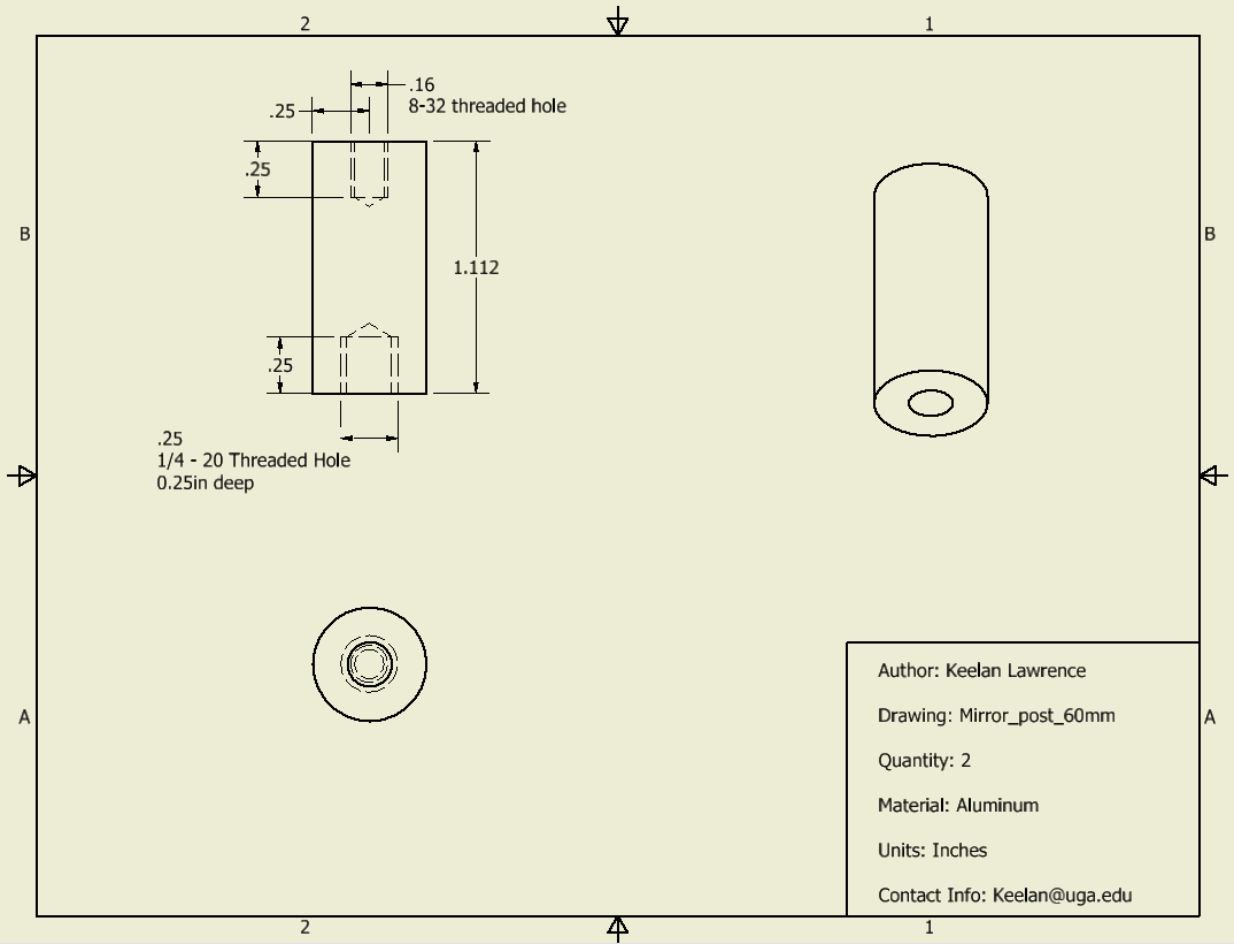
2
1
B
A
.16
8-32 threaded hole
.25
.25
1.112
.25
.25
1/4 - 20 Threaded Hole
0.25in deep
Author: Keelan Lawrence
Drawing: Mirror_post_60mm
Quantity: 2
Material: Aluminum
Units: Inches
Contact Info: Keelan@uga.edu

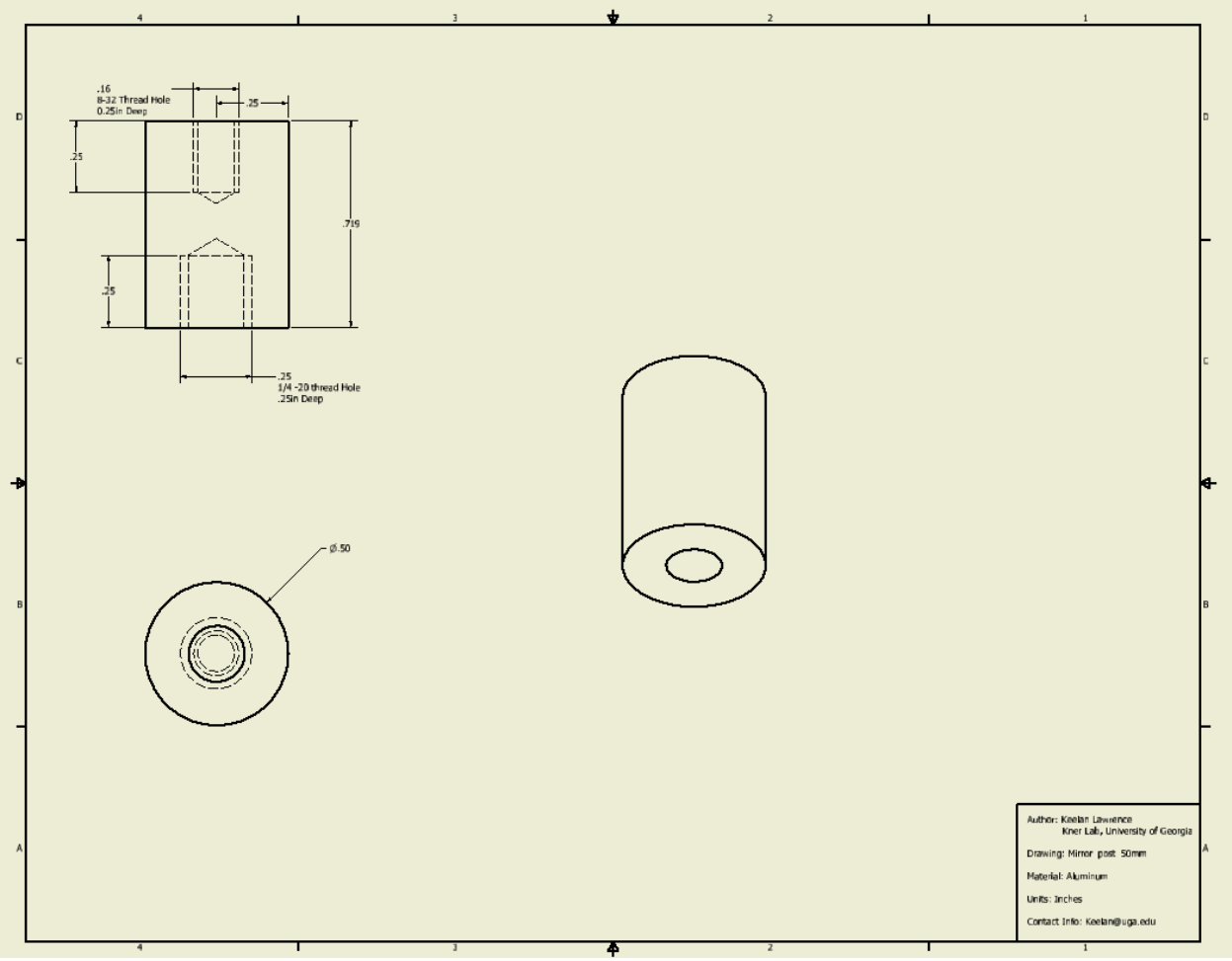
.16
8-32 Thread Hole
0.25in Deep
.25
.25
.719
.25
.25
1/4 -20 thread Hole
.25in Deep
Ø.50
Author: Keelan Lawrence
Kner Lab, University of Georgia
Drawing: Mirror post 50mm
Material: Aluminum
Units: Inches
Contact Info: Keelan@uga.edu

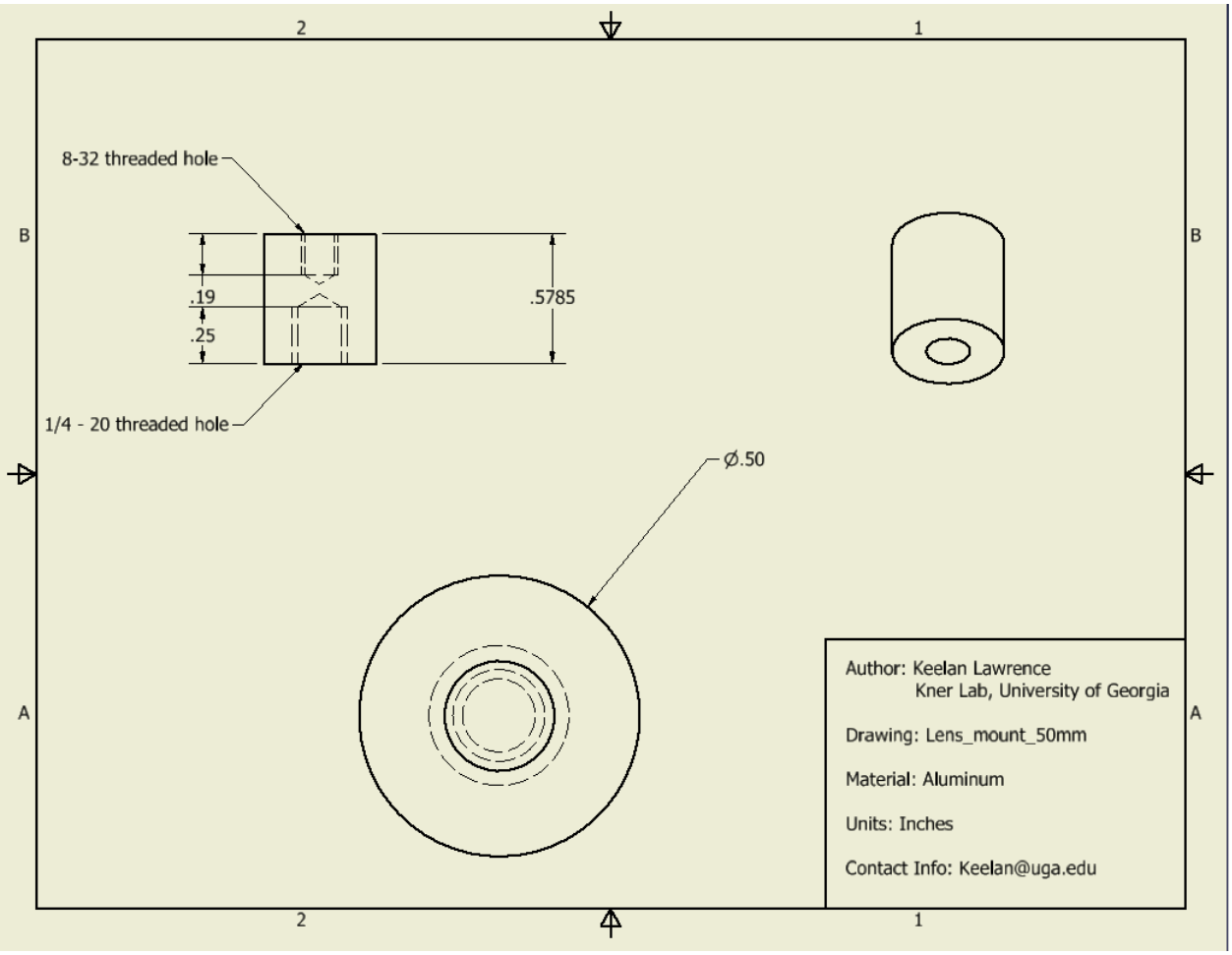
8-32 threaded hole
.19
.25
.5785
1/4 - 20 threaded hole
Ø.50
Author: Keelan Lawrence
Kner Lab, University of Georgia
Drawing: Lens_mount_50mm
Material: Aluminum
Units: Inches
Contact Info: Keelan@uga.edu

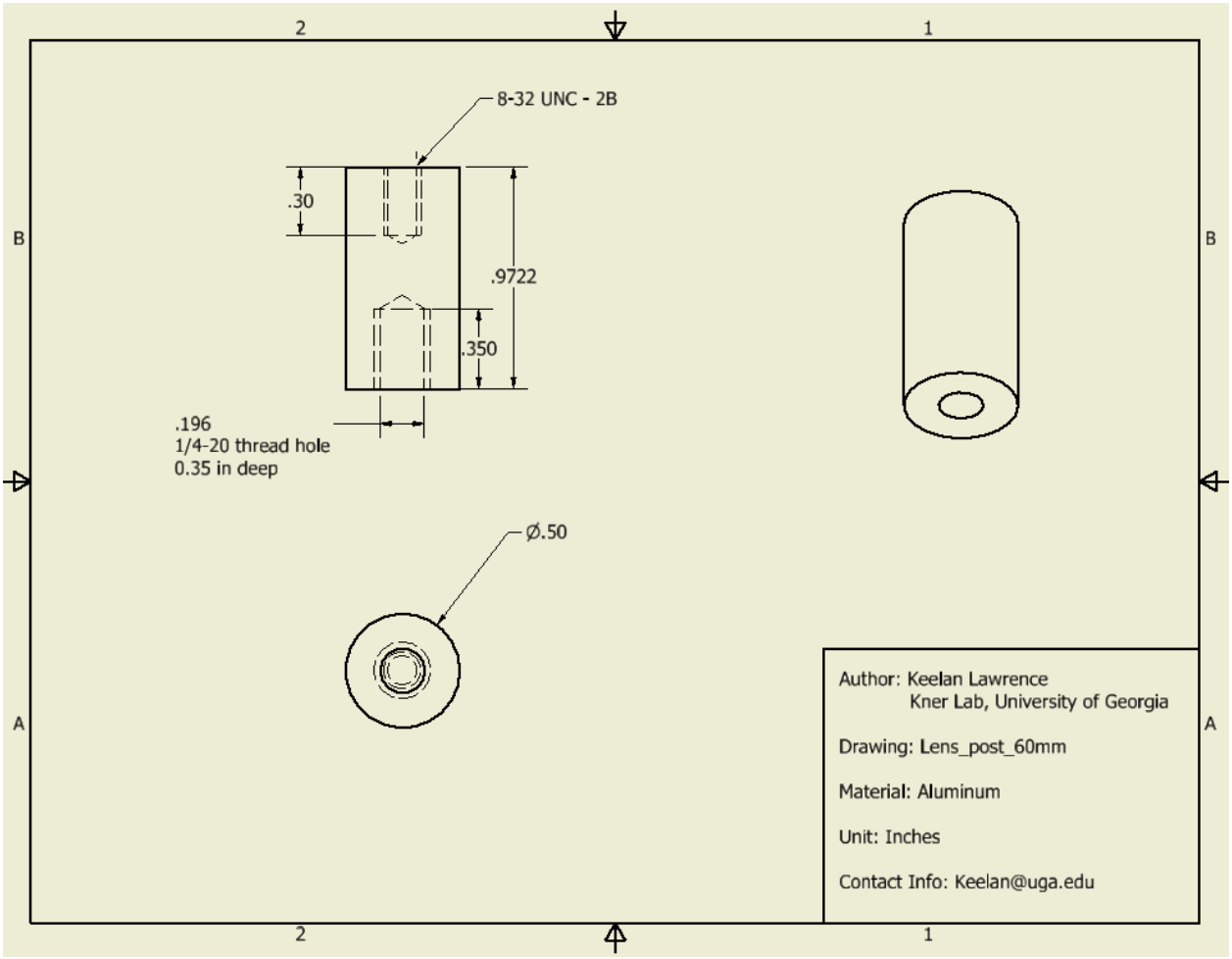
8-32 UNC - 2B
.30
.9722
.350
.196
1/4-20 thread hole
0.35 in deep
Ø.50
Author: Keelan Lawrence
Kner Lab, University of Georgia
Drawing: Lens_post_60mm
Material: Aluminum
Unit: Inches
Contact Info: Keelan@uga.edu

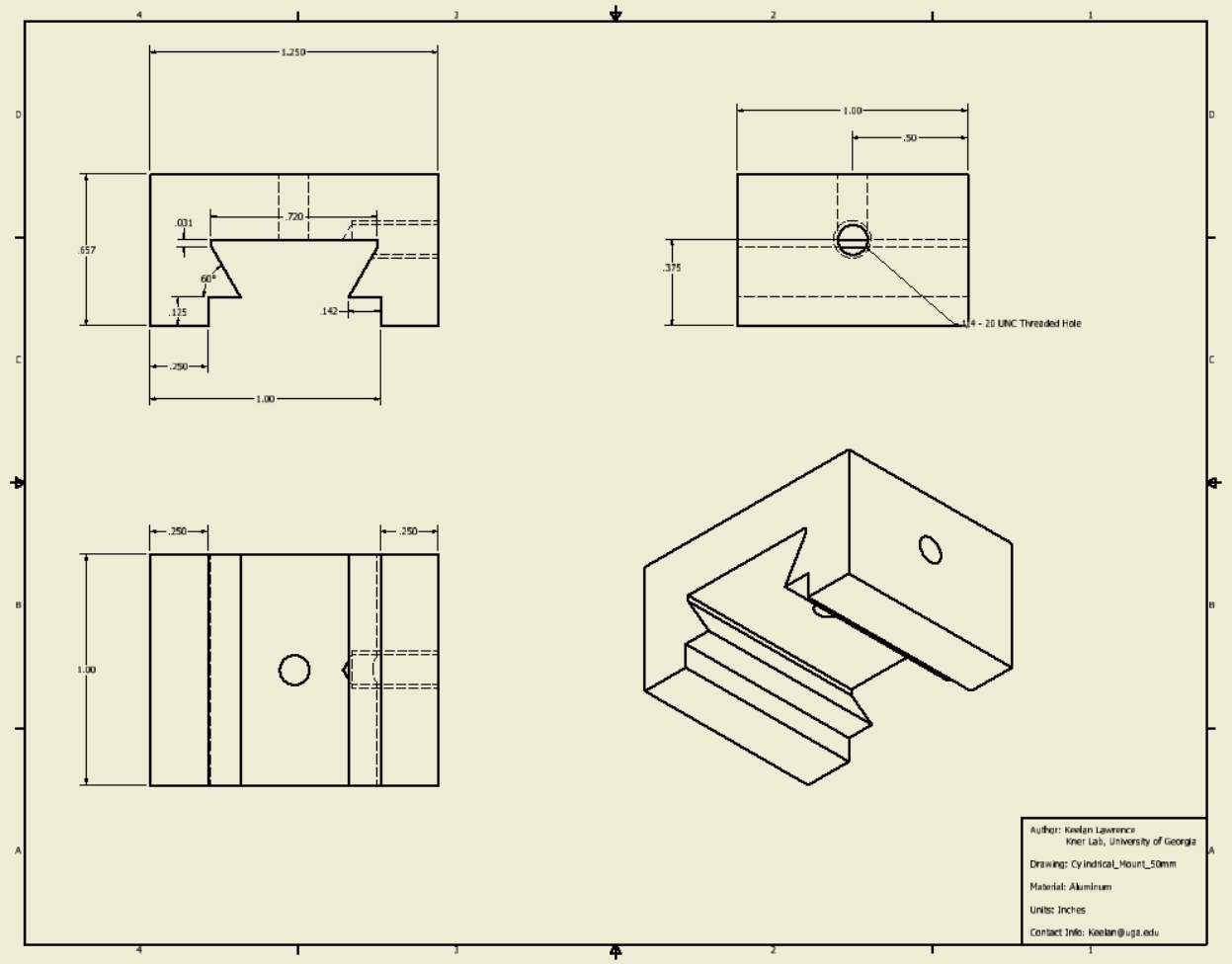
1.250
.657
.031
.720
60°
.125
.142
.250
1.00
1.00
.50
.375
1/4 - 20 UNC Threaded Hole
.250
.250
1.00
Author: Keelan Lawrence
Kner Lab, University of Georgia
Drawing: Cylindrical_Mount_50mm
Material: Aluminum
Units: Inches
Contact Info: Keelan@uga.edu

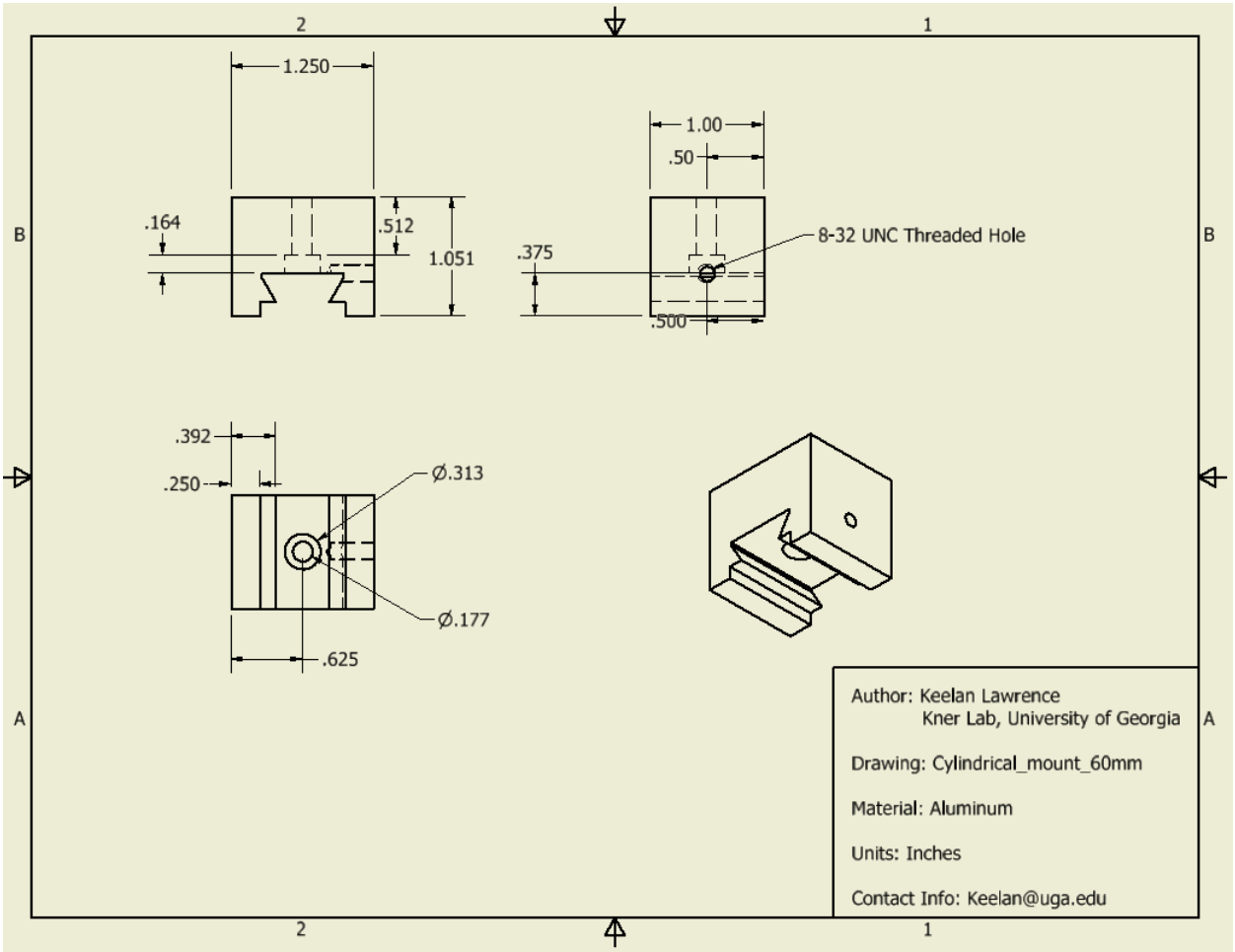
1.250
1.00
.50
.164
.512
1.051
.375
8-32 UNC Threaded Hole
.500
.392
.250
Ø.313
Ø.177
.625
Author: Keelan Lawrence
Kner Lab, University of Georgia
Drawing: Cylindrical_mount_60mm
Material: Aluminum
Units: Inches
Contact Info: Keelan@uga.edu

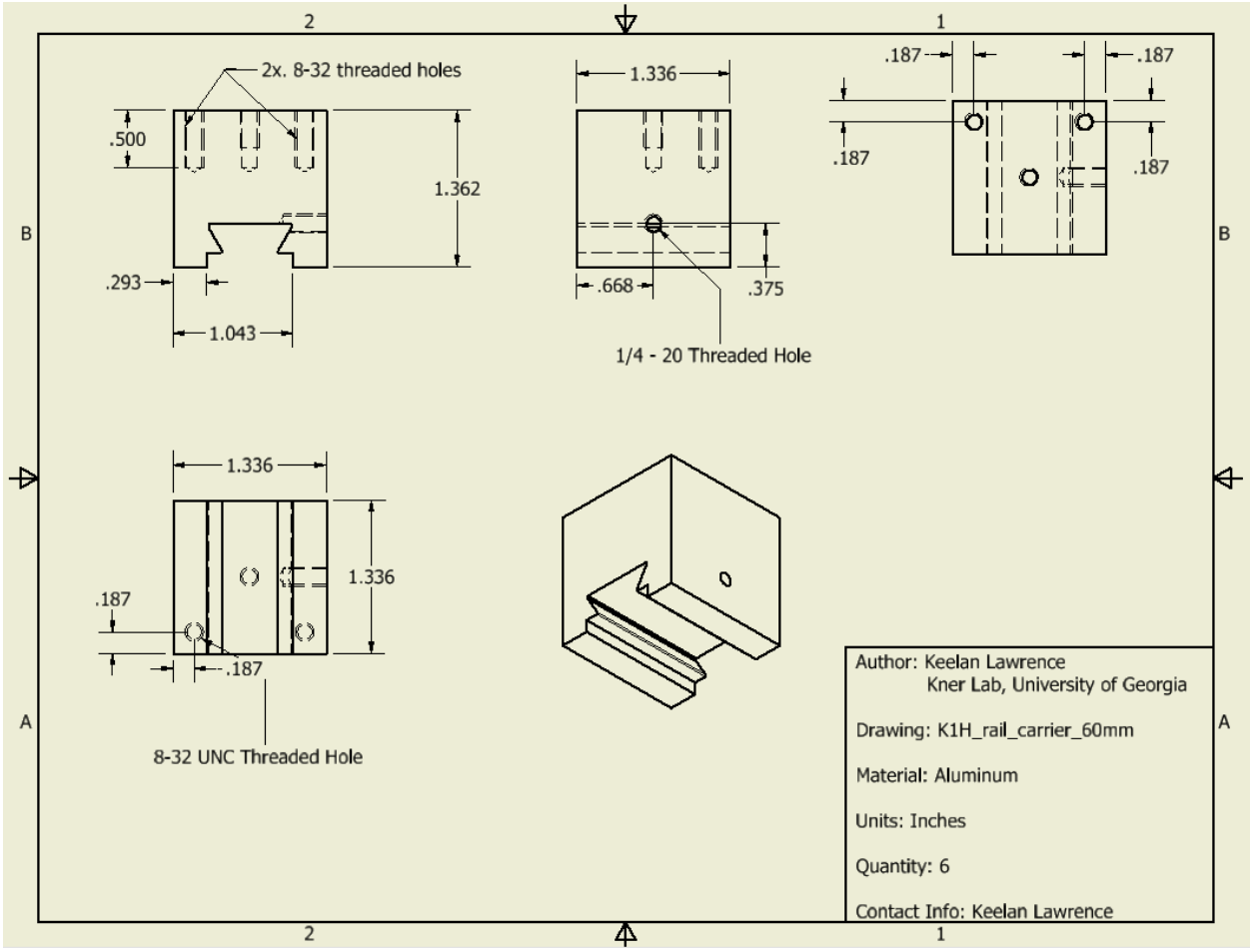
2x. 8-32 threaded holes
.500
1.362
.293
1.043
1.336
.668
.375
1/4 - 20 Threaded Hole
.187
.187
.187
.187
1.336
1.336
.187
.187
8-32 UNC Threaded Hole
Author: Keelan Lawrence
Kner Lab, University of Georgia
Drawing: K1H_rail_carrier_60mm
Material: Aluminum
Units: Inches
Quantity: 6
Contact Info: Keelan Lawrence

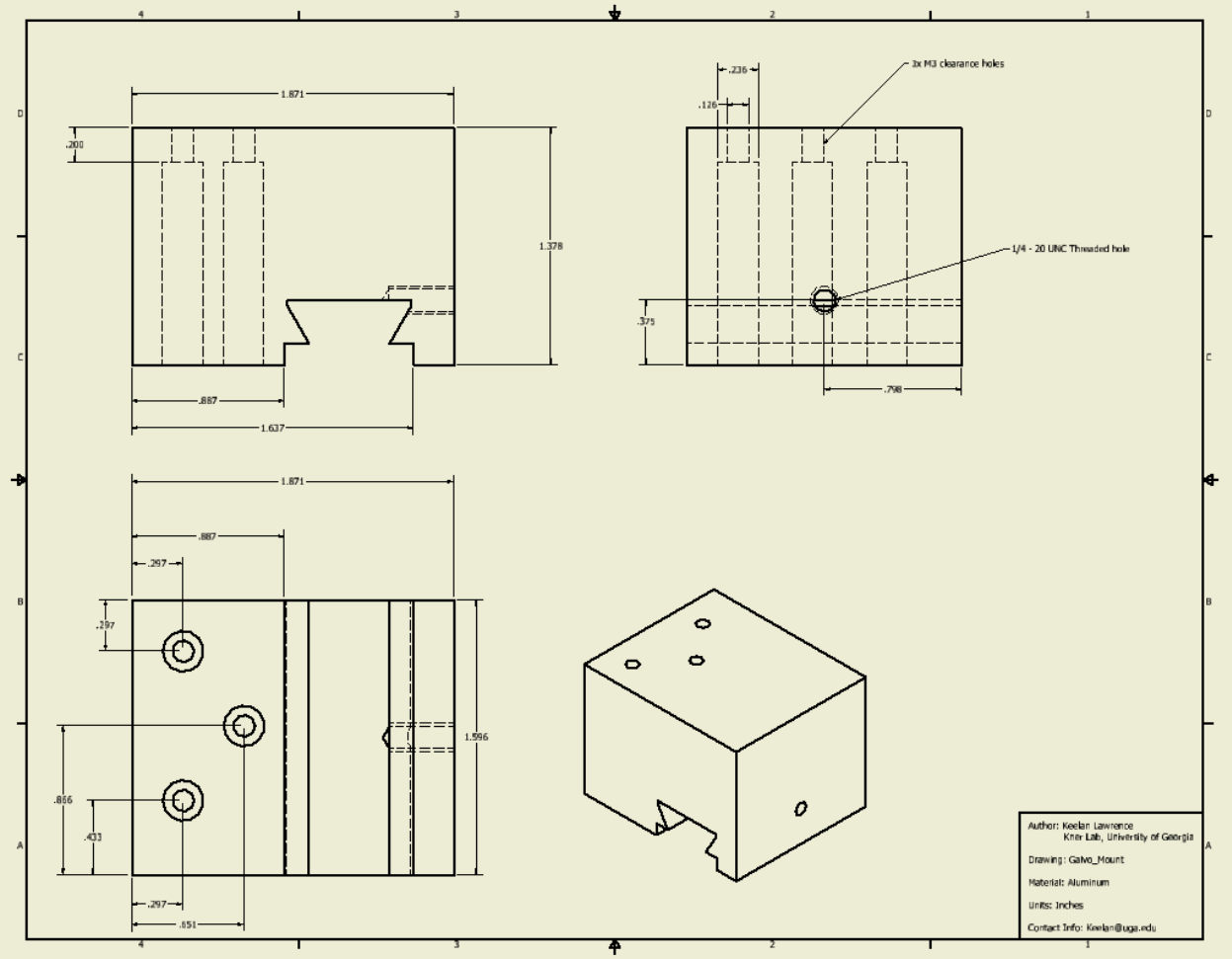
1.871
.200
1.378
.887
1.637
.236
.126
3x M3 clearance holes
1/4 - 20 UNC Threaded hole
.375
.798
1.871
.887
.297
.297
.866
.433
1.596
.297
.651
Author: Keelan Lawrence
Knier Lab, University of Georgia
Drawing: Galvo_Mount
Material: Aluminum
Units: Inches
Contact Info: Keelan@uga.edu

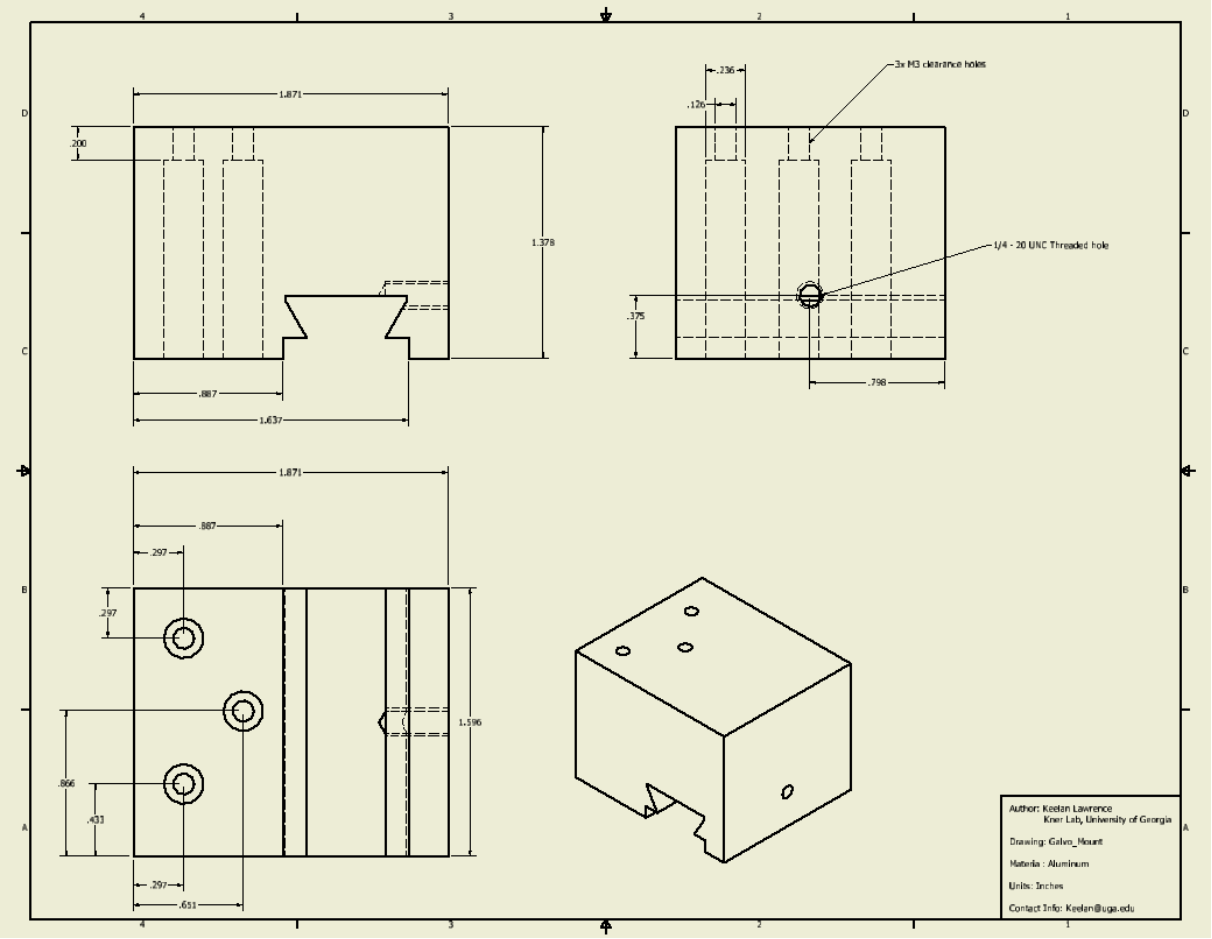
1.871
.200
1.378
.887
1.637
.236
.126
3x M3 clearance holes
1/4 - 20 UNC Threaded hole
.375
.798
1.871
.887
.297
.297
1.596
.866
.431
.297
.651
Author: Keelan Lawrence
Kner Lab, University of Georgia
Drawing: Galvo_Mount
Materia : Aluminum
Units: Inches
Contact Info: Keelan@uga.edu

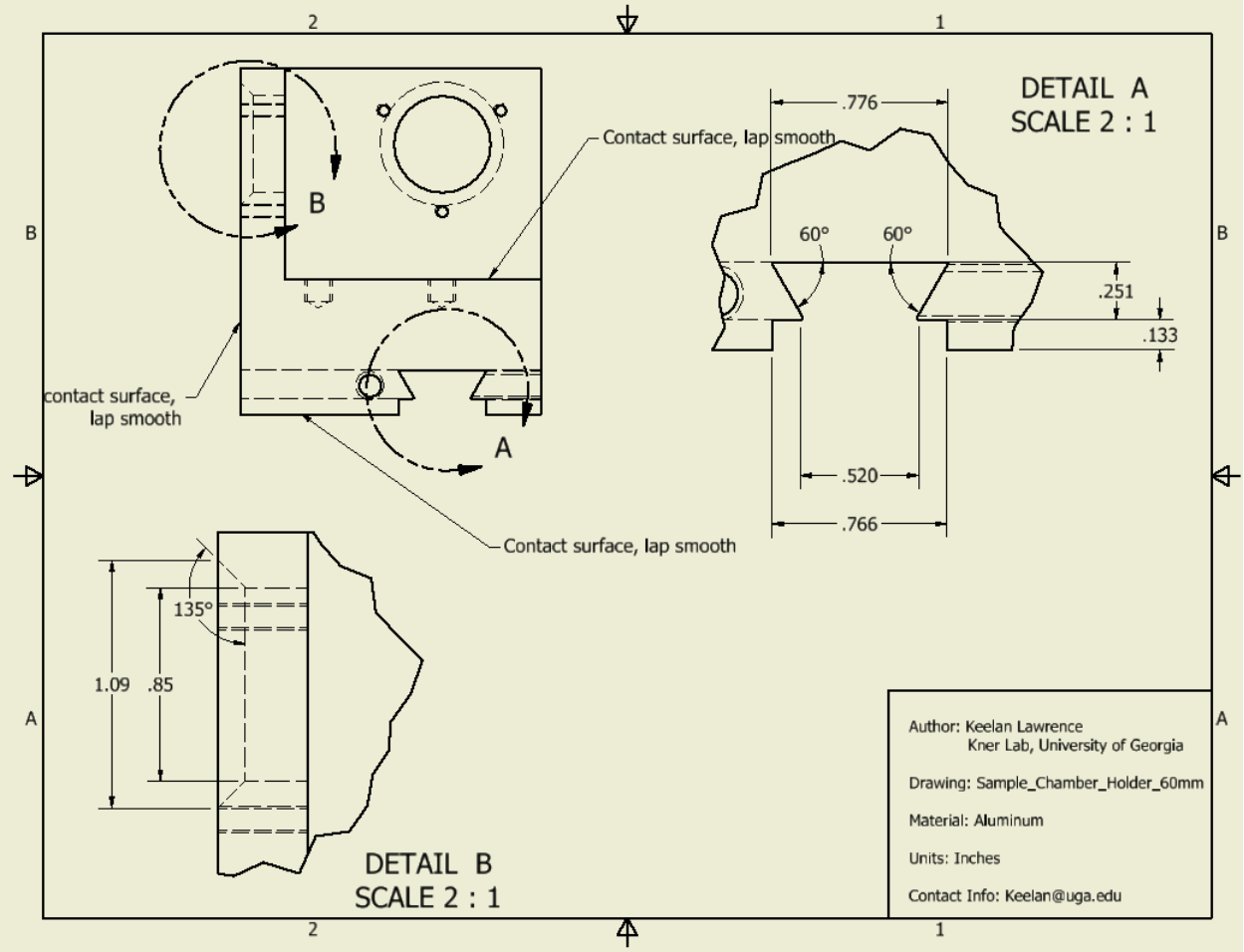
DETAIL A
SCALE 2 : 1
Contact surface, lap smooth
contact surface,
lap smooth
Contact surface, lap smooth
.776
60°
60°
.251
.133
.520
.766
135°
1.09
.85
DETAIL B
SCALE 2 : 1
Author: Keelan Lawrence
Kner Lab, University of Georgia
Drawing: Sample_Chamber_Holder_60mm
Material: Aluminum
Units: Inches
Contact Info: Keelan@uga.edu

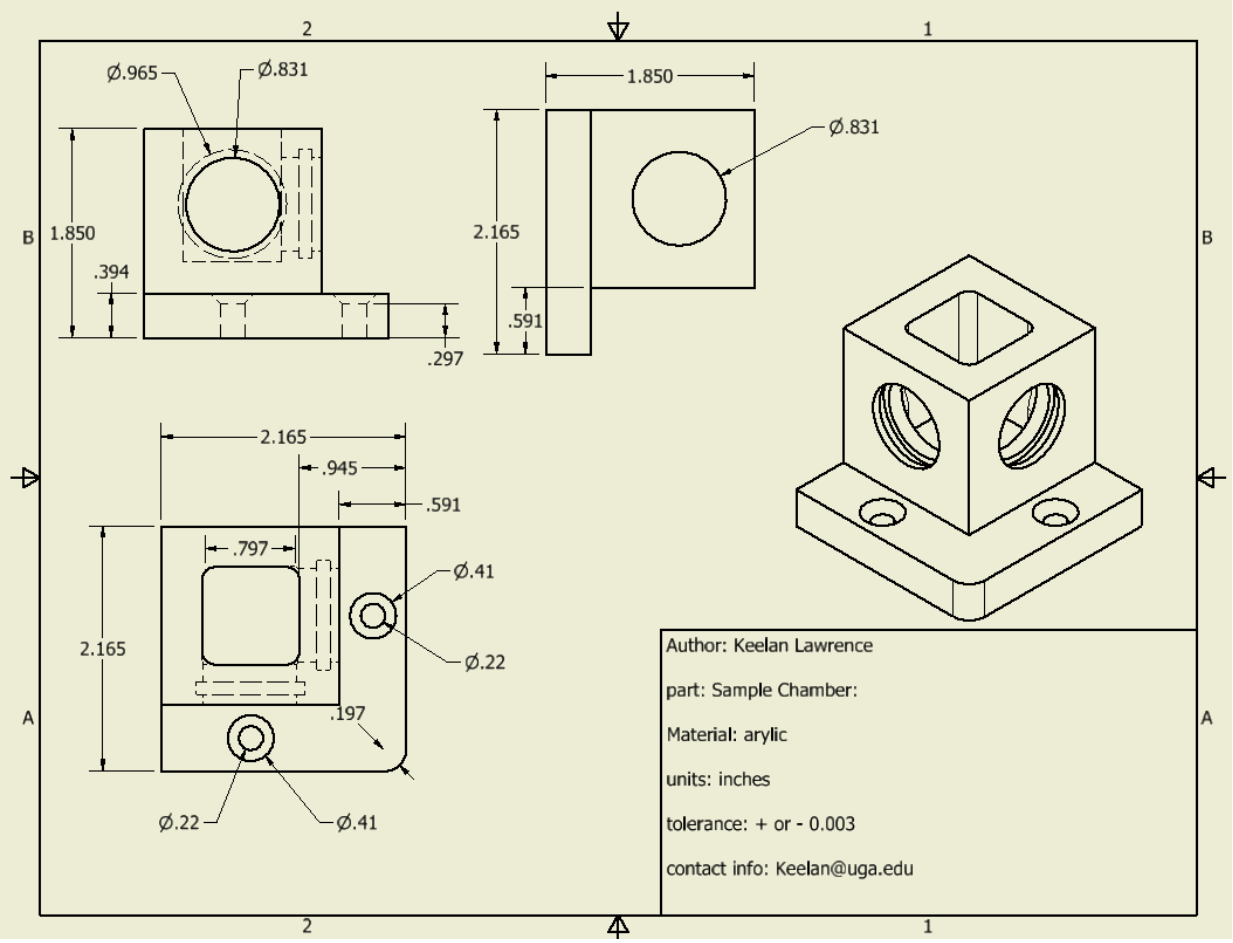
Ø.965
Ø.831
1.850
1.850
.394
.297
2.165
Ø.831
.591
2.165
.945
.591
.797
Ø.41
Ø.22
2.165
.197
Ø.22
Ø.41
Author: Keelan Lawrence
part: Sample Chamber:
Material: arylic
units: inches
tolerance: + or - 0.003
contact info: Keelan@uga.edu

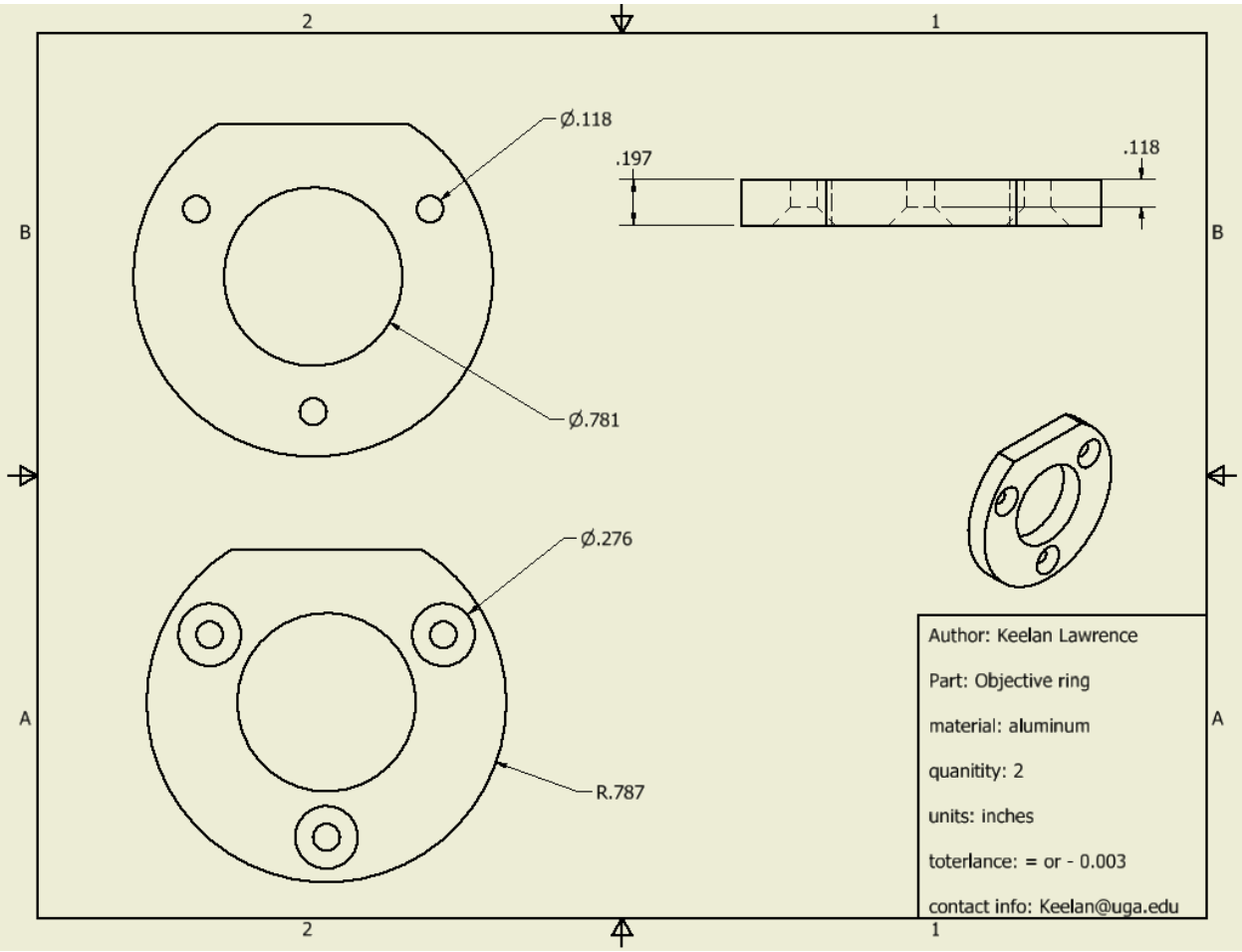
2
1
B
A
Ø.118
.197
.118
Ø.781
Ø.276
R.787
Author: Keelan Lawrence
Part: Objective ring
material: aluminum
quanitity: 2
units: inches
toterlance: = or - 0.003
contact info: Keelan@uga.edu

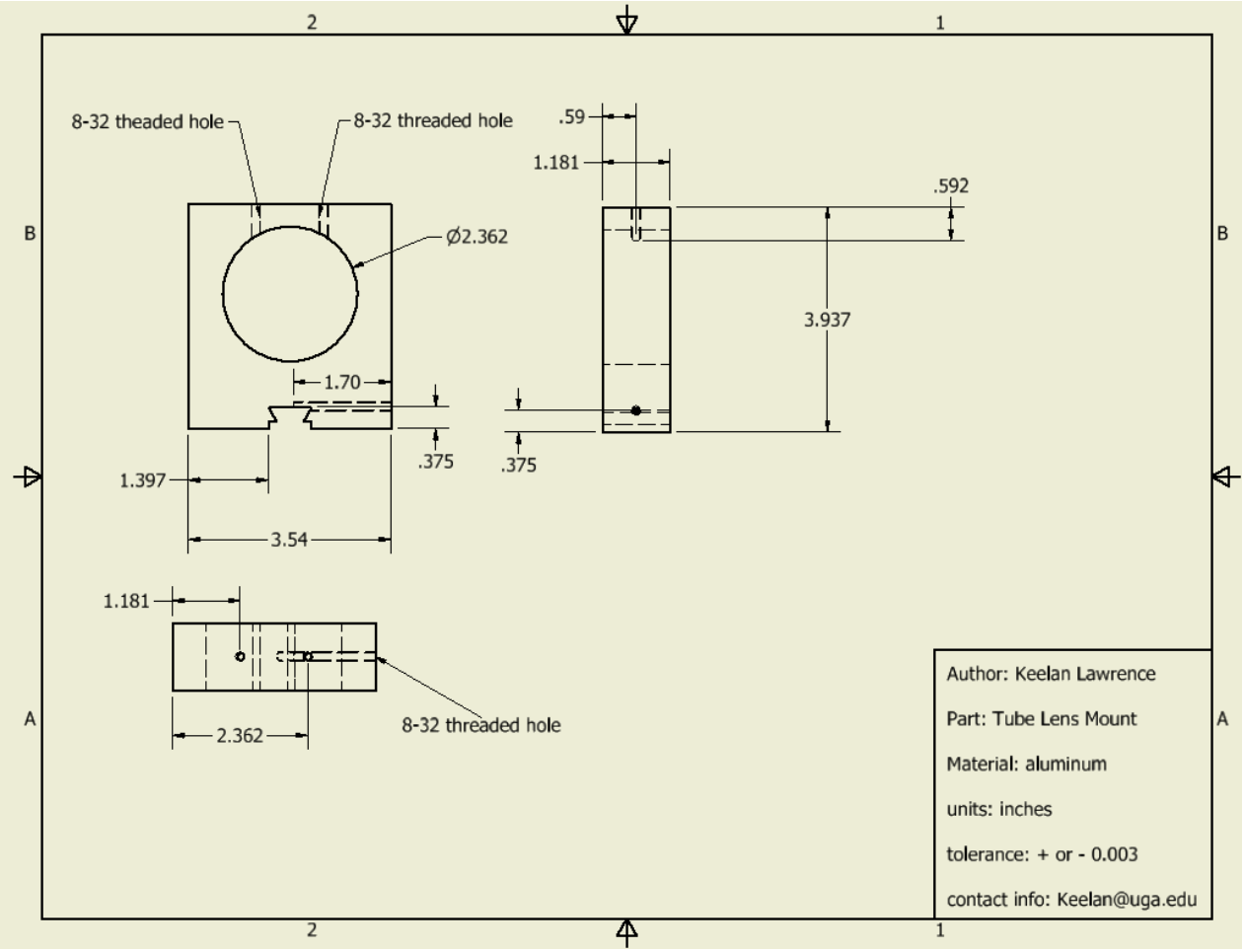
8-32 theaded hole
8-32 threaded hole
.59
1.181
.592
Ø2.362
3.937
1.70
.375
.375
1.397
3.54
1.181
2.362
8-32 threaded hole
Author: Keelan Lawrence
Part: Tube Lens Mount
Material: aluminum
units: inches
tolerance: + or - 0.003
contact info: Keelan@uga.edu

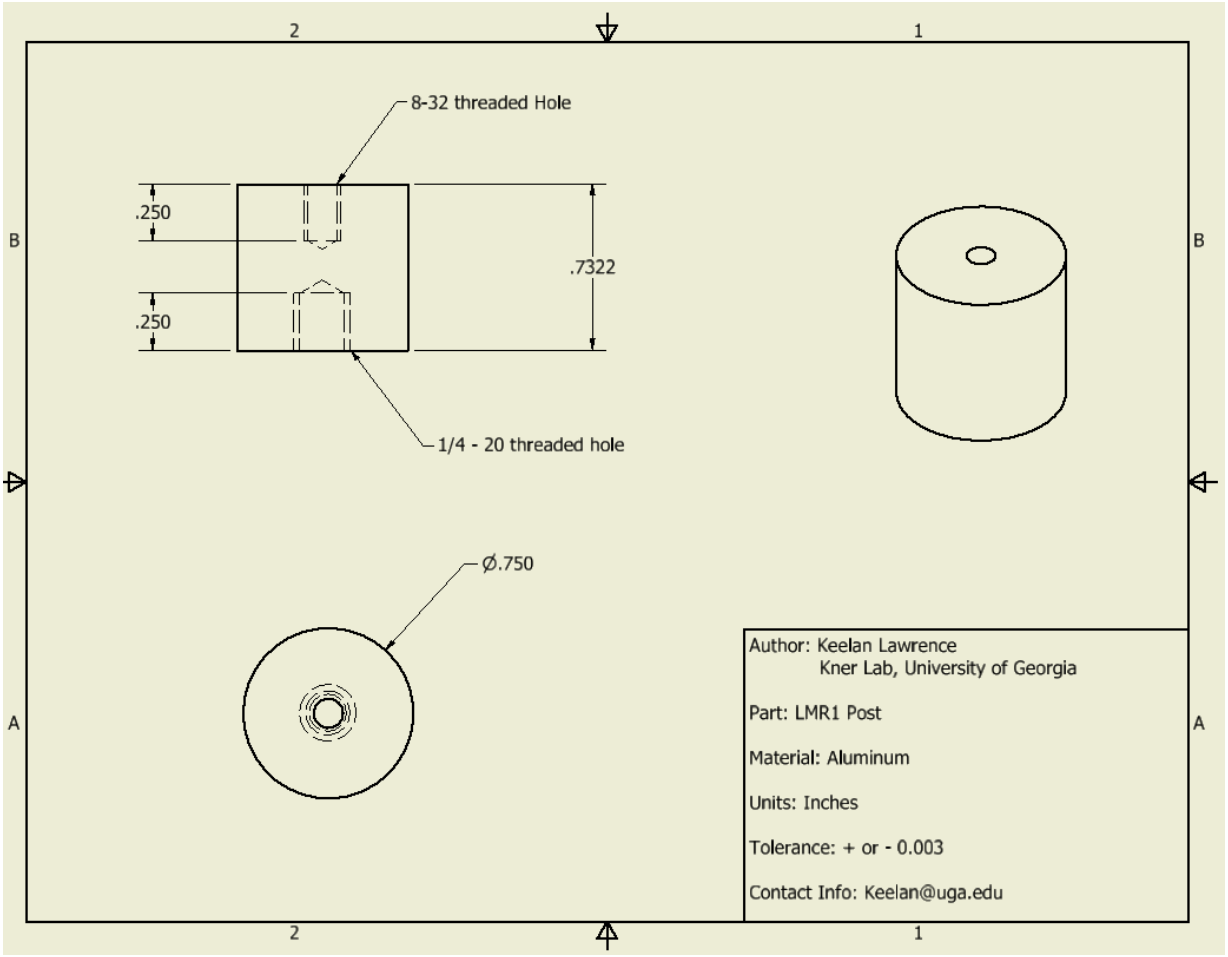
2
1
8-32 threaded Hole
.250
.250
.7322
1/4 - 20 threaded hole
Ø.750
B
A
Author: Keelan Lawrence
Kner Lab, University of Georgia
Part: LMR1 Post
Material: Aluminum
Units: Inches
Tolerance: + or - 0.003
Contact Info: Keelan@uga.edu

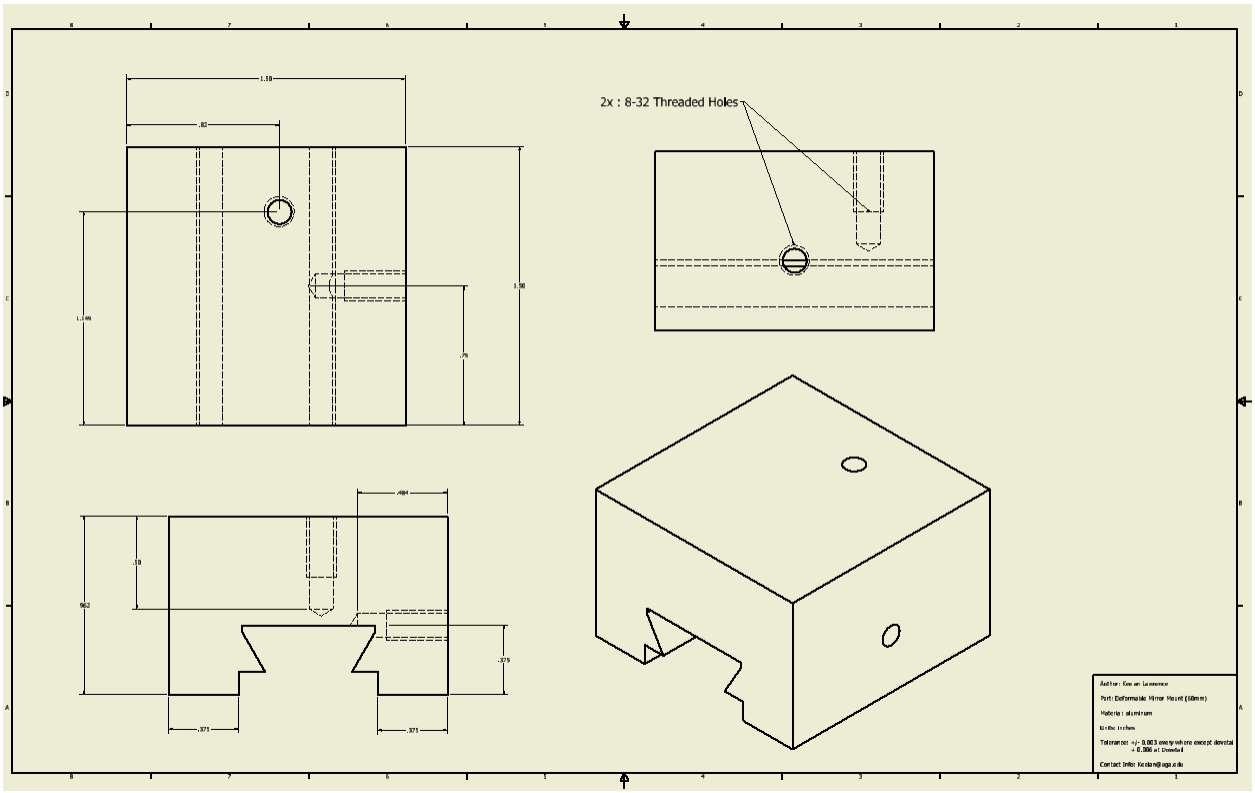
2x : 8-32 Threaded Holes

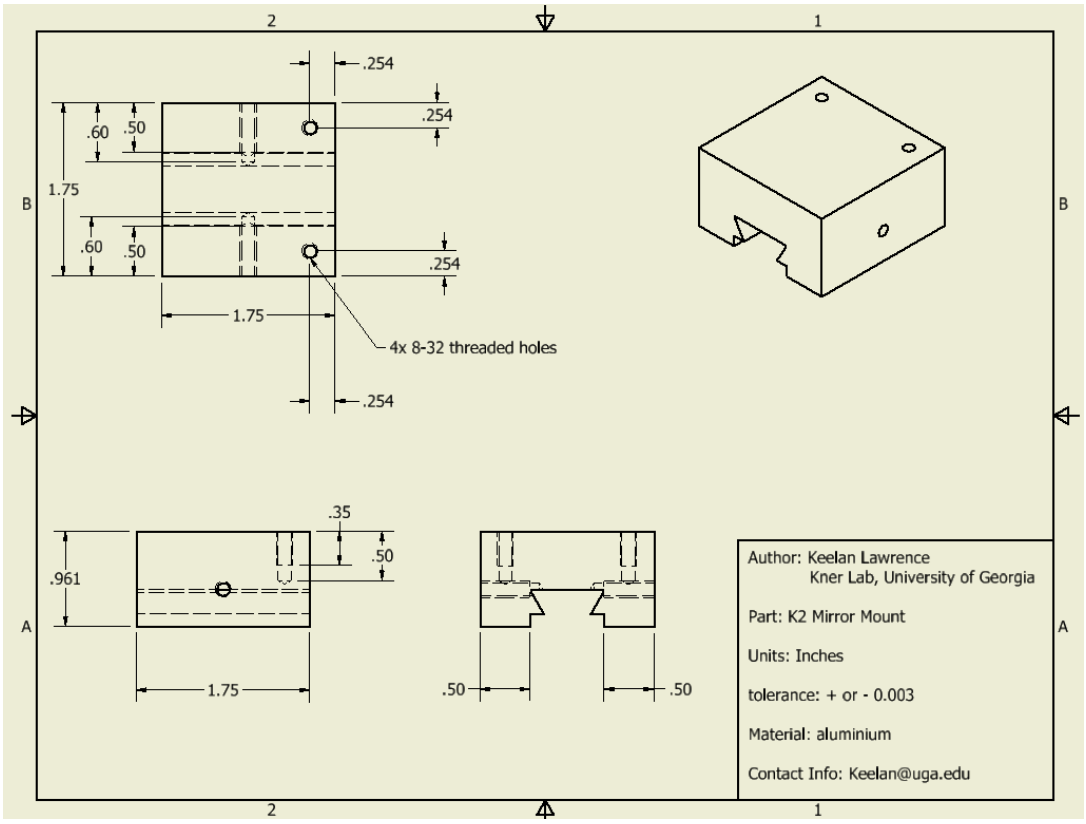
.254
.254
.60
.50
1.75
.60
.50
.254
1.75
4x 8-32 threaded holes
.254
.35
.50
.961
1.75
.50
.50
Author: Keelan Lawrence
Kner Lab, University of Georgia
Part: K2 Mirror Mount
Units: Inches
tolerance: + or - 0.003
Material: aluminium
Contact Info: Keelan@uga.edu

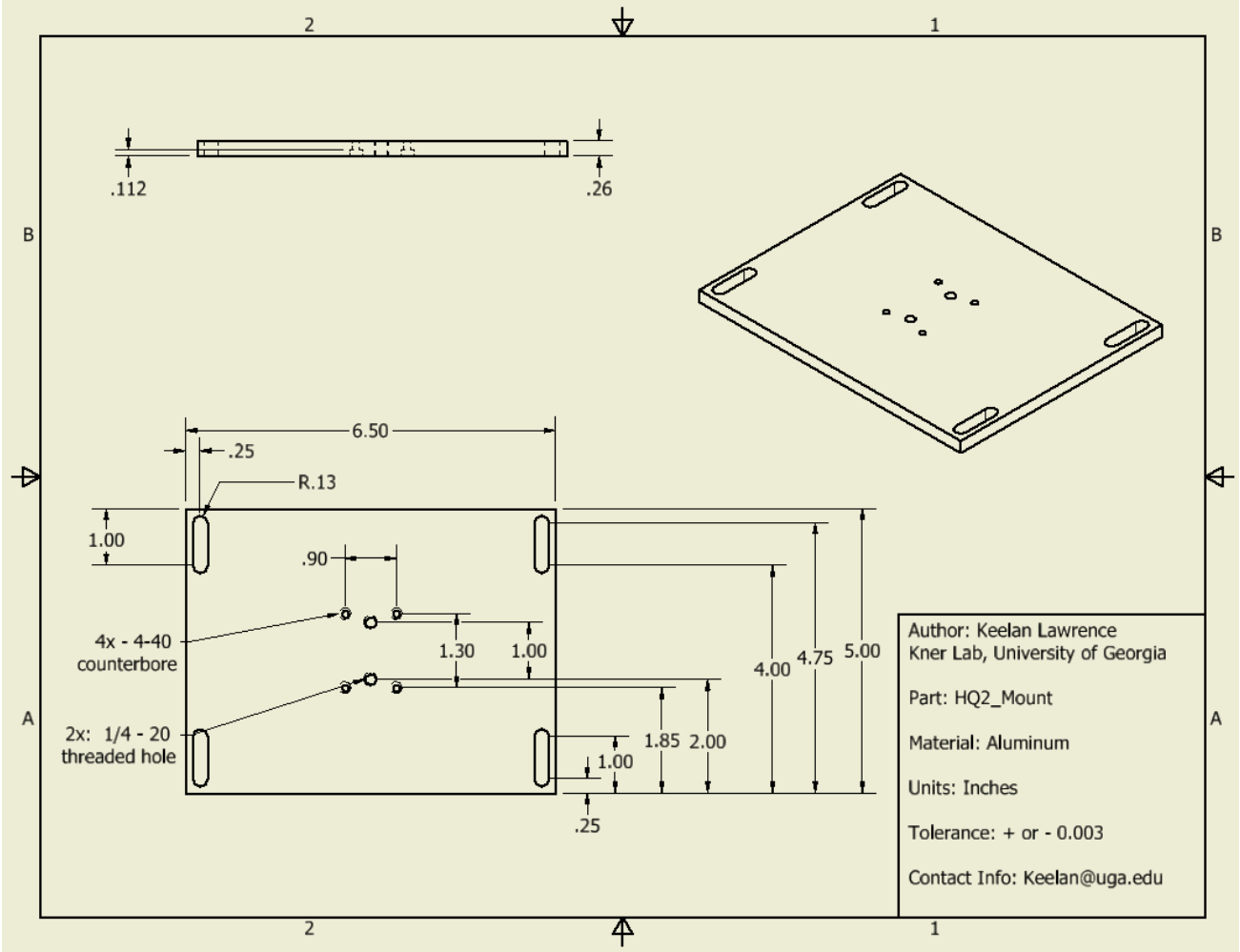
2
1
B
A
.112
.26
6.50
.25
R.13
1.00
.90
4x - 4-40
counterbore
2x: 1/4 - 20
threaded hole
1.30
1.00
1.85
2.00
1.00
.25
4.00
4.75
5.00
Author: Keelan Lawrence
Kner Lab, University of Georgia
Part: HQ2_Mount
Material: Aluminum
Units: Inches
Tolerance: + or - 0.003
Contact Info: Keelan@uga.edu

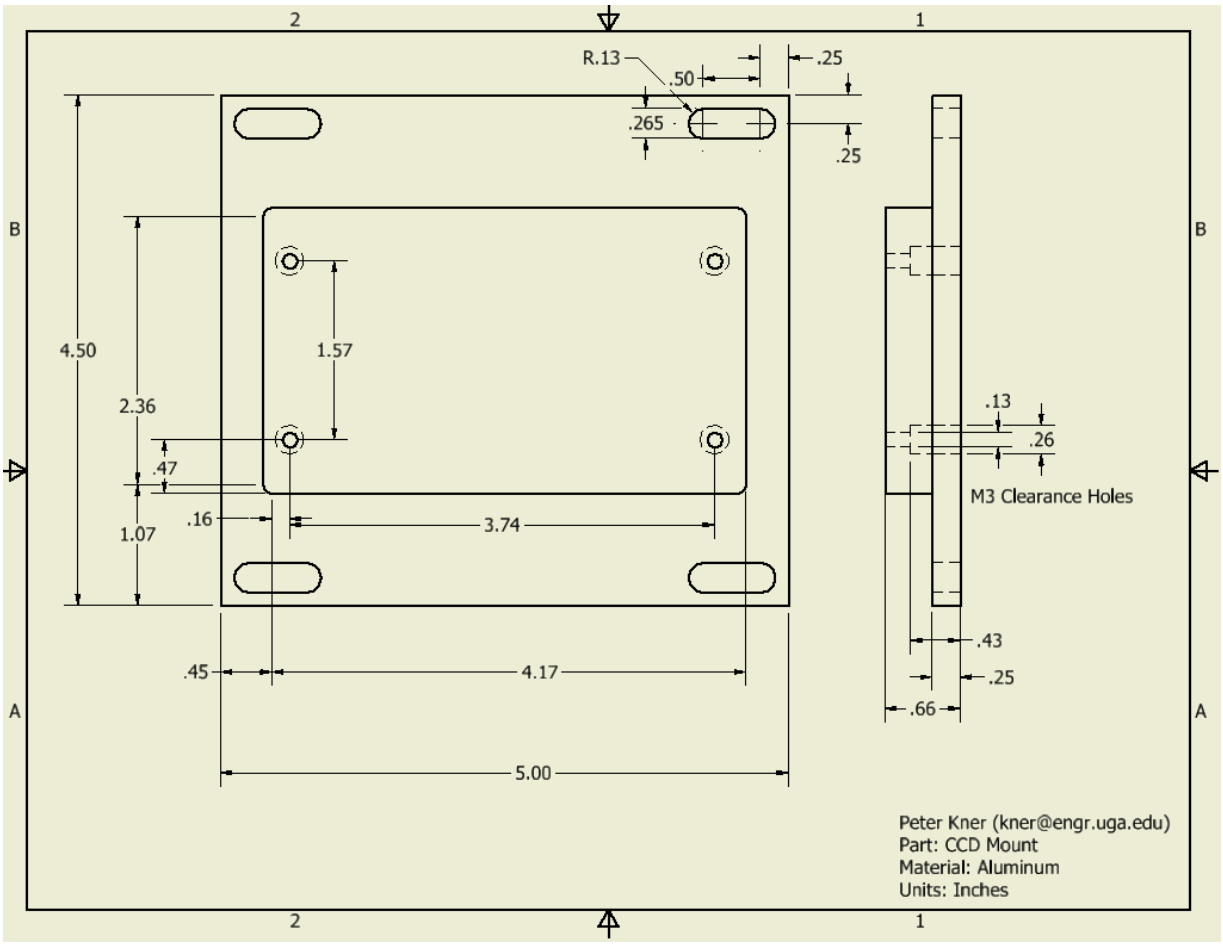
2
1
B
A
R.13
.50
.25
.265
.25
4.50
1.57
2.36
.47
1.07
.16
3.74
.45
4.17
5.00
.13
.26
M3 Clearance Holes
.43
.25
.66
Peter Kner (kner@engr.uga.edu)
Part: CCD Mount
Material: Aluminum
Units: Inches

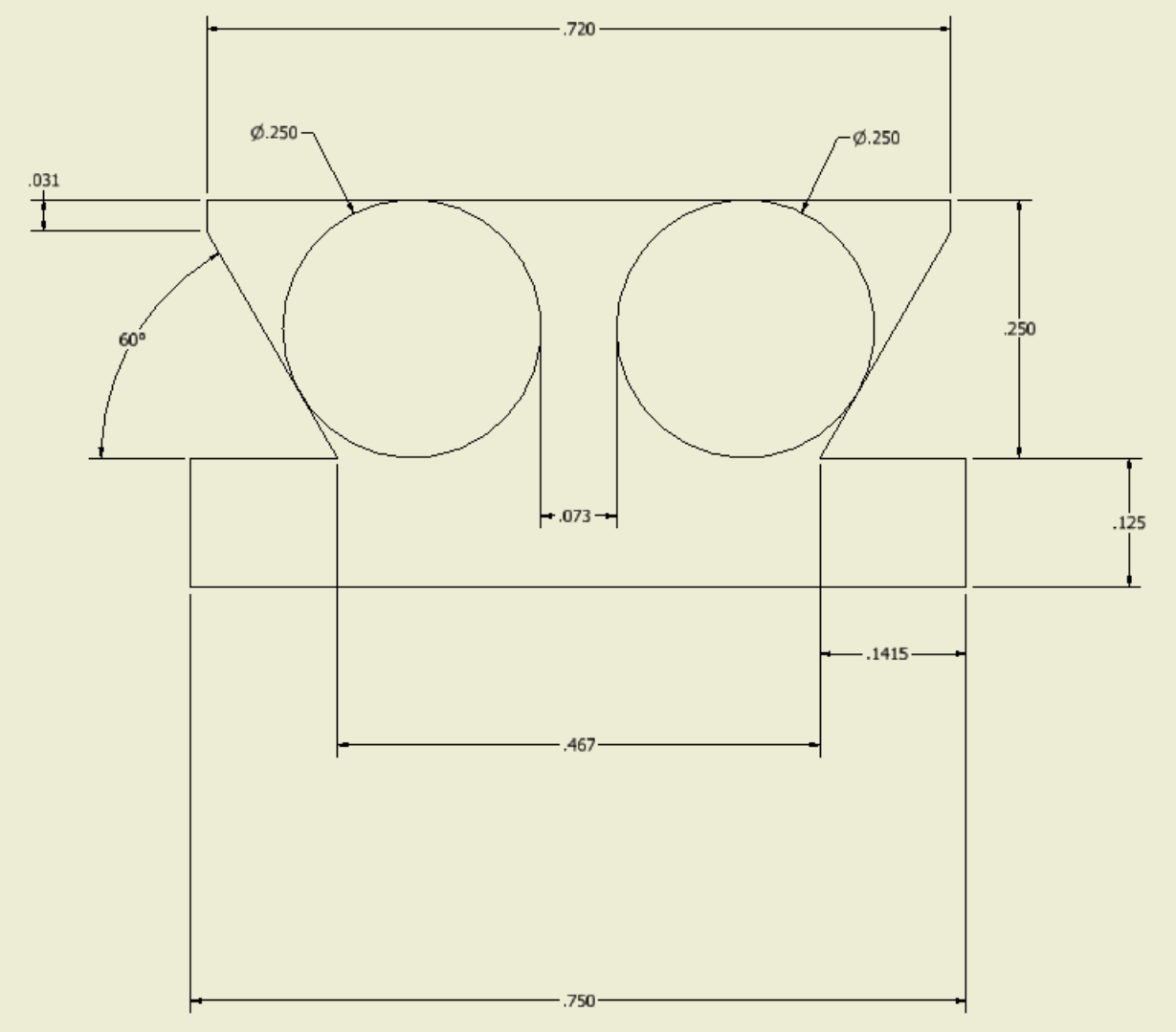
.720
Ø.250
Ø.250
.031
60°
.250
.073
.125
.1415
.467
.750

Software

Below is the python code used for wavefront sensing

```
"""
@author: Keelan
"""
import scipy.ndimage.measurements
com = scipy.ndimage.measurements.center_of_mass
#import AdaptiveThreshold_Opencv as opencv
import tifffile as tf
import numpy as N
import zernike
from pylab import imshow
#from scipy.ndimage import correlate as corr
from scipy.signal import fftconvolve as corr
from scipy.signal import convolve as convolve
from scipy.ndimage.measurements import center_of_mass as sccom
from scipy.ndimage.filters import gaussian_filter
from scipy.signal import detrend

fft2 = N.fft.fft2
ifft2 = N.fft.ifft2
fftshift = N.fft.fftshift
pi = N.pi

class Wavefront_Sensor(object):

    def __init__(self):
        # set up inital parameters to determine size of the scene composition
```

```
        #self.adapt = opencv.adaptivethreshold()
        self.radius = 14
        self.x_center = 583
        self.y_center = 578
        self.px_spacing = 31.0 # spacing between each lenslet
        self.barrier = 10000.0 # maximum intensity value accepted by the camera
        self.threshold = 50.0 # minimum intensity value accepted by the camera
        self.background = 285.0
        self.nx = 2*self.radius # number of lenslets x-direction
        self.ny = 2*self.radius # number of lenslets y-direction
        self.hsp = 15 # size of subimage is 2*hsp
        self.hsplong = self.hsp +1
        self.calfactor = (6.45/4700.0)*(300.0)*(3.0/2.0) # pixel size / focalLength * pitch
*magnification converts pixels to microns
        #wavelength = 0.520
        #radian = wavelength/(2*N.pi)
        #self.calfactor = self.calfactor*wavelength/N.pi
        self.NaN_Mask = self.mask_nan()
        self.Zero_Mask = self.mask_zero()
        # set up seccorr center
        section = N.ones((2*self.hsp+1,2*self.hsp+1)) #if odd sized subimage
        #section = N.ones((2*self.hsp+1,2*self.hsp+1)) #if even sized subimage
        sectioncorr = corr(1.0*section, 1.0*section[::-1,::-1], mode='full')
        self.CorrCenter = N.unravel_index(sectioncorr.argmax(), sectioncorr.shape)
        # Set up T and W filters for waffle removal
        # T
        self.T_Filter = N.zeros((3,3))
        self.T_Filter[0,1] = self.T_Filter[1,0] = self.T_Filter[1,2] = self.T_Filter[2,1] = 0.25
        self.T_Filter[1,1] = 1
```

```
        self.T_Filter = 0.5*self.T_Filter
        # W
        self.W_Filter = N.ones((3,3))
        self.W_Filter[0,0] = self.W_Filter[0,2] = self.W_Filter[2,0] = self.W_Filter[2,2] = 0.25
        self.W_Filter[0,1] = self.W_Filter[1,0] = self.W_Filter[1,2] = self.W_Filter[2,1] = 0.5
        self.W_Filter = 0.25*self.W_Filter
        self.Test_Waffle = N.zeros((3,3))
        self.Test_Waffle2 = N.zeros((3,3))
        self.Test_Waffle[0,1] = self.Test_Waffle[1,0] = self.Test_Waffle[1,2] =
self.Test_Waffle[2,1] = 1.0
        self.Test_Waffle2[0,0] = self.Test_Waffle2[0,2] = self.Test_Waffle2[1,1] =
self.Test_Waffle2[2,0] = self.Test_Waffle2[2,2] = 1.0
        # initialize Arrays
        self.gradx = N.zeros((self.ny,self.nx))
        self.grady = N.zeros((self.ny,self.nx))
        self.gradx_guide = N.zeros((self.ny,self.nx))
        self.grady_guide = N.zeros((self.ny,self.nx))
        self.gradx_Ref = N.zeros((self.ny,self.nx))
        self.grady_Ref = N.zeros((self.ny,self.nx))
        self.hudgins_prep()

    def GetPhiArray2img(self,imagearray):
        phi_array = N.zeros((140,2*self.radius,2*self.radius))
#         gradx_array =
        for i in range (140):
            phi_array[i] = self.GetAberration2img(imagearray[0],imagearray[i+1])
        return phi_array

    def GetPhiArray2img_120(self,imagearray):
```

```
        phi_array = N.zeros((119,2*self.radius,2*self.radius))
#       gradx_array =
        for i in range (119):
            phi_array[i] = self.GetAberration2img(imagearray[0],imagearray[i+1])
        return phi_array

    def GetPhiArray1img_35(self,imagearray):
        phi_array = N.zeros((35,2*self.radius,2*self.radius))
        phi_dif = N.zeros((34,2*self.radius,2*self.radius))
        phi_array[0] = self.GetAberration1img(imagearray[0])
        for i in range (34):
            phi_array[i+1] = self.GetAberration1img(imagearray[i+1])
            phi_dif[i] = phi_array[i+1] - phi_array[0]
        return phi_array,phi_dif

    def GetAberration2img(self,baseimg,offsetimg):
        '''Determines the phase difference between a base and offset image using cross correlation'''
        baseimg = self.background_subtraction(baseimg)
        offsetimg = self.background_subtraction(offsetimg)
        baseimg = self.high_pass_filter(baseimg)
        offsetimg = self.high_pass_filter(offsetimg)
        baseimg = self.low_pass_filter(baseimg)
        offsetimg = self.low_pass_filter(offsetimg)
        gradx,grady = self.GetGradientsCorr(baseimg,offsetimg)
        gradx = gradx*self.Zero_Mask
        grady = grady*self.Zero_Mask
        extx,exty = self.hudgins_extend_mask0(gradx,grady)
        phi = self.recon_hudgins(extx,exty)
```

```
    phi = phi*self.calfactor
    phi = self.RemoveGlobalWaffle(phi)
    phi = phi*self.Zero_Mask
    #phi = self.RemoveLocalWaffle(phi)
    return phi

def get_phi_array(self,imagearray,iters=140):
    phi_array = N.zeros((iters,2*self.radius,2*self.radius))
    for m in range(iters):
        phi_array[m] = self.GetAberration2img(imagearray[0],imagearray[1+m])
    return(phi_array)

def GetAberration1img(self,image):
    image = self.high_pass_filter(image)
    image = self.low_pass_filter(image)
    gradx,grady = self.GetGradientsRef(image)
    #gradx = self.mask*gradx
    #grady = self.mask*grady
    median_x = self.Median_reduction(gradx)
    median_y = self.Median_reduction(grady)
    gradx = 1.0*gradx - median_x
    grady = 1.0*grady - median_y
    gradx = gradx*self.Zero_Mask
    grady = grady*self.Zero_Mask
    extx,exty = self.hudgins_extend_mask0(gradx,grady)
    phi = self.recon_hudgins(extx,exty)
    phi = phi*self.calfactor
    phi = self.RemoveGlobalWaffle(phi)
```

```
    #phi = phi*self.NaN_Mask
    phi = phi*self.Zero_Mask
    return phi

def GetBaseGradients1img(self,image):
    image = self.high_pass_filter(image)
    image = self.low_pass_filter(image)
    gradx,grady = self.GetGradientsRef(image)
    #gradx = self.mask*gradx
    #grady = self.mask*grady
    median_x = self.Median_reduction(gradx)
    median_y = self.Median_reduction(grady)
    gradx = 1.0*gradx - median_x
    grady = 1.0*grady - median_y
    gradx = gradx*self.Zero_Mask
    grady = grady*self.Zero_Mask
    base_grad_x,base_grad_y = self.hudgins_extend_mask0(gradx,grady)
    return base_grad_x,base_grad_y

def GetGradientsCorr(self,baseimg,offsetimg):
    ''' Determines Gradients by Correlating each section
        with its base reference section'''
    for ii in range(self.nx):
        for jj in range(self.ny):
            gradx,grady = self.findDotsCorrelateoff(baseimg,offsetimg,jj,ii)
            self.gradx[jj,ii] = gradx# + 0.5
            self.grady[jj,ii] = grady# + 0.5
    return self.gradx,self.grady
```

```
def GetGradientsGuide(self,baseimg,offsetimg):
    ''' Determines Gradients using center of mass'''
    for ii in range(self.nx):
        for jj in range(self.ny):
            gradx,grady = self.findDotsCOM(baseimg,offsetimg,jj,ii)
            self.gradx_guide[jj,ii] = gradx# + 0.5
            self.grady_guide[jj,ii] = grady# + 0.5
    return self.gradx_guide,self.grady_guide

def GetGradientsRef(self,image):
    ''' Determines Gradients from a single image by Correlating
        Each section with a reference section'''
    for ii in range(self.nx):
        for jj in range(self.ny):
            gradx,grady = self.findDotsRef(image,jj,ii)
            self.gradx_Ref[jj,ii] = gradx
            self.grady_Ref[jj,ii] = grady
    #self.gradx_Ref = self.gradx_Ref*self.mask_grads
    #self.grady_Ref = self.grady_Ref*self.mask_grads
    #mask[mask == 0.0] = 'nan'
    #self.gradx_Ref[self.gradx_Ref == 0.0] = 'nan'
    #self.grady_Ref[self.grady_Ref == 0.0] = 'nan'
    #self.gradx_Ref = (self.Median_reduction(self.gradx_Ref))#*(-1.0)# + 0.5
    #self.grady_Ref = (self.Median_reduction(self.grady_Ref))#*(-1.0)# + 0.5
    #self.gradx_Ref[N.isnan(self.gradx_Ref)] = 0.0
    #self.grady_Ref[N.isnan(self.grady_Ref)] = 0.0
    #self.gradx_Ref[self.gradx_Ref == 'nan'] = 0.0
```

```
    #self.grady_Ref[self.grady_Ref == 'nan'] = 0.0
    return self.gradx_Ref,self.grady_Ref

def Median_reduction(self,gradient):
    # Reduces the values of all gradients by the values of the median gradient
    gradient = gradient*self.NaN_Mask
    median = N.nanmedian(gradient)
    return median

def background_subtraction(self,image):
    image = image - self.background*N.ones((1040,1040))
    image = image.clip(min=0.0)
    return image

def setZernike(self,mode, amp):
    phiin = amp*zernike.Zm(mode,rad=10, orig=None,Nx=19) # was 28
    # set mirror with new dm shape
    return phiin

def ZernikeLoop(self,amp=0.5,radius=11):
    phi_array = N.zeros((25,2*radius,2*radius))
    for k in range(25):
        phi = self.setZernike(k,amp)
        phi_array[k] = phi
    return phi_array

def Get_RMS(self,phi):
    rms = N.sqrt(N.mean(phi**2))
```

```
        return rms

    def Get_RMS_loop(self,dif):
        rms_array = N.zeros(119)
        for k in range(119):
            rms_array[k] = self.Get_RMS(dif[k])
#           print rms_array[k]
        return rms_array

    def Get_maximum_loop(self,phis):
        phis_array = N.zeros(140)
        for k in range(140):
            phis_array[k] = phis[k].max()
#           print phis[k].max()
        return phis_array

#   def LinearReg_reduction(self,gradient):
        # Redcues the values off all gradients by the central value of the linear fit


    def findDot(self,image,iy,ix):
        hsp = self.hsp
        hsp1 = self.hsplong
        bot = self.y_center - (self.radius)*self.px_spacing
        left = self.x_center - (self.radius)*self.px_spacing
        vert = int(bot + iy*self.px_spacing)
        horiz = int(left + ix*self.px_spacing)
        sec = image[(vert-hsp):(vert+hsp1),(horiz-hsp):(horiz+hsp1)]
```

```
    return sec

def findDots(self,image):
    dotarray = N.zeros((self.nx*self.ny,2*self.hsp,2*self.hsp))
    count = 0
    for ii in range(self.nx):
        for jj in range(self.ny):
            sec = self.findDot(image,jj,ii)
            dotarray[count] = sec
            #print jj,ii
            count = count + 1
    return dotarray

def findDotsCorrelateoff(self,baseimg,offsetimg,iy,ix):
    '''finds new spots using each section correlated with the center'''
    #CorrCenter = self.CorrCenter.copy()
    hsp = self.hsp
    hsp1 = self.hsplong
    bot = self.y_center - (self.radius)*self.px_spacing
    left = self.x_center - (self.radius)*self.px_spacing
    vert = int(bot + iy*self.px_spacing)
    horiz = int(left + ix*self.px_spacing)
    sec = offsetimg[(vert-hsp):(vert+hsp1),(horiz-hsp):(horiz+hsp1)]
    secbase = baseimg[(vert-hsp):(vert+hsp1),(horiz-hsp):(horiz+hsp1)]
    seccorr = corr(1.0*secbase, 1.0*sec[::-1,::-1], mode='full')
    #seccorrnorm = seccorr*(1.0/N.sum(seccorr))
    try:
    # Corrects for sub-images leaving the sub-field of view by setting the local gradient to zero
```

```
            px,py = self.Parabolicfit(seccorr)
        except: #IndexError
            px,py = self.CorrCenter[1],self.CorrCenter[0]
            #print ix,iy, "Scene Left SubImage"
        gradx = self.CorrCenter[1] - px
        grady = self.CorrCenter[0] - py
        return gradx,grady

    def findDotsCOM(self,baseimg,offsetimg,iy,ix):
        ''' Find Dot location using center of Mass'''
        hsp = self.hsp
        #hsp1 = self.hsplong
        bot = self.y_center - (self.radius)*self.px_spacing
        left = self.x_center - (self.radius)*self.px_spacing
        vert = int(bot + iy*self.px_spacing)
        horiz = int(left + ix*self.px_spacing)
        sec = offsetimg[(vert-hsp):(vert+hsp),(horiz-hsp):(horiz+hsp)]
        secbase = baseimg[(vert-hsp):(vert+hsp),(horiz-hsp):(horiz+hsp)]
        py,px = sccom(sec)
        sy,sx = sccom(secbase)
        gradx = px - sx
        grady = py - sx
        return (gradx,grady)

    def findDotsRef(self,image,iy,ix):
        ''' find dot location using correlations and parabolic fit'''
        #image = self.high_pass_filter(image)
        hsp = self.hsp
```

```
        #hsp1 = self.hsplong
        bot = self.y_center - (self.radius)*self.px_spacing
        left = self.x_center - (self.radius)*self.px_spacing
        vert = int(bot + iy*self.px_spacing)
        horiz = int(left + ix*self.px_spacing)
        vertmiddle = int(self.y_center)
        horizmiddle = int(self.x_center)
        sec = image[(vert-hsp):(vert+hsp),(horiz-hsp):(horiz+hsp)]
        #sec = self.Threshold_local(self,sec)
        #sec = self.high_pass_filter(sec)
        secmiddle = image[(vertmiddle-hsp):(vertmiddle+hsp),(horizmiddle-
hsp):(horizmiddle+hsp)]
        #secmiddle = self.Threshold_local(self,secmiddle)
        #secmiddle = self.high_pass_filter(secmiddle)
        seccorr = corr(1.0*secmiddle, 1.0*sec[::-1,::-1], mode='full')
        px,py = self.Parabolicfit(seccorr)
        gradx = px
        grady = py
        return gradx,grady


    def FindDotsMaxInt(self,image):
        image = self.high_pass_filter(image)
        intensityarray = N.zeros((self.nx,self.nx))
        count = 0
        for ii in range(self.nx):
            for jj in range(self.ny):
                sec = self.findDot(image,jj,ii)
                maximum = sec.max()
                intensityarray[jj,ii] = maximum
```

```
            #print jj,ii
            count = count + 1
        return intensityarray


    #Removes Waffle mode see "Fast wave-front reconstruction in large adaptive optics
systems....Poyneer,Gavel,Brase
#    def get_mask(self):
#        self.wv_mask = N.zeros((2*self.radius,2*self.radius))
#        for i in range(2*self.radius):
#            for k in range(2*self.radius):
#                if self.placement_mask[i,k] >=0:
#                    self.wv_mask[i,k] = 1


    def RemoveGlobalWaffle(self,phi):
        wmode = N.zeros((2*self.radius,2*self.radius)) # was originally (50,50)
        constant_num = 0
        constant_den = 0
        # a waffle-mode vector of +-1 for a given pixel of the Wavefront
        for x in range(2*self.radius):
            for y in range(2*self.radius):
                if (x+y)/2 - N.round((x+y)/2)==0:
                    wmode[y,x] = 1
                else:
                    wmode[y,x] = -1
        wmode = wmode
        self.temp = wmode
        for i in range(2*self.radius):
            for k in range(2*self.radius):
                temp = phi[i,k]*wmode[i,k]
```

```
            temp2 = wmode[i,k]*wmode[i,k]
            constant_num = constant_num+temp
            constant_den = constant_den+temp2
    constant = constant_num/constant_den
    #print constant
    phicorr = (phi - constant*wmode)
    return phicorr

def RemoveLocalWaffle(self,phi):
    # initialize DM_map corrected for local waffle
    phi_corrected = N.zeros((2*self.radius,2*self.radius))
    for ii in range(2*self.radius-2):
        for jj in range(2*self.radius-2):
            img3x3 = phi[((1+jj)-1):((1+jj)+2),((1+ii)-1):((1+ii)+2)]
            phi_corrected[jj+1,ii+1] = N.sum(img3x3*self.T_Filter)
    phi_corrected[:,0] = phi[:,0]
    phi_corrected[:,2*self.radius-1] = phi[:,2*self.radius-1]
    phi_corrected[0,] = phi[0,]
    phi_corrected[2*self.radius-1,] = phi[2*self.radius-1,]
    return phi_corrected

def high_pass_filter(self,data):
    y,x = data.shape
    data[data<self.threshold] = 0.0
    return data

def low_pass_filter(self,data):
    y,x = data.shape
```

```
        data[data>self.barrier] = 0.0
        return data

    def Threshold_local(self,section,threshold=0.9):
        maximum = section.max()
        section[section<threshold*maximum] = 0.0
        return section

    def Parabolicfit(self,sec):
        try:
            MaxIntLoc = N.unravel_index(sec.argmax(), sec.shape)
            secsmall = sec[(MaxIntLoc[0]-1):(MaxIntLoc[0]+2),(MaxIntLoc[1] -1):(MaxIntLoc[1] +
2)]
            gradx =  MaxIntLoc[1] + 0.5*(1.0*secsmall[1,0] - 1.0*secsmall[1,2])/(1.0*secsmall[1,0]
+ 1.0*secsmall[1,2] - 2.0*secsmall[1,1])
            grady =  MaxIntLoc[0] + 0.5*(1.0*secsmall[0,1] - 1.0*secsmall[2,1])/(1.0*secsmall[0,1]
+ 1.0*secsmall[2,1] - 2.0*secsmall[1,1])
        except: #IndexError
            gradx =  self.CorrCenter[1]
            grady =  self.CorrCenter[0]
        gradx = gradx
        grady = grady
        return gradx,grady

    def Get_Parabolic_WF(self):
        actsimage = N.zeros((19,19))
        centerx = 9
        centery = 9
        for ii in range(19):
```

```
        for jj in range(19):
            radius = N.sqrt((centerx-ii)**2 + ((centery-jj)**2))
            actsimage[jj,ii] = 0.2 - radius*0.01
    actsimage = actsimage - actsimage.mean()
    return actsimage


  def SVD_to_CMD(self,SVD):
    '''Creates a 1-d vector of size 100 for the using the center 10x10 actuators '''
    cmd = 0.5*N.ones(140)
    count = 0
    for k in range(10):
        for m in range(10):
            x = m
            y = 12*(k+1)
            cmd[(x+y)-1] = SVD[count]
            count = count + 1
    return cmd


  def invert_influence_fcn(self,act_wf,ns=75):
    ''' ns is the number of singular values to retain '''
    no_acts = 140
    sx = 28
    #sx = 2*sens.compositeimage.radius # number of Shack-Hartmann spots in the linear
direction
    swf = sx*sx # total number of SH spots
    phis2 = N.zeros((swf,140))
    for m in range(no_acts):
        phis2[:,m] = act_wf[m].reshape(swf)
    u,s,vh = N.linalg.svd(phis2,0,1) # Single Value Decompostion
```

```
    t = (u.reshape(sx,sx,no_acts)).swapaxes(1,2).swapaxes(0,1) # view Eigen Vectors

    ut = N.transpose(u)
    sd = 1./s
    s = N.zeros((no_acts,no_acts))
    for i in range(ns):
        s[i,i] = sd[i]
    v = N.transpose(vh)
    T = N.dot(v,s)
    S = N.dot(T,ut)
    tf.imsave('Inverse_Matrix.tif',S.astype('float32'))
    tf.imsave('eigin_modes.tif',t.astype('float32'))
    tf.imsave('T_maxtrix.tif',T.astype('float32'))
    tf.imsave('v_maxtrix.tif',v.astype('float32'))
    tf.imsave('phis_inverted.tif',phis2.astype('float32'))
    return S,T,t,v,phis2

def compositeimgoff(self,baseimg,threshold=0.75):
    images = []
    for i in range(self.nx):
        row = []
        for j in range(self.nx):
            dot = self.findDot(baseimg,i,j)
            dot = self.low_pass_filter(dot)
            dot = self.Threshold_local(dot,threshold)
            row.append(dot)
        images.append(row)
```

```
    flat = []
    for image_row in images:
        for flatrow_index in range(len(images[0][0])):
            flatrow = []
            for image in image_row:
                for pixel in image[flatrow_index]:
                    flatrow.append(pixel)
            flat.append(flatrow)
    flatarray = N.asarray(flat)
    return flatarray

def compositeimgcorr(self,baseimg,offsetimage):
    images = []
    for i in range(self.nx):
        row = []
        for j in range(self.nx):
            secbase = self.findDot(baseimg,i,j)
            secoff = self.findDot(baseimg,i,j)
            seccorr = corr(1.0*secbase, 1.0*secoff[::-1,::-1], mode='full')
            row.append(seccorr)
        images.append(row)

    flat = []
    for image_row in images:
        for flatrow_index in range(len(images[0][0])):
            flatrow = []
            for image in image_row:
```

```
            for pixel in image[flatrow_index]:
                flatrow.append(pixel)
        flat.append(flatrow)
    flatarray = N.asarray(flat)
    return flatarray

def mask_zero(self):
    # Mask
    a = self.radius #14  # center variable of mask (a,b)
    b = self.radius #14  # center variable of mask (a,b)
    Ly = 2*self.radius #28 # y dimension of image
    Lx = 2*self.radius #28 # x dimension of image
    r1 = self.radius -1 #13 # radius of mask
    y, x = N.ogrid[-a:Ly-a, -b:Lx-b] #creates a meshgrid centered at (a,b)
    mask = x**2 + y**2 <= r1**2
    mask[1,a] = mask[a,1] = mask[a,Lx-1] = mask[Ly-1,a] = 0.0
    mask = mask.astype('float')
    #mask[mask == 0.0] = 'nan'
    return mask

def mask_nan(self):
    a = self.radius  # center variable of mask (a,b)
    b = self.radius  # center variable of mask (a,b)
    Ly = 2*self.radius # y dimension of image
    Lx = 2*self.radius # x dimension of image
    r1 = self.radius -1 # radius of mask
    y, x = N.ogrid[-a:Ly-a, -b:Lx-b] #creates a meshgrid centered at (a,b)
    mask = x**2 + y**2 <= r1**2
```

```
    mask[1,a] = mask[a,1] = mask[a,Lx-1] = mask[Ly-1,a] = 0.0
    mask = mask.astype('float')
    mask[mask == 0.0] = 'nan'
    return mask

def recon_hudgins(self,gradx,grady):
    ''' wavefront reconstruction from gradients
        Hudgins Geometry, Poyneer 2002 '''
    sx = fft2(fftshift(gradx))
    sy = fft2(fftshift(grady))
    numx = self.numx
    numy = self.numy
    den = self.den
    self.sw = (numx*sx + numy*sy)/den
    self.sw[0,0] = 0.0
    #self.sw[nx/2,nx/2] = 0.0
    phi = fftshift(ifft2(self.sw)).real
    return phi

def hudgins_extend_masknan(self,gradx,grady):
    ''' extension tecchnique Poyneer 2002 '''
    nx = self.nx
    ny = self.ny
    if (nx % 2 == 0): #even
        mx = nx/2
    else: #odd
        mx = (nx+1)/2
    for jj in range(int(nx)):
```

```
        for ii in range(int(mx),int(nx)):
            if grady[jj,ii] == ('nan'):
                grady[jj,ii] = grady[jj,ii-1]
            if gradx[ii,jj] == ('nan'):
                gradx[ii,jj] = gradx[ii-1,jj]
        for ii in range(int(mx),int(-1),int(-1)):
            if grady[jj,ii] == ('nan'):
                grady[jj,ii] = grady[jj,ii+1]
            if gradx[ii,jj] == ('nan'):
                gradx[ii,jj] = gradx[ii+1,jj]
    gradx[:,nx-1] = -gradx[:,:(nx-1)].sum(1)
    grady[nx-1,:] = -grady[:(nx-1),:].sum(0)
    return gradx,grady

def hudgins_extend_mask0(self,gradx,grady):
    ''' extension tecchnique Poyneer 2002 '''
    nx = self.nx
    ny = self.ny
    if (nx % 2 == 0): #even
        mx = nx/2
    else: #odd
        mx = (nx+1)/2
    for jj in range(int(nx)):
        for ii in range(int(mx),int(nx)):
            if grady[jj,ii] == (0.0):
                grady[jj,ii] = grady[jj,ii-1]
            if gradx[ii,jj] == (0.0):
                gradx[ii,jj] = gradx[ii-1,jj]
```

```
            for ii in range(int(mx),int(-1),int(-1)):
                if grady[jj,ii] == (0.0):
                    grady[jj,ii] = grady[jj,ii+1]
                if gradx[ii,jj] == (0.0):
                    gradx[ii,jj] = gradx[ii+1,jj]
        gradx[:,nx-1] = -gradx[:,:(nx-1)].sum(1)
        grady[nx-1,:] = -grady[:(nx-1),:].sum(0)
        return gradx,grady

    def hudgins_prep(self):
        nx = self.nx
        ny = self.ny
        k,l = N.meshgrid(N.arange(ny),N.arange(nx))
        self.numx = (N.exp(-2j*pi*k/nx)-1)
        self.numy = (N.exp(-2j*pi*l/nx)-1)
        self.den = 4*(N.sin(pi*k/nx)**2 + N.sin(pi*l/nx)**2)
        return True

#fid = open('InverseMatrix_LSM.dat','w')
#s.tofile(fid, ",", "%f")
#fid.close()
```